A Scheme for Ultra-fast Computed Tomography Based on Stationary Multi-beam X-ray Sources

Hao Gong

Dissertation submitted to the faculty of the Virginia Polytechnic Institute and State University in partial fulfillment of the requirements for the degree of

Doctor of Philosophy

In

Biomedical Engineering

Guohua Cao, Chair

Stephen LaConte

Ge Wang

Chris Wyatt

Yizhen Zhu

01-18-2017

Blacksburg, VA

Keywords: Multi-source, computed tomography, scatter correction, temporal resolution, interior tomography

A Scheme for Ultra-fast Computed Tomography Based on Stationary Multi-beam X-ray Sources

Hao Gong

ABSTRACT

The current cardiac computed tomography (CT) technology is mainly limited by motion blurring and radiation dose. The conceptual multi-source interior CT scheme has provided a potential solution to reduce motion artifacts and radiation exposure. This dissertation work conducted multi-facet investigations on a novel multi-source interior CT architecture (G. Cao, et. al, IEEE Access, 2014;2:1263-71) which employs distributed stationary multi-beam Carbon-nanotube (CNT) X-ray sources and simultaneously operates multiple source-detector chains to improve temporal resolution. The collimation based interior CT is integrated in each imaging chain, to suppress radiation dose. The central thesis statement is: Compared to conventional CT design, this distributed source array based multi-source interior CT architecture shall provide ultra-fast CT scan of region-of-interest (ROI) inside body with comparable image quality at lower radiation dose. Comprehensive studies were conducted to separately investigate three critical aspects of multi-source interior CT: interior CT mode, X-ray scattering, and scatter correction methods. First, a single CNT X-ray source based interior micro-CT was constructed to serve as a down-

scaled experimental verification platform for interior CT mode. Interior CT mode demonstrated comparable contrast-noise-ratio (CNR) and image structural similarity to the standard global CT mode, while inducing a significant radiation dose reduction (< 83.9%). Second, the data acquisition of multi-source interior CT was demonstrated at clinical geometry, via numerical simulation and physical experiments. The simultaneously operated source-detector chains induced significant X-ray forward / cross scattering and thus caused severe CNR reduction (< 68.5%) and CT number error (< 1122 HU). To address the scatter artifacts, a stationary beam-stopper-array (BSA) based and a source-trigger-sequence (STS) based scatter correction methods were proposed to enable the online scatter measurement / correction with further radiation dose reduction (< 50%). Moreover, a deterministic physics model was also developed to iteratively remove the scatter-artifacts in the multi-source interior CT, without the need for modifications in imaging hardware or protocols. The three proposed scatter correction methods improved CNR (< 94.0%) and suppressed CT number error (< 48 HU). With the dedicated scatter correction methods, the multi-source interior CT could provide ROI-oriented imaging with acceptable image quality at significantly reduced radiation dose.

A Scheme for Ultra-fast Computed Tomography Based on Stationary Multi-beam X-ray Sources

Hao Gong

GENERAL AUDIENCE ABSTRACT

Cardiac computed tomography (CT) technology enables a non-invasive imaging examination of patients' cardiovascular system, and thus it has been widely applied in the fields of the diagnosis, treatment, and scientific research of cardiovascular diseases (CVD). The image quality of the current cardiac CT is frequently degraded by rapid cardiac motion and X-ray scattering, and the potential radiation harm has also raised public concern. The above limitations could be theoretically overcome by a recently proposed conceptual stationary multi-beam X-ray sources based interior CT (i.e. multi-source interior CT) system architecture. This dissertation conducted a comprehensive investigation on the actual image quality and radiation dose of this conceptual CT system. The experiments demonstrated that a significant radiation dose reduction could be achieved in multi-source interior CT. The image quality of multi-source interior CT could be maintained with the in-house-developed scatter correction methods.

Acknowledgements

First, I would like to thank Dr. Guohua Cao. As my advisor, he has provided a fantastic mentorship throughout all aspects of my PhD research. Both the academic and professional advices / opportunities that he has provided have been extremely valuable for me to not only accomplish my research work but also broaden my career horizon.

Second, I would like to thank Drs. Ge Wang, Hengyong Yu, Xun Jia and Jia-qiang He for their continued supports in our collaborative research projects. I would also like to thank my committee members: Drs. Stephen LaConte, Chris Wyatt and Yizhen Zhu for their great expertise and deep insights in guiding my research.

Third, I would like to thank my lab-mates and colleagues: Drs. Rui Liu, Chuang Miao and Kriti Sen Sharma for their hard work in the collaboration of software package for image reconstruction. I would also like to thank Mr. Craig McNally (from the center for injury biomechanics, Virginia Tech) for his great help in the fabrication of phantoms and mechanical components.

Finally, I would like to dedicate this dissertation to my wife and my parents. They have been great sources of inspiration and I could not have completed this journey without them.

Table of contents

List of Figures

List of Tables

List of Abbreviations

AAPD	Averaged absolute percentage difference
ASG	Anti-scatter grid
BSA	Beam-stopper-array
CNR	Contrast-noise-ratio
CNT	Carbon-nanotube
CSPR	Cross scatter to primary ratio
CT	Computed tomography
CTDI	Computed tomography dose index
CVD	Cardiovascular disease
DLP	Dose length product
DSCT	Dual-source computed tomography
FDK	Feldkamp-Davis-Kress algorithm
FOV	Field-of-view
FASKS	Fast adaptive scatter kernel superposition
FSDDR	Frequency split displaced detector reconstruction
FSPR	Forward scatter to primary ratio
HU	Hounsfield unit
MAE	Mean absolute error
MSSIM	Mean structural similarity index
MC	Monte Carlo simulation
ROI	Region-of-interest
SMOG	Synchronized moving grid
STS	Source-trigger-sequence

Chapter 1 Introduction

1.1 Current status of Cardiac CT

As one of the leading causes of death, cardiovascular diseases (CVD) account for 17.3 million deaths per year [1]. Cardiac CT imaging has been undergoing a rapid world-wide growth, and the major driving force is the growing demand for the prevention and treatment of CVD [2]. First, Cardiac CT has been frequently employed for qualitative visual interpretation of anatomical structures and / or pathological features. For example, in myocardial assessment, the region of infarcts can be identified through the changes in attenuation (i.e. CT numbers of the image pixels) relative to normal adjacent tissues [3]. Second, in some other clinical applications, CT numbers can become useful for the quantitative diagnosis. For instance, in plaque imaging, the different types of plaques could be distinguished by thresholding CT numbers of the plaque regions in CT images [4]. Thus far, cardiac CT imaging has become one of the most promising complementary techniques in the primary detection of CVD [5].

The major benefit of cardiac CT is its capability of noninvasively obtaining anatomical and functional information of the patients' hearts [6]. Nevertheless, several major limitations are still present in the current cardiac CT techniques. First, the temporal resolution remains a major challenge, because the rapid cardiac motion can induce severe motion blurring in CT images. A cardiac CT system with fast-enough temporal resolution can virtually freeze cardiac motion and reduce the

motion blurring [7]. The current highest temporal resolution (up to 66 ms) is provided by the state-of-the-art dual-source CT (Siemens Healthcare, Inc.) [8, 9]. However, dual-source CT still frequently employs ECG gating strategy to acquire CT images at diastolic phase to minimize motion blurring [10, 11]. Higher temporal resolution (<50ms) is still desired for functional imaging of arbitrary cardiac phases, which is especially true for the patients with irregular heart rate [12, 13]. Second, the cumulative radiation dose from cardiac CT has become a growing public concern [14]. Evidence has been reported recently that the relatively high radiation dose from cardiac CT can cause DNA damage and increase the risk of cancer [15]. Compared with single source CT, dual-source CT has to further increase radiation dose in order to maintain the image contrast-noise-ratio (CNR) [16]. Universal consensus has been achieved on keeping the radiation dose as low as reasonably possible [17, 18]. Therefore, it is significant to reduce radiation dose from cardiac CT, while maintaining or even improving its image quality. In addition, X-ray scatter artifacts still persist in the current cardiac CT. Scatter artifacts have become well-known for degrading image quality, including CT number inaccuracy, image contrast degradation and non-uniformity [19]. In dual-source CT, the temporal resolution is increased at the expense of additional X-ray cross scattering due to the simultaneous data acquisition from the two source-detector chains. The reason is that, in dual-source CT, each X-ray detector receives the scattered X-ray photons originated from the opposite X-ray source (as “forward scattering”), and also from the other source at a cross angle (as “cross scattering”) [16].

1.2 Multi-source CT schemes

During the development of CT scanners, the majority of the research for temporal resolution improvement is focused on the increment of gantry rotation speed and X-ray source power [20]. However, both the gantry rotation speed and source power are currently approaching the corresponding engineering limits [21]. On the other hand, the CT systems with multiple X-ray sources (i.e. multi-source CT) have provided potential solutions to further improve temporal resolution. As suggested by the name, there are more than one source-detector chains operated simultaneously in a typical multi-source CT scanner. This is because that, for speeding up the temporal resolution, the efficiency of doubling the number of source-detector chains inside a given gantry is more than twice as much as that of increasing the gantry rotation speed [22].

The development of multi-source CT dates back to the early stage of CT imaging techniques. The first multi-source CT prototype is the dynamic spatial reconstructor (DSR) which was constructed in Mayo clinics in the 1980s [23]. Later on, Sven Fritzler and Jan Matschulla (from Picker Medical System, Inc.) proposed a conceptual triple source CT in 1990s [24]. Nowadays, the standard clinical dual-source CT (DSCT) (Siemens Healthcare, Inc.) that incorporates two pairs of X-ray sources and detectors in one gantry has been routinely employed in daily medical examination [25-27].

A few research groups have reported other conceptual multi-source CT system architecture with the corresponding image reconstruction algorithms. Several examples are listed as follows. Y. Liu *et. al.* derived a generalized Parker's weighting scheme to enable a Feldkamp-type half-scan image reconstruction for a simulated multi-source cone-beam micro-CT [28]. J. Zhao and Y. Xi described a conceptual multi-source CT which employs multiple interlaced source-detector arrays [29]. At the same time, J. Zhao, L. Yang, *et. al.* proposed two triple-source cone-beam CT architectures utilizing a helical curve and a saddle curve scanning trajectory for projection data collection, and they also proposed the corresponding exact volumetric reconstruction algorithms [30, 31]. In addition, G.M. Besson recently proposed a novel dual-gantry CT architecture which decoupled the revolution of X-ray sources and detectors into two independent yet synchronized systems, to further improve the temporal resolution [32].

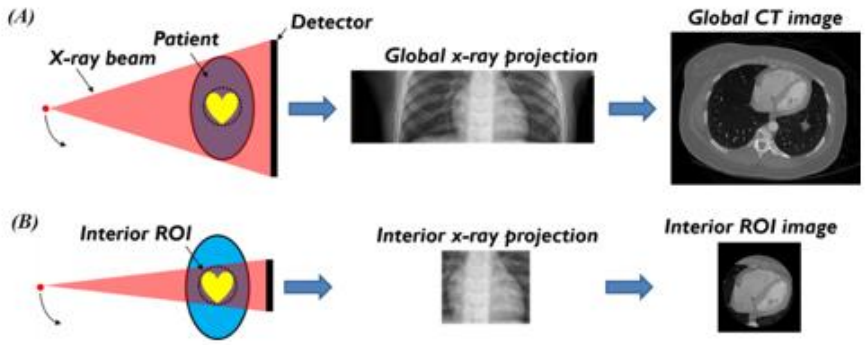

Figure 1-1. The schematics of global CT mode (A) and interior CT mode (B). Global CT mode acquires the complete X-ray projections of the patients. Interior CT mode acquires the truncated X-ray projections through an internal ROI.

The above multi-source CT system architectures employ the standard global CT mode, wherein the fan-beam angle is wide enough to irradiate the entire cross section of the patients. On the other hand, interior CT mode (i.e. interior tomography) can be readily integrated to suppress the radiation exposure in multi-source CT. In interior CT mode, X-ray beam is collimated to confine the field-of-view (FOV) to an relatively small internal region of interest (ROI) inside the patients, and hence reducing the radiation exposure to the surrounding tissues [33, 34]. Figure 1-1 illustrates the schematics of global CT mode and interior CT mode.

Moreover, interior CT mode enables the integration of more source-detector chains in a given gantry space [35]. The multi-source interior CT architectures have the potential to achieve the high temporal resolution that is required for all-phase cardiac CT imaging [36]. Wang *et. al.* presented a general scheme of multi-source interior CT which operated multiple ($\geq$ 7) rotating source-detector chains simultaneously [37]. Lately, Cao *et. al.* proposed a multi-source interior CT architecture that employed three stationary distributed X-ray source arrays and three rotating detectors (see Figure 1 of the reference [36]). This dissertation work conducted a multi-facet investigation on this multi-source interior CT architecture.

The stationary distributed X-ray source arrays based multi-source interior CT architecture is briefly summarized as follows. Each source array can be based on the CNT field-emission or the conventional dispenser cathodes. Therefore, the source array is programmable for electronic control of X-ray emission, which

enables flexible exposure control for cardiac imaging [38]. The three stationary X-ray source arrays are placed symmetrically outside the gantry, and virtually rotate three X-ray sources by electronically sweeping three X-ray beams around the patients. The three X-ray beams are activated simultaneously (separated by 120° angular interval) in CT scan. This architecture could further improve temporal resolution, because of the following two major reasons. First, the sweeping of X-ray beams could be conducted at a much faster speed than that of mechanical rotation of conventional X-ray source. Second, three source-detector chains are operated simultaneously to further reduce the total acquisition time for a complete CT dataset. A comparison of the theoretical temporal resolution between the multi-source interior CT and the standard CT design is shown in Table 2 of the reference [36]. Moreover, this architecture integrates the collimation based interior CT to all source-detector chains, and thus the X-ray beam coverage is reduced to reduce the radiation exposure to the peripheral tissues.

The actual image quality and radiation dose of multi-source interior CT has not been experimentally evaluated. The construction of a prototype multi-source interior CT can be an expensive and time-consuming process. Therefore, it is necessary to conduct a proof-of-concept study to evaluate the feasibility of this system architecture.

1.3 X-ray scatter correction methods

In a multi-source CT architecture, X-ray scattering problem is more complicated than that in a conventional single-source CT. X-ray scattering in a multi-source CT architecture involves both the traditional forward scattering that occurs at the same source-detector chain, and the cross scattering that takes place among different source-detector chains. Each X-ray detector receives the forward scattering originated from the X-ray source at the opposite side, and more importantly, the "cross" scattering originated from the other activated X-ray sources at cross angles (hence termed "cross scattering") [16]. The superposition of forward scattering signals and cross scattering signals at the detector will lead to more noise and lower contrast-to-noise ratio (CNR) in the final CT images. Therefore, cross scattering tends to increase the total amount of scattering signals that can be received by the detectors in multi-source CT architectures, and dedicated cross-scatter correction techniques are needed to improve CT image quality.

A lot of research efforts have been focused on the correction of forward scattering in the standard single-source CT. The existing forward-scatter correction methods could be categorized as measurement-based and model-based methods. As for the measurement-based estimation, a variety of beam-stopper-array (BSA) based approaches have been developed, wherein forward scattering signals are sampled in the shadow of the blades of BSA. For instance, Ning *et. al*. used a matrix-type beam-stopper-array (BSA) to sample the forward scattering signals from a set of scout

views and then applied spatial / angular interpolation across the detector plane and angular positions to acquire a complete estimation of scattering signals [39]. A synchronized-moving-grid (SMOG) system was proposed by Ren et. al, wherein a stripe-type BSA was shifted periodically at each view to obtain two complementary projections and form a complete measurement of forward scattering signals at each view [40]. On the other hand, the model-based scatter correction methods could be further categorized as projection-based (2D model) and image-based (3D model) methods. In the projection-based methods, scattering signals are directly de-convolved from the measured X-ray projections. In the image-based methods, scattering signals are typically derived using a complete volume of reconstructed CT images. For example, the scatter kernels can be adapted to the local object thickness and then superposed to deconvolve the forward scattering signals from the X-ray projections [41]. Or, a convolution kernel can be first applied to estimate the distribution of forward scattering signals, and then an object-size-dependent scaling factor shall be applied to adjust the magnitudes of forward scattering signals [42]. Furthermore, Monte Carlo simulation can be utilized to simulate the history of each X-ray photon emitted from the X-ray source, which could be highly accurate after deliberated calibration. Despite the low computational efficiency, a few acceleration techniques are now available for Monte Carlo simulation (e.g. “fixed forced detection” technique in reference [43]).

On the contrary, there are limited number of cross-scatter correction methods for dual-source CT in the previous literature. Notice that the conventional hardware-based scatter suppression techniques (i.e. anti-scatter grid, air gap & bow-tie filter) have been demonstrated to be insufficient for the suppression of cross scattering signals in the standard dual-source CT [16, 44]. Previously, Siemens Healthcare developed two dedicated scatter correction approaches for its dual-source CT [45]: In the first method, total X-ray scattering signals (i.e. forward / cross scattering signals) were sampled by using additional scatter detectors that were placed outside the X-ray beams in the z-direction; In the second method, a huge database of X-ray scattering signals was established by using the data from previous phantom experiments and Monte Carlo simulation. Lately, Ren *et. al.* presented a BSA based method for dual-source CT, wherein two BSAs were mounted in front of the X-ray sources and the complete measurement of total scattering signals were obtained by shifting the BSAs at all views [46]. Thus far, the hardware-based scatter correction methods typically caused certain modifications of the imaging system configuration (e.g. BSA or scatter sensors), while the model-based methods frequently induced heavy workload in the numerical computation (e.g. Monte Carlo simulation) and / or the parametric calibration (e.g. scatter kernel convolution).

In addition, interior CT mode may suppress the magnitudes of X-ray scattering signals, because of the reduced FOV. The data acquisition of multi-source interior CT architectures have been simulated using conventional single-source CT data [36,

37], yet the effects of cross scattering signals were not considered in these previous studies. Therefore, this dissertation work demonstrated the distribution and magnitudes of the X-ray forward / cross scattering in multi-source interior CT architecture, and then developed three effective scatter correction techniques for multi-source interior CT.

1.4 Dissertation organization

The organization of the remaining chapters of this dissertation is as follows:

Chapter 2 introduces the experimental evaluation of single CNT source based interior micro-CT. This chapter presents the experimental methods of system implementation, geometric calibration and radiation dose measurement. It also presents the corresponding image reconstruction algorithm as well as the evaluation methods used for image quality analysis.

Chapter 3 demonstrates the effects of X-ray scattering signals (i.e. forward scattering and cross scattering) in multi-source interior CT system architecture at clinical imaging geometry, via Monte Carlo simulation and physical experiments. Moreover, it also presents two measurement-based scatter correction methods dedicated for multi-source interior CT architecture: a stationary BSA based method and a source-trigger-sequence (STS) based method. A comprehensive evaluation of image quality before and after scatter correction is included in this chapter.

Chapter 4 mainly introduces a physics model based scatter correction method dedicated for multi-source interior CT architecture. This chapter presents the physics model of multi-source interior CT and an iterative framework of scatter correction. A comprehensive evaluation of image quality before and after scatter correction is also demonstrated in this chapter.

1.5 Attribution

In this section, the contributions of each author in the following chapters of this dissertation are briefly reported below, since these works are not sole-authorships.

Chapter 2 is the extended version of the paper entitled "Interior Tomographic Imaging of Mouse Heart in a Carbon Nanotube Micro-CT" (published in Journal of X-ray Science and Technology, i.e. the reference [47]). As the first author, my contribution includes the following aspects: the construction of CNT source based interior micro-CT, experimental design, phantom fabrication, phantom / animal specimen micro-CT scans, pre-processing of X-ray projections, image reconstruction, image quality analysis, radiation dose measurement. R. Liu and H. Yu contributed to the development of GPU based acceleration techniques for image reconstruction. L. Kan and JQ. He contributed to the preparation of the animal specimen. G. Cao supervised this study.

Chapter 3 is the extended version of the paper entitled "X-ray scatter correction for multi-source interior computed tomography" (published in Medical Physics, i.e. the

reference [48]). As the first author, I contributed to the following aspects of this study: the construction of experimental imaging platform, experiment design, phantom fabrication, phantom scans, image reconstruction, experimental data analysis, and more importantly, the development of two dedicated measurement-based scatter correction methods. H. Yan, X. Jia, and B. Li contributed to the Monte Carlo simulation of multi-source interior CT system architecture. G. Wang and G. Cao supervised this study.

Chapter 4 is the extended version of the paper entitled "Physics model based scatter correction in multi-source interior computed tomography". As the first author, my contribution includes the following aspects: the development and implementation of the deterministic physics model, the implementation of iterative scatter correction, the experimental design, data collection, and experimental results analysis. X. Jia and B. Li contributed the Monte Carlo simulation of multi-source interior CT. G. Cao supervised this study.

1.6 Relevant publications

The following list shows the manuscripts published, accepted, or prepared concurrently with this dissertation.

Journal papers:

1) G. Cao, B. Liu, **H. Gong**, H. Yu, G Wang, "A stationary-sources and rotating-detectors computed tomography architecture for higher temporal resolution and lower radiation dose", IEEE Access, 2014.
2) **H. Gong**, M. Chuang, H. Yu, G. Cao, "Realistic cone-beam micro-CT datasets for reproducible evaluation of reconstruction algorithms", JSM BioMed Img Data Paper, 2014.
3) K. Sen Sharma, **H. Gong**, O. Ghasemalizadeh, H. Yu, G. Wang, G. Cao, "Interior micro-CT with an offset detector", Med Phys, Jun;41(6), 2014.
4) S. Zhang, D. Zhang, **H. Gong**, O. Ghasemalizadeh, G. Wang, G. Cao, "Fast and accurate computation of system matrix for area integral model-based algebraic reconstruction technique", Optical Engineering, 2014.
5) **H. Gong**, R. Liu, H. Yu, J. Lu, O. Zhou, L. Kan, JQ. He, G. Cao, et al, "Interior Tomographic Imaging of Mouse Heart in a Carbon Nanotube Micro-CT", Journal of X-ray Science and Technology, May 2;24(4):549-63, 2016.
6) **H. Gong**, H. Yan, X. Jia, B. Li, G. Wang, G. Cao, "X-ray scatter correction for multi-source interior computed tomography", Med Phys, 2016, in press.
7) **H. Gong**, X. Jia, B. Li, G. Cao, "Physics model based scatter correction in multi-source interior computed tomography", in preparation.

Conference papers:

1) **H. Gong**, C. Miao, H. Yu, G. Wang, G. Cao, "Real phantom datasets for the evaluation of reconstruction algorithms at various dose conditions", IEEE 11th International Symposium on Biomedical Imaging (ISBI), 65-68, 2014.
2) **H. Gong**, J. Lu, O. Zhou, G. Cao, "Implementation of interior micro-CT on a carbon nanotube dynamic micro-CT scanner for lower radiation dose", Proc. SPIE Medical Imaging, 2015

3) X. Yu, H. Wang, W. Feng, **H. Gong**, G. Cao, "cuART: Fine-Grained Algebraic Reconstruction Technique for Computed Tomography Images on GPUs", Proc. IEEE/ACM CCGrid 2016.

Conference abstracts:

1) **H. Gong**, B. Liu, et al, "Cardiac CT architecture with lower radiation dose and higher temporal resolution", BMEs annual conference, Seattle, WA, 2013 (Poster presentation).
2) **H. Gong**, G. Cao, "Interior micro-CT for radiation dose reduction", BMEs annual conference, San Antonio, 2014 (Poster presentation).
3) **H. Gong**, O. Pen, G. Cao, "Scatter reduction and correction in multi-source cardiac computed tomography", BMEs annual conference, Tampa, FL, 2015 (Oral presentation).

References

[1] D. Mozaffarian, E. J. Benjamin, A. S. Go, D. K. Arnett, M. J. Blaha, M. Cushman, *et al.*, "Heart Disease and Stroke Statistics—2016 Update: A Report From the American Heart Association," *Circulation*, December 16, 2015 2015.

[2] R. C. Cury, "President's page: Worldwide expansion of cardiac CT—an impressive growth in recent years," *Journal of Cardiovascular Computed Tomography*, vol. 9, pp. 77-79.

[3] H. K. Pannu, P. T. Johnson, and E. K. Fishman, "64 Slice multi-detector row cardiac CT," *Emergency Radiology*, vol. 16, pp. 1-10, 2009.

[4] S. Schroeder, A. Kopp, A. Baumbach, A. Kuettner, C. Georg, B. Ohnesorge, *et al.*, "Non-invasive characterisation of coronary lesion morphology by multi-slice computed tomography: a promising new technology for risk stratification of patients with coronary artery disease," *Heart*, vol. 85, pp. 576-578, 2001.

[5] K. Nikolaou, H. Alkadhi, F. Bamberg, S. Leschka, and B. J. Wintersperger, "MRI and CT in the diagnosis of coronary artery disease: indications and applications," *Insights into Imaging*, vol. 2, pp. 9-24, 2011.

[6] D. B. Mark, D. S. Berman, M. J. Budoff, J. J. Carr, T. C. Gerber, H. S. Hecht, *et al.*, "ACCF/ACR/AHA/NASCI/SAIP/SCAI/SCCT 2010 Expert Consensus Document on Coronary Computed Tomographic AngiographyA Report of the American College of Cardiology Foundation Task Force on Expert Consensus Documents," *Journal of the American College of Cardiology,* vol. 55, pp. 2663-2699, 2010.

[7] B. M. Ohnesorge, T. G. Flohr, C. R. Becker, and M. F. Reiser, *Multi-slice CT in Cardiac Imaging: Technical Principles, Imaging Protocols, Clinical Indications and Future Perspective*: Springer Berlin Heidelberg, 2013.

[8] M. Lell, M. Marwan, T. Schepis, T. Pflederer, K. Anders, T. Flohr, *et al.*, "Prospectively ECG-triggered high-pitch spiral acquisition for coronary CT angiography using dual source CT: technique and initial experience," *European Radiology,* vol. 19, pp. 2576-2583, 2009.

[9] T. G. Flohr, S. Leng, L. Yu, T. Allmendinger, H. Bruder, M. Petersilka, *et al.*, "Dual-source spiral CT with pitch up to 3.2 and 75 ms temporal resolution: Image reconstruction and assessment of image quality," *Medical Physics,* vol. 36, pp. 5641-5653, 2009.

[10] S. Achenbach, D. Ropers, A. Kuettner, T. Flohr, B. Ohnesorge, H. Bruder, *et al.*, "Contrast-enhanced coronary artery visualization by dual-source computed tomography - Initial experience," *European Journal Of Radiology,* vol. 57, pp. 331-335, Mar 2006.

[11] M. Kachelrieß, M. Knaup, and W. A. Kalender, "Multithreaded cardiac CT," *Medical Physics,* vol. 33, pp. 2435-2447, 2006.

[12] S. Leschka, S. Wildermuth, T. Boehm, L. Desbiolles, L. Husmann, A. Plass, *et al.*, "Noninvasive Coronary Angiography with 64-Section CT: Effect of Average Heart Rate and Heart Rate Variability on Image Quality," *Radiology,* vol. 241, pp. 378-385, 2006.

[13] M. Mahesh and D. D. Cody, "Physics of Cardiac Imaging with Multiple-Row Detector CT," *RadioGraphics,* vol. 27, pp. 1495-1509, 2007.

[14] P. S. Douglas, J. J. Carr, M. D. Cerqueira, J. E. Cummings, T. C. Gerber, D. Mukherjee, *et al.*, "Developing an Action Plan for Patient Radiation Safety in Adult Cardiovascular MedicineProceedings From the Duke University Clinical Research Institute/American College of Cardiology Foundation/American Heart Association Think Tank Held on February 28, 2011," *Journal of the American College of Cardiology,* vol. 59, pp. 1833-1847, 2012.

[15] P. K. Nguyen, W. H. Lee, Y. F. Li, W. X. Hong, S. Hu, C. Chan, *et al.*, "Assessment of the Radiation Effects of Cardiac CT Angiography Using Protein and Genetic Biomarkers," *JACC Cardiovasc Imaging,* vol. 8, pp. 873-84, Aug 2015.

[16] K. J. Engel, C. Herrmann, and G. Zeitler, "X-ray scattering in single- and dual-source CT," *Medical Physics,* vol. 35, pp. 318-332, 2008.

[17] L. Yu, X. Liu, S. Leng, J. M. Kofler, J. C. Ramirez-Giraldo, M. Qu, *et al.*, "Radiation dose reduction in computed tomography: techniques and future perspective," *Imaging in medicine*, vol. 1, pp. 65-84, 2009.
[18] K. J. Strauss and S. C. Kaste, "The ALARA (as low as reasonably achievable) concept in pediatric interventional and fluoroscopic imaging: striving to keep radiation doses as low as possible during fluoroscopy of pediatric patients—a white paper executive summary," *Pediatric Radiology,* vol. 36, pp. 110-112, 2006.
[19] J. H. Siewerdsen and D. A. Jaffray, "Cone-beam computed tomography with a flat-panel imager: Magnitude and effects of x-ray scatter," *Medical Physics,* vol. 28, pp. 220-231, 2001.
[20] W. A. Kalender, "X-ray computed tomography," *Phys Med Biol,* vol. 51, pp. R29-43, Jul 7 2006.
[21] P. Schardt, J. Deuringer, J. r. Freudenberger, E. Hell, W. Knüpfer, D. Mattern, *et al.*, "New x-ray tube performance in computed tomography by introducing the rotating envelope tube technology," *Medical Physics,* vol. 31, p. 2699, 2004.
[22] W. A. Kalender, "CT: the unexpected evolution of an imaging modality," *European Radiology,* vol. 15, pp. D21-D24, Nov 2005.
[23] E. L. Ritman, J. H. Kinsey, R. A. Robb, B. K. Gilbert, L. D. Harris, and E. H. Wood, "3-DIMENSIONAL IMAGING OF HEART, LUNGS, AND CIRCULATION," *Science,* vol. 210, pp. 273-280, 1980.
[24] E. Dafni and D. Ruimi, "Multiple source CT scanner," ed: Google Patents, 1999.
[25] T. G. Flohr, C. H. McCollough, H. Bruder, M. Petersilka, K. Gruber, C. Suss, *et al.*, "First performance evaluation of a dual-source CT (DSCT) system," *European Radiology,* vol. 16, pp. 256-268, Feb 2006.
[26] B. Krauss, B. Schmidt, and T. G. Flohr, "Dual source CT," in *Dual energy CT in clinical practice*, ed: Springer, 2011, pp. 11-20.
[27] S. Fritzler and J. Matschulla, "Multi-source CT system," ed: Google Patents, 2015.
[28] Y. Liu, H. Liu, Y. Wang, and G. Wang, "Half-scan cone-beam CT fluoroscopy with multiple x-ray sources," *Medical physics,* vol. 28, pp. 1466-1471, 2001.
[29] J. Zhao and Y. Xi, "A Reconstruction Method for Circular Interlaced-Source-Detector-Array CT," in *2009 First International Conference on Information Science and Engineering*, 2009, pp. 3575-3578.
[30] J. Zhao, Y. Jin, Y. Lu, and G. Wang, "A Filtered Backprojection Algorithm for Triple-Source Helical Cone-Beam CT," *IEEE transactions on medical imaging,* vol. 28, pp. 384-393, 2009.
[31] Y. Lu, J. Zhao, and G. Wang, "Exact image reconstruction with triple-source saddle-curve cone-beam scanning," *Physics in medicine and biology,* vol. 54, pp. 2971-2991, 2009.

[32] G. M. Besson, "New CT system architectures for high temporal resolution with applications to improved geometric dose efficiency and cardiac imaging," *Medical Physics,* vol. 42, pp. 2668-2678, 2015.
[33] D. Bharkhada, H. Yu, R. Dixon, Y. Wei, J. J. Carr, J. D. Bourland, *et al.*, "Demonstration of Dose and Scatter Reductions for Interior Computed Tomography," *Journal of computer assisted tomography,* vol. 33, p. 967, 2009.
[34] H. Gong, R. Liu, H. Yu, J. Lu, O. Zhou, L. Kan, *et al.*, "Interior tomographic imaging of mouse heart in a carbon nanotube micro-CT," *Journal of X-Ray Science and Technology,* vol. 25, 2016.
[35] G. Wang and H. Y. Yu, "The meaning of interior tomography," *Physics in Medicine and Biology,* vol. 58, pp. R161-R186, Aug 21 2013.
[36] G. Cao, B. Liu, H. Gong, H. Yu, and G. Wang, "A stationary-sources and rotating-detectors computed tomography architecture for higher temporal resolution and lower radiation dose," *Access, IEEE,* vol. 2, pp. 1263-1271, 2014.
[37] G. Wang, H. Yu, and Y. Ye, "A scheme for multisource interior tomography," *Medical Physics,* vol. 36, pp. 3575-3581, 2009.
[38] G. Cao, L. M. Burk, Y. Z. Lee, X. Calderon-Colon, S. Sultana, J. Lu, *et al.*, "Prospective-gated cardiac micro-CT imaging of free-breathing mice using carbon nanotube field emission x-ray," *Med Phys,* vol. 37, pp. 5306-12, Oct 2010.
[39] R. Ning, X. Tang, and D. Conover, "X-ray scatter correction algorithm for cone beam CT imaging," *Medical Physics,* vol. 31, pp. 1195-1202, 2004.
[40] L. Ren, F.-F. Yin, I. J. Chetty, D. A. Jaffray, and J.-Y. Jin, "Feasibility study of a synchronized-moving-grid (SMOG) system to improve image quality in cone-beam computed tomography (CBCT)," *Medical Physics,* vol. 39, pp. 5099-5110, 2012.
[41] M. Sun and J. M. Star-Lack, "Improved scatter correction using adaptive scatter kernel superposition," *Physics in Medicine and Biology,* vol. 55, p. 6695, 2010.
[42] M. Michael, A. K. Willi, and K. Yiannis, "A fast and pragmatic approach for scatter correction in flat-detector CT using elliptic modeling and iterative optimization," *Physics in Medicine and Biology,* vol. 55, p. 99, 2010.
[43] G. Poludniowski, P. M. Evans, V. N. Hansen, and S. Webb, "An efficient Monte Carlo-based algorithm for scatter correction in keV cone-beam CT," *Physics in Medicine and Biology,* vol. 54, p. 3847, 2009.
[44] K. Yiannis and A. K. Willi, "Intensity distribution and impact of scatter for dual-source CT," *Physics in Medicine and Biology,* vol. 52, p. 6969, 2007.
[45] M. Petersilka, K. Stierstorfer, H. Bruder, and T. Flohr, "Strategies for scatter correction in dual source CT," *Medical Physics,* vol. 37, pp. 5971-5992, 2010.

[46] L. Ren, Y. Chen, Y. Zhang, W. Giles, J. Jin, and F. F. Yin, "Scatter Reduction and Correction for Dual-Source Cone-Beam CT Using Prepatient Grids," *Technol Cancer Res Treat,* May 24 2015.
[47] H. Gong, R. Liu, H. Yu, J. Lu, O. Zhou, L. Kan, *et al.*, "Interior tomographic imaging of mouse heart in a carbon nanotube micro-CT," *J Xray Sci Technol,* vol. 24, pp. 549-63, May 2 2016.
[48] H. Gong, H. Yan, X. Jia, B. Li, G. Wang, and G. Cao, "X-ray scatter correction for multi-source interior computed tomography," *Medical Physics,* vol. 44, pp. 71-83, 2017.

Chapter 2 Interior tomographic imaging in a Carbon nanotube X-ray source based micro-CT

Hao Gong[1], Rui Liu[2, 3], Hengyong Yu[3], Jianping Lu[4], Otto Zhou[4], Lijuan Kan[5], Jiaqiang He[5], and Guohua Cao[1]

[1]Department of Biomedical Engineering and Mechanics, Virginia Polytechnic Institute and State University, Blacksburg, VA 24061, USA

[2]Virginia Tech-Wake Forest School of Biomedical Engineering and Science, Wake Forest University Health Sciences, Winston-Salem, NC 27157, USA

[3]Department of Electrical and Computer Engineering, University of Massachusetts Lowell, Lowell, MA 01854, USA

[4]Department of Physics and Astronomy, University of North Carolina at Chapel Hill, Chapel Hill, NC 27599, USA

[5]Department of Biomedical Sciences and Pathobiology, Virginia-Maryland College of Veterinary Medicine, Virginia Polytechnic Institute and State University, VA 24061, USA

Publication information – The major contents of this chapter were published as: Hao Gong, Rui Liu, Hengyong Yu, Jianping Lu, Otto Zhou, Lijuan Kan, Jiaqiang He, Guohua

Cao, “Interior tomographic imaging of mouse heart in a carbon nanotube micro-CT”, ***Journal of X-ray Science and Technology***, vol. 24, no. 4, pp. 549-563, 2016. doi: 10.3233/XST-160574. https://www.ncbi.nlm.nih.gov/pubmed/27163376.

2.1 Abstract

The relatively high radiation dose from micro-CT is a cause for concern in preclinical research involving animal subjects. Interior region-of-interest (ROI) imaging was proposed for dose reduction, but has not been experimentally applied in micro-CT. Our aim is to implement interior ROI imaging in a carbon nanotube (CNT) X-ray source based micro-CT, and present the ROI image quality and radiation dose reduction for interior cardiac micro-CT imaging of a mouse heart *in situ*. An aperture collimator was mounted at the source-side to induce a small-sized cone beam (10mm width) at the isocenter. Interior *in situ* micro-CT scans were conducted on a mouse carcass and several micro-CT phantoms. A GPU-accelerated hybrid iterative reconstruction algorithm was employed for volumetric image reconstruction. Radiation dose was measured for the same system operated at the interior and global micro-CT modes. Visual inspection demonstrated comparable image quality between two scan modes. Quantitative evaluation demonstrated high structural similarity index (up to 0.9614) with improved contrast-noise-ratio (CNR) on interior micro-CT mode. Interior micro-CT mode yielded significant reduction (up to 83.9%) for dose length product (DLP). This work demonstrates the applicability of using CNT X-ray

source based interior micro-CT for preclinical imaging with significantly reduced radiation dose.

Keywords: Micro-CT, Interior tomography, Carbon-nanotube X-ray micro-CT

2.2 Introduction

Mouse models of human diseases have been widely used in preclinical studies [1-4]. Micro-CT provides biomedical researchers with low-cost, high-throughput, high-resolution and non-invasive evaluation of anatomical structure and physiological function [5]. However, high radiation dose is often required to generate high-resolution micro-CT images [6]. The radiation dose is estimated to be inversely scaled with the fourth power of image voxel size in order to maintain the same image noise level [6, 7]. Both high-dose radiation exposure [8, 9] and longitudinal low-dose radiation exposure [10, 11] could induce a variety of pathological effects to small animals and perturb the experimental outcomes. The radiation-induced biological effects may increase the difficulty of planning preclinical studies using longitudinal micro-CT scans [12-14]. Therefore, it is important to reduce radiation dose while striving to provide the highest image quality for small animal micro-CT.

Several techniques have been proposed to reduce the radiation dose, such as X-ray flux reduction [15, 16], sparse-view acquisition [17-19], and interior ROI imaging techniques (including theoretically-exact interior tomography [20-23] and other approximate-

reconstruction-based ROI CT techniques [24-28]). X-ray flux reduction and sparse-view acquisition are readily applicable to the existing commercial / laboratory micro-CT scanners [29]. Noise and artifacts caused by X-ray flux reduction and sparse-view acquisition can be reduced by advanced reconstruction algorithms such as the ones based on compressive sensing and/or statistical modeling [15-19]. On the other hand, interior ROI imaging techniques require physical modification of system and/or the scan protocols [23-28]. Briefly, an internal ROI receives primary exposure delivered through an aperture in a "pre-patient" X-ray collimator [23-25, 28], while the region outside the targeted ROI receives no primary exposure. Interior ROI imaging techniques have been shown to significantly reduce radiation dose in clinical CT systems. For instance, R. Chityala *et al* demonstrated 85.7% total dose reduction in a C-arm system, by shielding 82% of original field-of-view (FOV) [27]. D. Bharkhada et al demonstrated up to 58% radiation dose reduction in a clinical spiral CT [23]. L. Chen et al even reported 77.3% dose reduction inside the ROI due to scatter reduction [26]. Moreover, interior ROI imaging techniques can be combined with X-ray flux reduction and sparse-view acquisition to further reduce the radiation dose delivered to the internal ROI [20, 22, 30]. A number of advanced reconstruction algorithms have been proposed to address the artifacts caused by data truncation in interior ROI imaging [20, 31-35]. The aforementioned research works suggest that interior ROI imaging may be applicable in micro-CT for radiation dose reduction.

Nevertheless, to the best of our knowledge, no collimator-based interior ROI imaging techniques have been physically implemented in micro-CT systems, and radiation dose

reduction from interior micro-CT for preclinical imaging has not been experimentally demonstrated. Some commercial micro-CT scanners (e.g. Xradia scanners) can achieve interior tomography through limited detector FOV by multiple objective lens between the sample and the detector. However, the sample is still fully irradiated by a wide X-ray beam and hence it does not serve the purpose of radiation dose reduction. Previously, we have developed a dynamic micro-CT scanner that provides high temporal-spatial resolutions (15msec and 6.2lp/mm) by using a carbon nanotube (CNT) field-emission based X-ray source [36]. The CNT X-ray source is programmable for electronic control of X-ray emission, which enables flexible exposure control for cardiac and respiratory gated micro-CT imaging of free-breathing mice with no wasted radiation exposure [36]. The conventional global micro-CT mode was still used in that scanner. Interior ROI imaging can be applied to restrict the X-ray beam path through a small internal ROI (e.g. heart, lung tumor, etc.) in small animals while significantly reducing radiation exposure to the surrounding tissues. We anticipate that the integration of these two techniques (i.e. CNT dynamic micro-CT and interior ROI imaging) will lead to highest image quality and lowest radiation risk in small animal micro-CT imaging.

In this paper, we describe our work on the implementation of interior ROI imaging in a CNT X-ray source based dynamic micro-CT scanner, and demonstrate the high quality of interior ROI images with greatly reduced radiation dose. We explored several practical issues of CNT X-ray source based interior micro-CT, such as the geometric calibration with a small (10mm) interior FOV, the high-precision alignment between interior FOV of

the scanner and internal ROI of the object, and most importantly, the image quality and radiation dose reduction. This paper is organized as follows. In section 2, we present the system overview, imaging experiments, and methods for image reconstruction and evaluation. In section 3, we show the experimental results. In the last section, we discuss the results and conclude this study.

2.3 Methods

2.3.1 The CNT source based micro-CT system

The schematic system configuration and the physical system setup are shown in Figure 2-1. Interior micro-CT was realized by placing a source collimator (i.e. pre-patient) between X-ray source and objects to reduce the FOV (i.e. from FOV2 to FOV1). The system mainly consists of a flat panel X-ray detector (Hamamatsu, Inc. Japan), a motorized gantry (Huber, Inc. Germany), an XYZ manual sample stage (Newport, Inc. USA), and an in-house-built CNT X-ray source. The detector element size is 50μm. The collimator is a 2mm thick lead plate (with a circular 3.73mm aperture) fixed on an XYR stage (Thorlab, Inc. USA). The CNT X-ray source was constructed by using the previous design [36]. The X-ray focal spot size is of 100μm diameter. The cone angle of X-ray beam was reduced from 30˚ to 3˚, by using the aperture collimator.

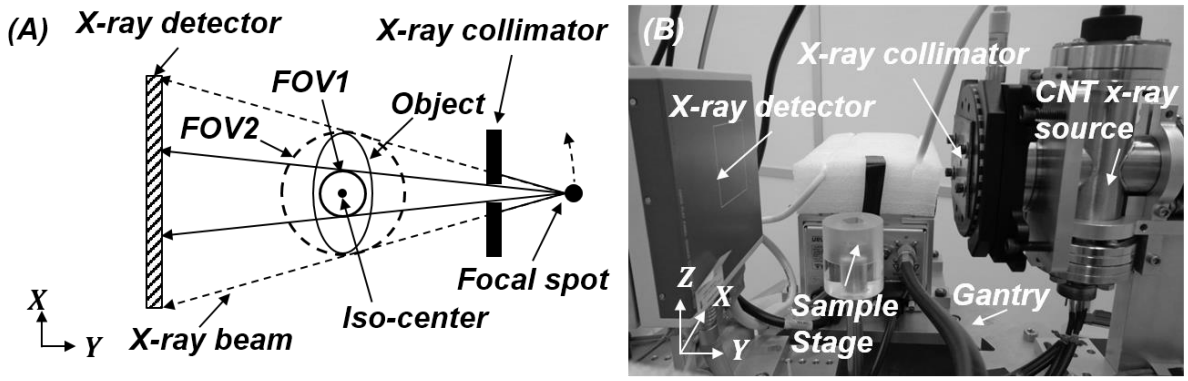

Figure 2-1 (A) Schematic system configuration. FOV1 and FOV2 indicate the FOVs of interior micro-CT and global micro-CT, respectively. (B) Picture of the CNT interior micro-CT system.

During micro-CT scans, the object was stationary while the X-ray source and detector were rotated. The cone-beam circular trajectory was adopted for projection data acquisition. The step-and-shoot scan mode was employed to eliminate the motion blurring caused by continuous mechanical rotation of X-ray source and detector. The X-ray source was operated at 50kV and filtered by a 0.5mm aluminum filter. The diameters of the spherical FOV were 32mm and 10mm in global and interior micro-CT modes, respectively. The interior FOV is just slightly bigger than an adult mouse heart. The other major parameters of scan protocols and imaging geometry are summarized in Table 2-1. The system control software was developed under *LabVIEW* (National Instrument, Inc. USA).

Table 2-1 Parameters of imaging geometry and scanning protocols

Source-isocenter distance	167.8mm
Source-detector distance	261.7mm
Source-collimator distance	62.6mm
X-ray tube voltage	50kV
Exposure per projection	0.1mAs
Scan angle	360°
Number of projections	720

2.3.2 Imaging experiments

The imaging experiments on two micro-CT phantoms and a mouse carcass were conducted to evaluate the image reconstruction quality (see Sec 2.5.1 for evaluation methods). The two micro-CT phantoms included a water phantom and a "multi-feature" phantom. The water phantom was an acrylic cylinder (25.5mm diameter and 1.5mm wall thickness) filled with water, with a sealed polypropylene tube (2.5mm diameter and 0.15mm wall thickness) placed in the center (Figure 2-2A). Micro-CT images of the water phantom were used for Hounsfield Units (HU) calibration and CNR evaluation. The "multi-feature" phantom (diameter 20mm) was fabricated by modifying the one used in our previous works [34, 35]. This phantom comprises of various attenuating materials such as acrylic tube, rubber granules, micro-pillar arrays, micro-capillary tubes, multi-bore tubing, electrical tapes and duct tapes (thickness range from 0.25mm to 5mm, see Figure 2-2B). The "multi-feature" phantom was mainly used to evaluate interior ROI reconstruction with the presence of heterogeneous materials and fine structures. For the animal experiment, a euthanized adult

C57 mouse (body length 110mm and thorax diameter 25mm) underwent an open-chest surgery to ligate all blood vessels from heart, and then 300μl iodine contrast agent (Omnipaque 350mgI/ml) was injected into the heart chambers. The mouse carcass was frozen by using dry ice. The C57 mouse was chosen because it is a typical animal model of human cardiovascular diseases. The ligation was used to retain the contrast agent in mouse heart. Micro-CT scans of the mouse heart *in situ* were conducted using the CNT interior micro-CT scanner. The interior ROI (9mm in diameter) was targeted at the mouse heart. Two low-dose "scout view" projections (separated by 90° angular interval) of the mouse carcass were acquired at global micro-CT mode, to align the mouse heart with system isocenter. Another low-dose raw projection was acquired at interior micro-CT mode, to calibrate the aperture collimator and align the interior FOV with mouse heart. Both global and interior micro-CT scans were conducted for each sample. The scanning protocol is listed in Table 2-1.

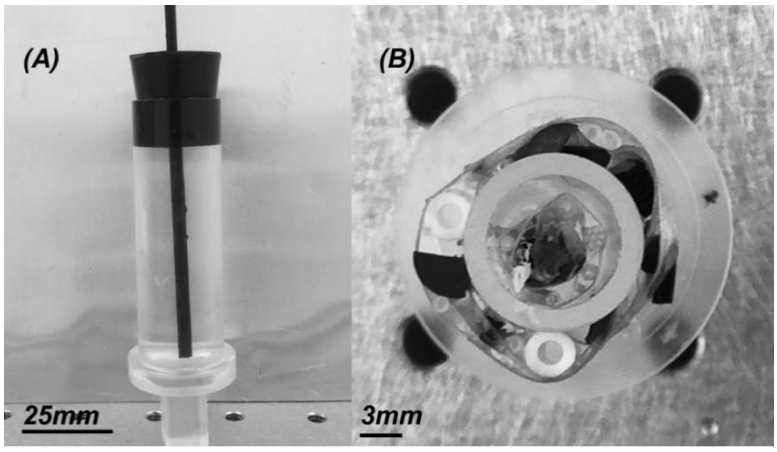

Figure 2-2. In-house-built micro-CT phantoms for imaging experiments. (A) Side view of water phantom. (B) Top view of "Multi-feature" phantom.

2.3.3 Image reconstruction

2.3.3.1 Geometric calibration and data preprocessing

System geometric calibration was conducted to identify the geometric parameters for accurate image reconstruction. Moreover, switching from global mode to interior mode could induce slight misalignment of interior FOV with the system isocenter, because of the mechanical tolerance of the aperture collimator. The analytic method proposed by F. Noo et al [37] was adapted for geometric calibration of interior micro-CT. It is practical to assume that the collimator plane is parallel to system rotation axis and the detector plane. So, the geometric calibration of collimator can be accomplished by quantifying the in-plane offset (termed as "interior detector offset"). Interior detector offset can be calculated using interior projections (i.e. raw projections acquired at interior micro-CT mode). Figure 2-3 demonstrates the geometric calibration of interior detector offset. The projection of the collimator was not exactly circular because of unsmooth edge (Figure 2-3A). Therefore, a circular image mask (as marked by the dashed circle) was applied to the interior projections, and the pixel values outside the mask were set to zeroes (Figure 2-3B). P_m is the center of image mask, and P_1 is the intercept point between the detector plane and the "piercing line" (i.e. the line connecting focal spot and isocenter). The offset (d_x, d_y) between P_1 and P_m is defined as the interior detector offset. Raw projections were preprocessed to remove detector defects and then subjected to blank and dark projection corrections.

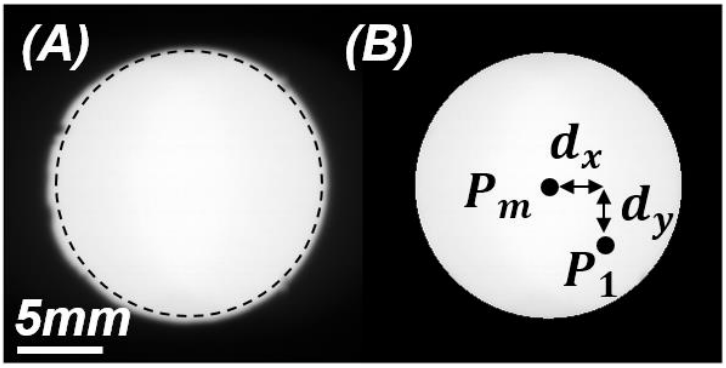

Figure 2-3 Geometric calibration of interior detector offset. (A) The zoom-in interior blank projection. (B) The resultant projection after applying an image mask to subfigure (A). Note that the offset in (B) was exaggerated for illustration purpose. See detailed comments in Sec. 2.3.1.

2.3.3.2 Reconstructions

As to interior micro-CT mode, we utilized our previously published frequency-split displaced detector (FSDDR) reconstruction technique [34]. Briefly, FSDDR algorithm employs a frequency splitting strategy to combine the post-convolution weighting based filtered back projection method (PCW-FBP) with the weighted simultaneous algebraic reconstruction technique (WSART). PCW-FBP incorporates sinogram reflection, sinogram splicing, cosine extrapolation and offset-detector-weighting function to filtered back projection method [34]: sinogram reflection is employed to recover the missing data induced by offset-detector acquisition; sinogram splicing is then applied to smooth out the edge where the measured data are stitched to the recovered data; cosine extrapolation is used to reduce the artifacts induced by interior mode acquisition; the recovered data is

discarded after applying Ram-Lak filter, and offset-detector-weighting function is then applied to the data redundancy induced by offset-detector acquisition. For WSART, the conventional SART algorithm is adapted for detector offset, by multiplying the offset-detector-weighting function [34]: the offset-detector-weighting function is multiplied with the correction term in the formula of SART algorithm. Furthermore, total variation minimization (TVM) and ordered subset (OS) were also combined with WSART to guarantee theoretically accurate solution [20]. Finally, the frequency splitting scheme was applied to combine low frequency components and high frequency components respectively from the reconstruction results of PCW-FBP and WSART. For volumetric reconstruction, a GPU-based acceleration technique was utilized to significantly reduce the computational time [38]. As to global micro-CT mode, the conventional FDK algorithm [39] was employed for image reconstruction (referred to as global-FDK-reference images). The reason is that the FDK algorithm is typically utilized as the surrogate truth in current micro-CT applications [17, 30]. In addition, FSDDR algorithm was also applied in global micro-CT mode (referred to as global-FSDDR-reference images) in order to provide a complementary evaluation of image quality by excluding the influence from different reconstruction algorithms.

2.3.4 Evaluation methods

2.3.4.1 Image quality analysis

Interior micro-CT images were compared against the global micro-CT images. All reconstructed images were calibrated to Hounsfield unit (HU) scale by using water

phantom datasets. Three image quality metrics were employed for the quantitative assessment, including CNR, root mean square error (RMSE) and mean structural similarity index (MSSIM). Water phantom datasets were used to evaluate CNR. As is shown in Figure 2-4, two circular ROIs were respectively selected from air region (i.e. ROI1) and water region (i.e. ROI2) to calculate CNR. The CNR is defined as follows [40, 41]:

$$CNR = \frac{|\mu_1 - \mu_2|}{\sqrt{\sigma_1^2 + \sigma_2^2}} \tag{1}$$

where μ_1 and μ_2 are respectively the average pixel value from ROI1 and ROI2, σ_1^2 and σ_2^2 are the corresponding variance. RMSE and MSSIM were calculated for all datasets to evaluate reconstruction accuracy. The RMSE is defined as follows:

$$RMSE = \sqrt{\frac{\sum|g(x,y) - f(x,y)|^2}{N}} \tag{2}$$

where N is the number of image pixels within the entire interior FOV, $g(x,y)$ is a pixel from interior micro-CT images, and $f(x,y)$ is the counterpart from global micro-CT images. The MSSIM is defined as follows [42]:

$$MSSIM = \frac{1}{M}\sum_{j=1}^{M}\left[l(x_j,y_j)\right]^{\alpha}\left[c(x_j,y_j)\right]^{\beta}\left[s(x_j,y_j)\right]^{\gamma} \tag{3}$$

where M is the number of local windows, x_j and y_j stand for the two groups of pixels in the jth local window from global micro-CT images and interior micro-CT images respectively, $l(x_j,y_j)$, $c(x_j,y_j)$, and $s(x_j,y_j)$ are respectively the comparison function for luminance, contrast, and structure. α , β and γ are parameters for adjusting relative

importance of three comparison functions. These parameters were fixed at the same values in [42].

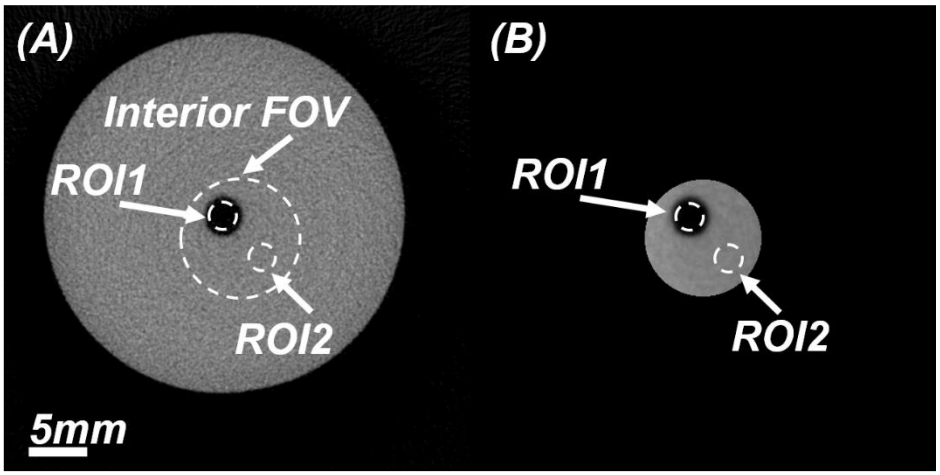

Figure 2-4 Position of ROIs for CNR evaluation in water phantom datasets. ROI1 - air region. ROI2 - water region. (A) Global micro-CT image. (B) Interior micro-CT image. The region outside FOVs was cropped out by using image support. Display window [-1000 1000] HU.

2.3.4.2 Radiation dose measurement

We adapted the methods from the reference [23] to evaluate radiation dose reduction. Due to lack of standard phantom for micro-CT, we fabricated two acrylic micro-CT dose phantoms for radiation dose measurement (Figure 2-5A). The diameter and the length of the phantoms were respectively fixed at 30mm and 110mm which were the approximate size of the commercial micro-CT dose phantom (QRM, Inc. Germany). One phantom has a peripheral bore hole (i.e. phantom 1) and the other has a central bore hole (i.e. phantom 2). Due to lack of small thermoluminescent dosimeters (TLD) and micro-ion chambers, a

calibrated 100mm pencil ion chamber (Model 10X5-3CT, *Radcal*, Inc.) was placed in the micro-CT dose phantoms to measure the accumulated radiation exposures at the five positions throughout the scans (Figure 2-5B). The scan protocol in Table 2-1 was also used in the dose measurement. The phantom 2 was used to measure the radiation dose in the central position (i.e. position #5). The phantom 1 was used to measure the radiation dose in peripheral positions (i.e. positions #1 - #4). Note that phantom 1 was rotated to next position after radiation dose measurement was accomplished at current position.

We adopted the concepts of $CTDI_a$ from the references [43-45] to evaluate the average radiation dose across the nominal beam width. The formula of $CTDI_a$ is defined as follows:

$$CTDI_a = \frac{1}{a}\int_{-50mm}^{50mm} f(z)dz \tag{4}$$

where a is the nominal beam width along z-axis, and $f(z)$ is the radiation dose profile along z-axis. The weighted $CTDI_a$ is calculated as follows:

$$CTDI_{a,w} = \frac{2}{3}CTDI_a^{periphery} + \frac{1}{3}CTDI_a^{central} \tag{5}$$

Where $CTDI_a^{periphery}$ is the average dose at peripheral positions, and $CTDI_a^{central}$ is the dose at central position. The dose length product (DLP) was employed as the descriptor of total dose [44]:

$$DLP = CTDI_{a,w} \times a \tag{6}$$

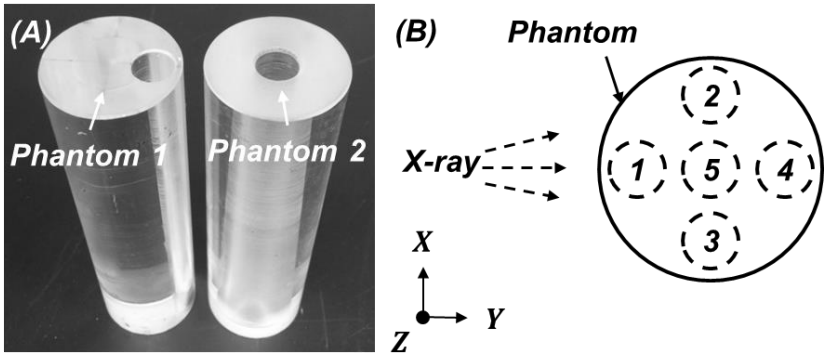

Figure 2-5 (A) The in-house-built micro-CT dose phantoms. (B) Schematic five positions (top view) where ion chamber was placed in the phantoms.

2.4 Experimental results

2.4.1 Imaging results

Figure 2-6 demonstrates the comparison between global-FDK-reference images and interior micro-CT images of water phantom. By visual inspection, FSDDR algorithm suppressed the image noise of interior micro-CT images, while FDK algorithm yielded higher image noise in global micro-CT images. This is because FSDDR algorithm employs compressive sensing (CS) based iterative reconstruction technique which enables the noise reduction in piecewise constant type phantom. The image differences mainly demonstrated noise-like pattern. Table 2-2 demonstrated the value of CNR, RMSE and MSSIM from water phantom datasets. The mean CNR of global micro-CT images was 55% lower than that of interior micro-CT images. The mean RMSE of three slices was 103.5HU. High structural similarity index was observed as one would expect. The mean MSSIM of three slices was 0.9173.

Figure 2-7 demonstrated the comparison between global-FDK-reference images and interior micro-CT images of “multi-feature” phantom. By visual inspection, the low contrast line-shape structures at the bottom of interior micro-CT images are slightly weakened. This can be attributed to the TVM method which could reduce the image noise at the expense of smoothing out small structures [46]. Nevertheless, the high and low contrast structures of the phantom remain largely consistent in the images from both modes, and no significant artifacts are induced in interior micro-CT images. The image differences also mainly demonstrated noise-like pattern. The line profiles from interior micro-CT images were well-matched to those from global micro-CT images. Table 2-2 also demonstrated the RMSE and the MSSIM from multi-feature phantom datasets. High structural-similarity-index was still observed. The mean MSSIM of three slices was 0.9294. Despite the heterogeneous inner materials and the sub-millimeter structure, interior micro-CT images still presented high structural similarity to global micro-CT images.

Figure 2-8 presents the comparison between global-FDK-reference images and interior micro-CT images of mouse carcass. By visual inspection, FDK algorithm yielded visible streak artifacts in global micro-CT images, which was mainly induced by bony structure and iodine contrast agent. The streak artifacts had degraded image contrast. On the contrary, FSDDR algorithm suppressed the artifacts and enhanced the image contrast. The suppression of streak artifacts by the FSDDR algorithm could be attributed to the following reasons. First, CS based iterative reconstruction technique has been demonstrated to suppress streak artifacts [47, 48]. Second, the frequency splitting scheme allows adjusting

the contribution of analytic reconstruction (i.e. PCW-FBP) and CS based iterative reconstruction (i.e. WSART). Briefly, it could combine less low frequency components from PCW-FBP with more high frequency components from WSART to constitute the reconstruction results of FSDDR algorithm, by using proper image filtering. More details can be referred to in reference [34]. Therefore, the streak artifacts could be reduced by using frequency-split scheme, although some amount of residual could be present. The image differences and line profiles demonstrated relatively larger discrepancy. Table 2-2 also demonstrated the RMSE and the MSSIM from mouse carcass datasets. The mean RMSE of three slices was 587.76HU. Despite higher RMSE, the structural similarity index was maintained at a relatively high level. The mean MSSIM of three slices was 0.8624. Figure 2-9 shows the comparison of other representative axial, coronal, and sagittal slices and volume rendering between interior and global-FDK-reference images. The anatomical structure such as blood vessels (as marked by solid arrows) and heart chambers still demonstrated high visual fidelity.

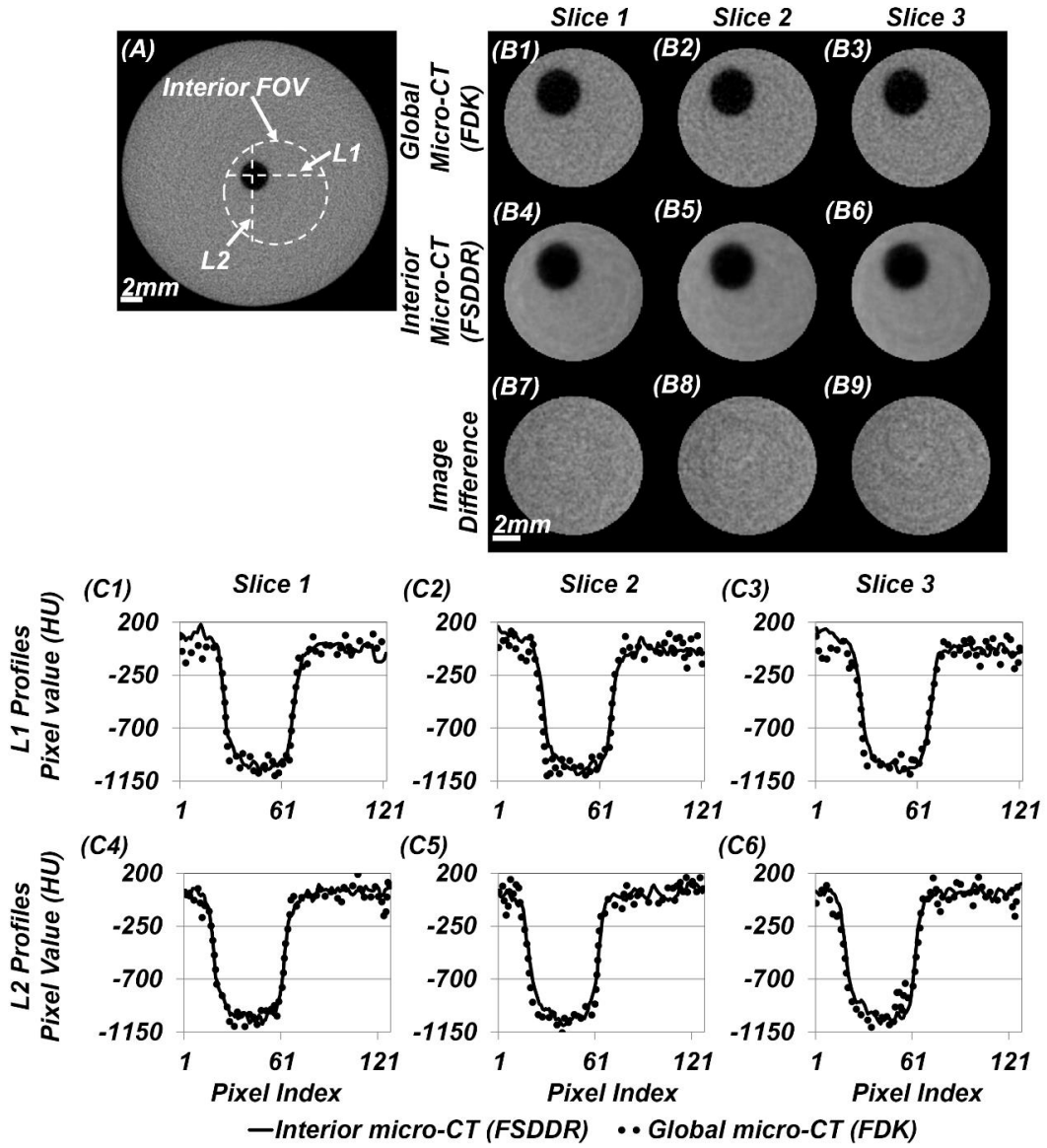

Figure 2-6. The comparison between global-FDK-reference images and interior micro-CT images (axial slices) of water phantom. The region outside the FOV was cropped out by image support. (A) The location of interior FOV and line profiles. (B1-B3) Global micro-CT images. (B4-B6) Interior micro-CT images. (B7-B9) Image differences. Slice 2 is the central slice. Slices 1 & 3 are two off-mid-plane slices (0.26 mm away from the slice 2). (C1-C6) Line profiles from each slice. Display window is [-1000 1000] HU.

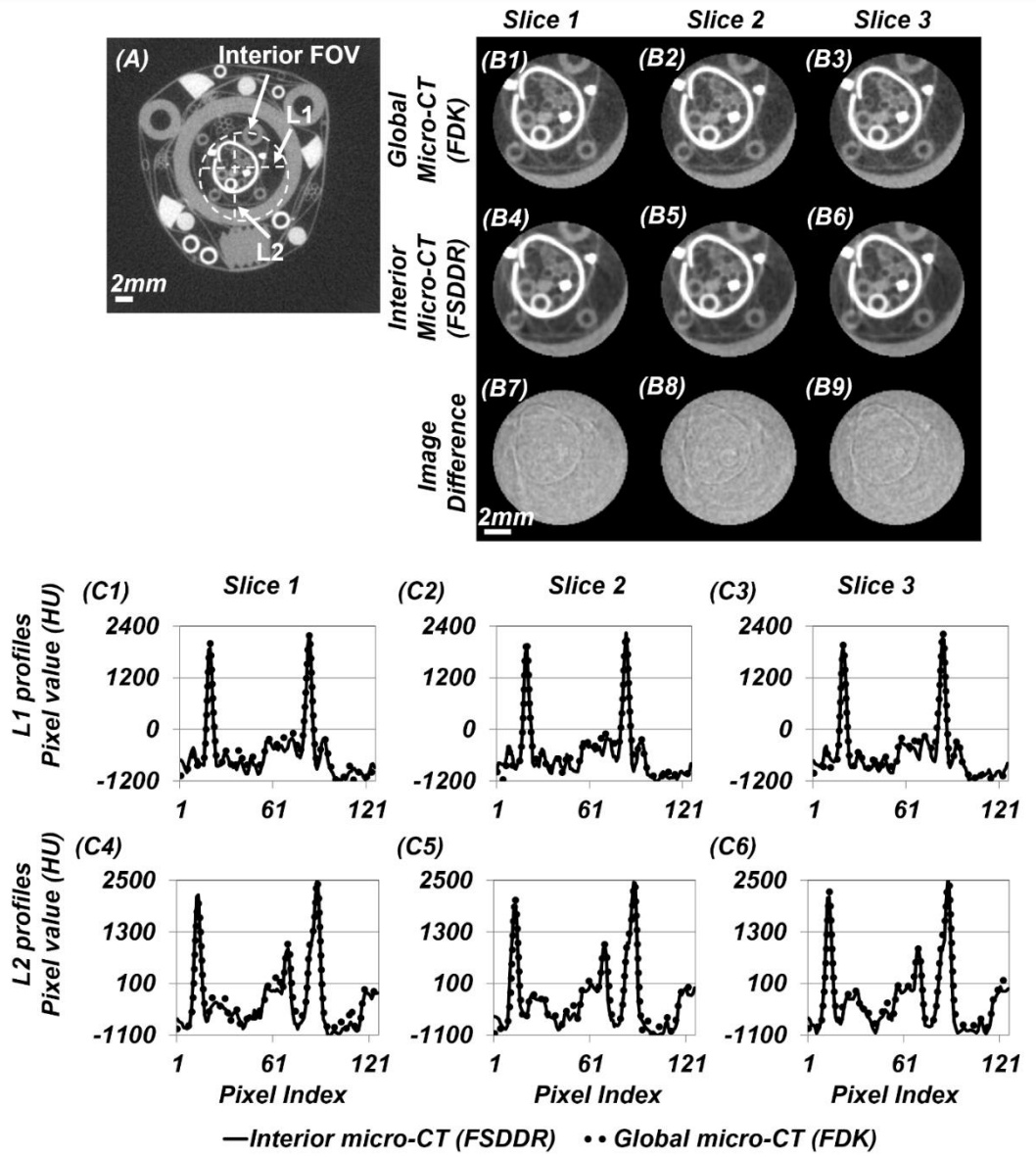

Figure 2-7. The comparison between global-FDK-reference images and interior micro-CT images (axial slices) of multi-feature phantom. The region outside the FOV was cropped out by image support. (A) The location of interior FOV and line profiles. (B1-B3) Global micro-CT images. (B4-B6) Interior micro-CT images. (B7-B9) Image differences. Slice 2 is the central slice. Slices 1 & 3 are two off-mid-plane slices (0.26 mm away from the slice 2). (C1-C6) Line profiles from each slice. Display window is [-1700 1000] HU.

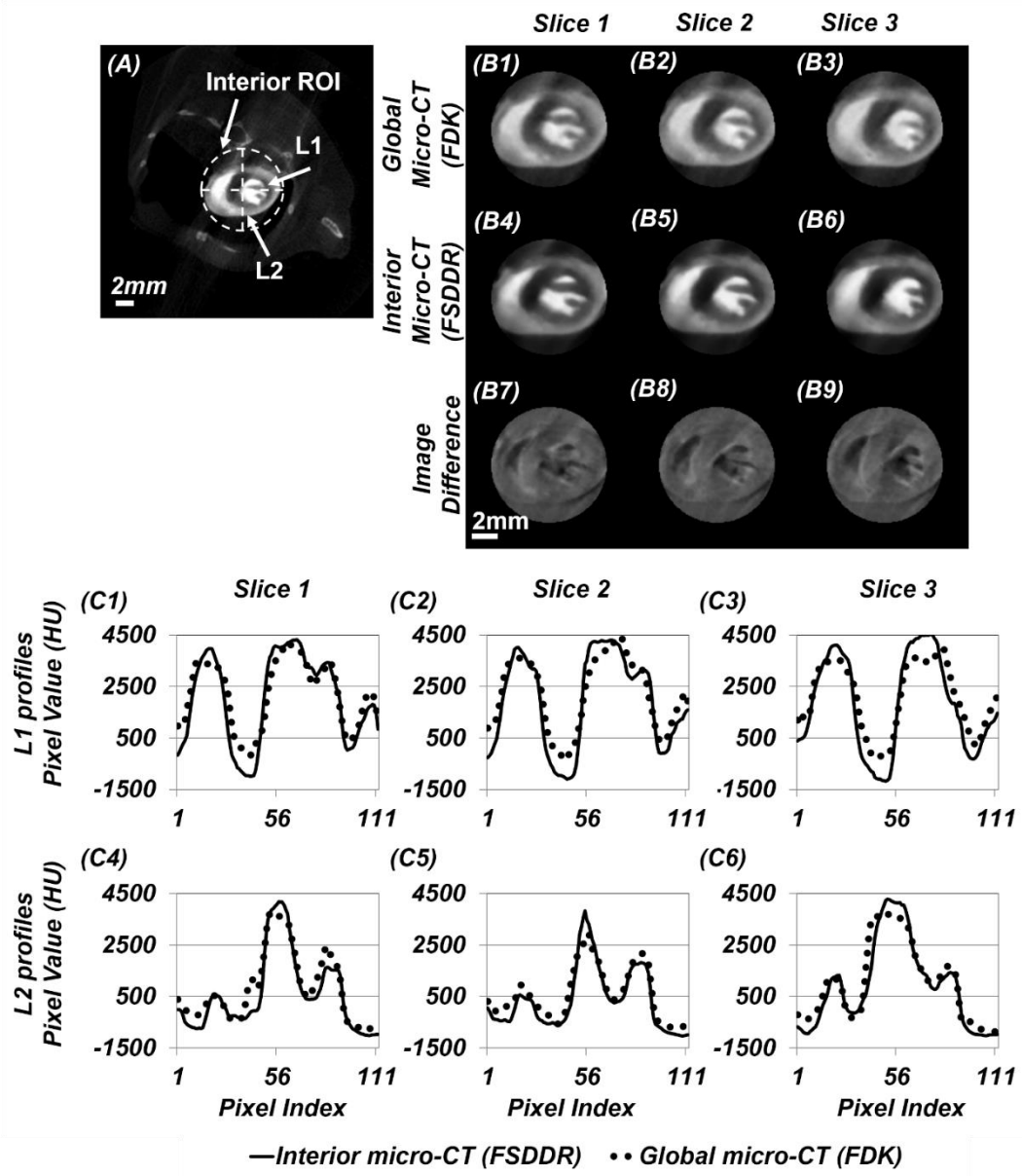

Figure 2-8. The comparison between global-FDK-reference images and interior micro-CT images (axial slices) of mouse carcass. The region outside the ROI was cropped out by image support. (A) The location of interior ROI and line profiles. (B1-B3) Global micro-CT images. (B4-B6) Interior micro-CT images. (B7-B9) Image differences. Slice 2 is the central slice. Slices 1 & 3 are two off-mid-plane slices (0.26 mm away from the slice 2). (C1-C6) Line profiles from each slice. Display window is [-1500 4500] HU.

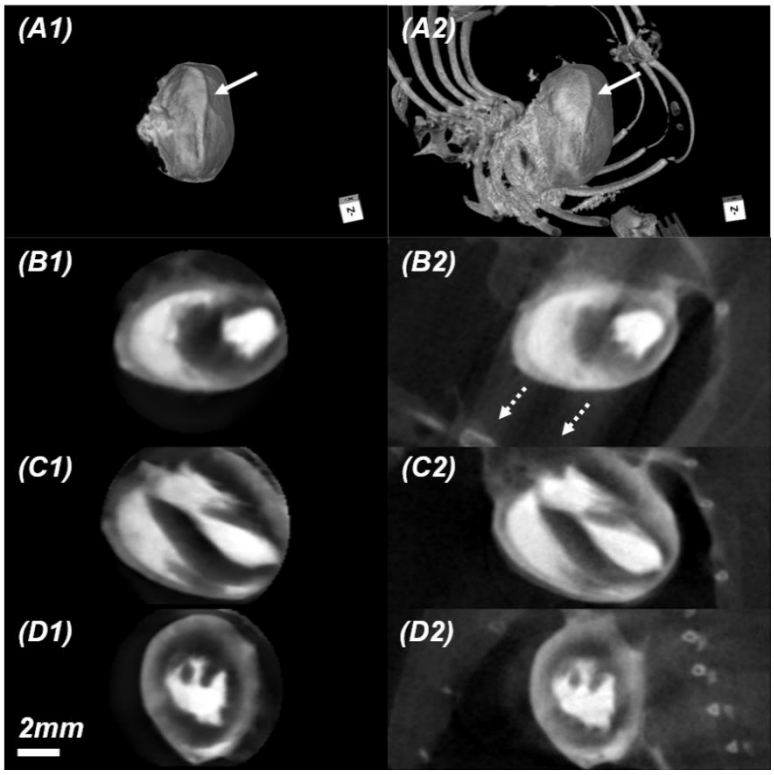

Figure 2-9. The volume rendering and reconstructed images of mouse carcass. Left column: interior micro-CT images. Right column: global micro-CT images (FDK). (A1-A2): Volume rendering generated from Volview (Kitware, Inc. USA). (B1-B2) Axial slices. (C1-C2) Coronal slices. (D1-D2) Sagittal slices. The solid arrows in (A1-A2) indicate blood vessels. The dash arrows in (B2) indicate the direction of streak artifacts. Display window [-1500 4000] HU.

Table 2-2 Quantitative quality metrics

		Global-FDK-reference images				Interior micro-CT images			
	Quality Metrics	Slice 1	Slice 2	Slice 3	Mean Value	Slice 1	Slice 2	Slice 3	Mean Value
Water phantom	CNR	8.83	9.35	8.77	8.98	20.13	20.44	19.08	19.88
	RMSE (HU)	-	-	-	-	99.28	104.1	107.11	103.50
	MSSIM	-	-	-	-	0.9191	0.9166	0.9162	0.9173
Multi-feature phantom	RMSE (HU)	-	-	-	-	150.48	150.50	153.74	151.57
	MSSIM	-	-	-	-	0.9346	0.9272	0.9263	0.9294
Mouse carcass	RMSE (HU)	-	-	-	-	572.75	580.75	609.79	587.76
	MSSIM	-	-	-	-	0.8663	0.8681	0.8527	0.8624

Figure 2-10 presents the comparison between global-FSDDR-reference images and interior micro-CT images of the three aforementioned samples. By visual inspection, global and interior micro-CT modes demonstrated comparable image quality in terms of image noise, contrast and structural similarity. In water phantom dataset, the CNR of global-FSDDR-reference image was 18.5, which was close to that of interior micro-CT images (see Table 2-2). Higher structural similarity index was also observed. The MSSIM was respectively 0.9330, 0.9614 and 0.8939 for water phantom, "multi-feature" phantom and mouse carcass.

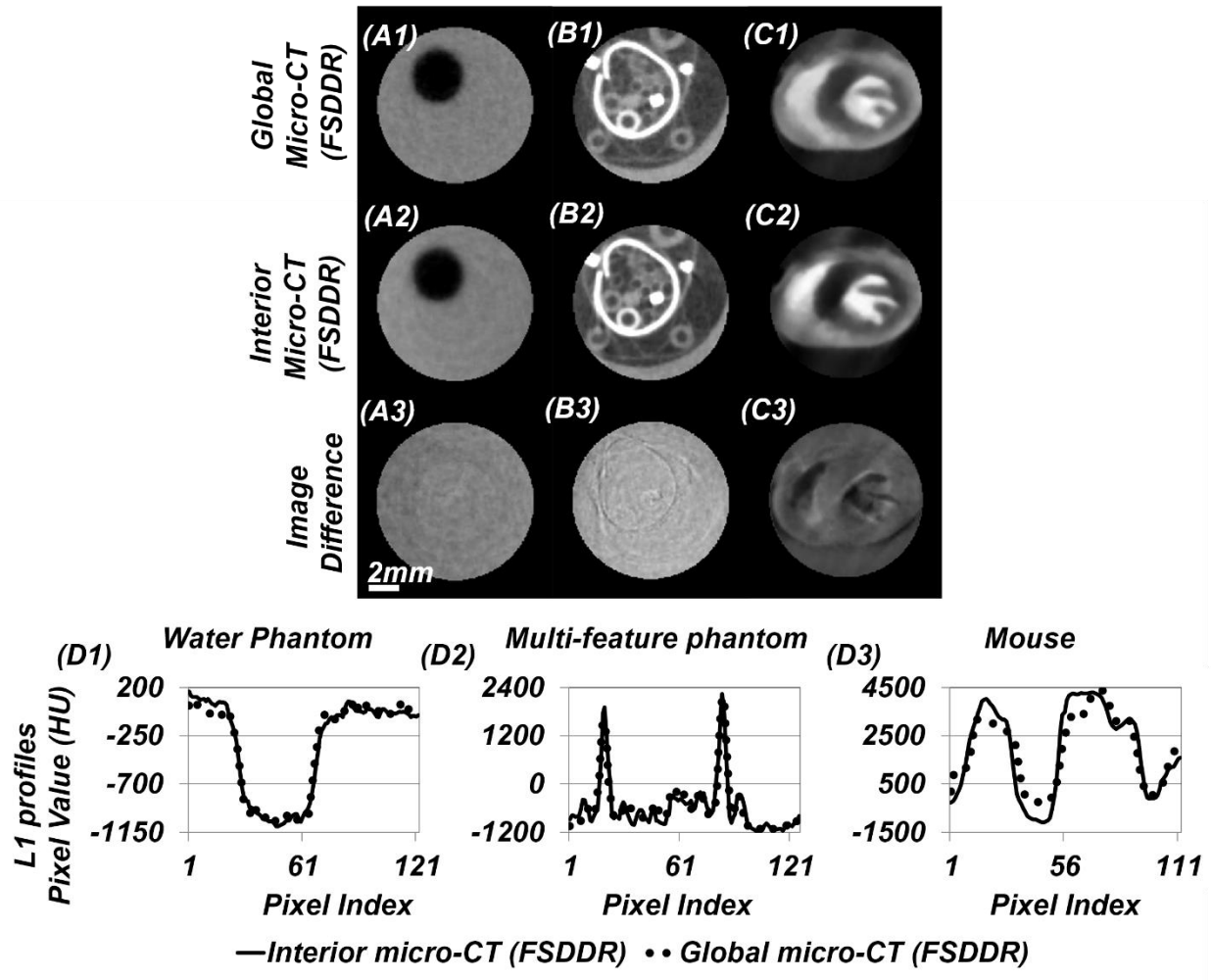

Figure 2-10 the comparison between global-FSDDR-reference images and interior micro-CT images (central slices) of the three samples. (A1) - (A3) water phantom. (B1) - (B3) multi-feature phantom. (C1) - (C3) mouse carcass. Display window: (A1)-(A3) [-1000 1000] HU, (B1)-(B3) [-1700 1000] HU, (C1)-(C3) [-1500 4500] HU. (D1) - (D3) L1 line profiles from each slice. The locations of L1 line profiles are illustrated in the above figures (from Figure 2-6 to Figure 2-8).

2.4.2 Radiation dose

The results of radiation dose measurement are demonstrated in Table 2-3. Interior micro-CT mode demonstrated significantly less radiation dose than global micro-CT mode. Significant dose reduction was observed at the peripheral positions (up to 65.9%). As is expected, the percentage dose reduction was higher at the peripheral positions than at the center (up to 8.6%). Unlike the central region, the peripheral region was only partially irradiated by the collimated X-ray cone beam during interior micro-CT scan. The dose reduction in both central and peripheral region leads to overall dose reduction. Compared with global micro-CT mode, interior micro-CT mode demonstrated significant percentage reduction of $CTDI_{a,w}$ (up to 48%) and DLP (up to 83.9%).

Table 2-3 $\boldsymbol{CTDI_a}$ *(cGy) at positions #1 - #5,* $\boldsymbol{CTDI_{a,w}}$ *(cGy) and DLP (cGy-cm)*

	#1	#2	#3	#4	#5	$CTDI_{a,w}$	DLP
Global micro-CT	16.340	16.275	16.189	16.297	14.135	15.562	37.706
Interior micro-CT	5.566	5.578	5.664	5.871	12.919	8.086	6.066
Percentage reduction (%)	65.9	65.7	65.0	64.0	8.60	48.0	83.9

2.5 Discussion and conclusion

In this study, we used a source collimator to implement interior ROI imaging in a CNT X-ray source based micro-CT system. We conducted global and interior micro-CT scans on two micro-CT phantoms and a sacrificed mouse to evaluate the system performance. An

iterative reconstruction algorithm (FSDDR) was employed for interior ROI reconstruction. Visual inspection and quantitative analysis were carried out to evaluate the image quality. Moreover, we experimentally measured and compared the radiation dose from global and interior micro-CT.

The influence of source collimators on interior ROI imaging has been overlooked in previous cone-beam CT studies [49]. As is reported by D. Xue *et. al.* [49], the source collimator can induce non-negligible penumbra effects and reduction of primary X-ray field intensity in a clinical cone-beam CT, which mainly results from the off-focal-spot radiation and the large geometric magnification from collimator plane to detector plane. The similar effects were observed in our interior micro-CT system. Despite the same geometry magnifications for the global and interior micro-CT modes in our system, the central X-ray ray intensity dropped about 10% from the global mode to interior mode. We attributed this reduction of the central ray intensity to the aperture collimator at the source, which can reduce the off-focal-spot radiations. In interior micro-CT, the X-ray intensity of the primary field decreases radially from the center toward the edge (up to about 5%). This can be explained by the penumbra effects caused by the interior collimator. Overall, the changes of primary X-ray field intensity can result in reconstruction error for interior ROI imaging [49]. To eliminate such error, interior raw projections have to be normalized by the corresponding interior blank projections in the preprocessing step.

The concept of CTDI was adopted as a micro-CT dose descriptor, because it has demonstrated linear response to the parametric changes of micro-CT scan protocols [45].

Moreover, CTDI was also used in dose measurement of interior clinical CT by D. Bharkhada et al [23]. Furthermore, the concept of $CTDI_a$ was utilized instead of conventional $CTDI_{100}$, since our micro-CT system conducts cone-beam circular scans [44]. On the other hand, we have noticed that partial irradiation of ion chamber in interior micro-CT should cause some uncertainty to the measured $CTDI_a$ and DLP. Furthermore, the holes of 9.5mm diameter may cause some uncertainties on dose measurement in the 20mm to 30mm diameter phantoms [50]. Nonetheless, our dose measurement should allow us to gauge the radiation dose reduction in this work.

In conclusion, we have demonstrated that interior ROI imaging can be implemented for radiation dose reduction in micro-CT imaging by mounting a source collimator. Using such a micro-CT scanner, we conducted comprehensive analysis of imaging quality and measured the radiation dose when the micro-CT system was applied for imaging physical phantoms and mouse carcass in both the conventional global micro-CT mode and the interior micro-CT mode. Interior micro-CT has been demonstrated to have comparable image quality to conventional global micro-CT, while significantly reducing radiation dose. We conclude that our CNT X-ray source based interior micro-CT system is applicable for high-quality and low-dose ROI-oriented preclinical imaging.

References

[1] E. L. Ritman, "Current status of developments and applications of micro-CT," *Annual review of biomedical engineering*, vol. 13, pp. 531-552, 2011.

[2] A. Y. Sheikh, K. E. A. van der Bogt, T. C. Doyle, M. K. Sheikh, K. J. Ransohoff, Z. A. Ali, *et al.*, "Micro-CT for Characterization of Murine CV Disease Models," *JACC: Cardiovascular Imaging*, vol. 3, pp. 783-785, 2010.

[3] R. Meuwissen and A. Berns, "Mouse models for human lung cancer," *Genes Dev*, vol. 19, pp. 643-64, Mar 15 2005.

[4] O. Engel, S. Kolodziej, U. Dirnagl, and V. Prinz, "Modeling Stroke in Mice - Middle Cerebral Artery Occlusion with the Filament Model," *Journal of Visualized Experiments : JoVE*, p. 2423, 2011.

[5] C. T. Badea, M. Drangova, D. W. Holdsworth, and G. A. Johnson, "In Vivo Small Animal Imaging using Micro-CT and Digital Subtraction Angiography," *Physics in medicine and biology*, vol. 53, pp. R319-R350, 08/29 2008.

[6] N. L. Ford, M. M. Thornton, and D. W. Holdsworth, "Fundamental image quality limits for microcomputed tomography in small animals," *Medical Physics*, vol. 30, pp. 2869-2877, 2003.

[7] R. A. Brooks and G. Di Chiro, "Statistical limitations in x-ray reconstructive tomography," *Medical physics*, vol. 3, pp. 237-240, 1976.

[8] T. Ohnishi, A. Takahashi, K. Ohnishi, and M. Yonezawa, "Tumor suppressor p53 response is blunted by low-dose radiation," *Phys Med*, vol. 17 Suppl 1, pp. 215-6, 2001.

[9] S. L. Chen, L. Cai, Q. Y. Meng, S. Xu, H. Wan, and S. Z. Liu, "Low-Dose Whole-Body Irradiation (LD-WBI) Changes Protein Expression of Mouse Thymocytes: Effect of a LD-WBI-Enhanced Protein RIP10 on Cell Proliferation and Spontaneous or Radiation-Induced Thymocyte Apoptosis," *Toxicological Sciences*, vol. 55, pp. 97-106, May 1, 2000 2000.

[10] E. Flockerzi, S. Schanz, and C. E. Rübe, "Even low doses of radiation lead to DNA damage accumulation in lung tissue according to the genetically-defined DNA repair capacity," *Radiotherapy and Oncology*, vol. 111, pp. 212-218, 2014.

[11] D. Mathias, R. E. J. Mitchel, M. Barclay, H. Wyatt, M. Bugden, N. D. Priest, *et al.*, "Low-Dose Irradiation Affects Expression of Inflammatory Markers in the Heart of ApoE -/- Mice," *PLoS One*, vol. 10, p. e0119661, 2015.

[12] V. Kersemans, J. Thompson, B. Cornelissen, M. Woodcock, P. D. Allen, N. Buls, *et al.*, "Micro-CT for Anatomic Referencing in PET and SPECT: Radiation Dose, Biologic Damage, and Image Quality," *Journal of Nuclear Medicine*, vol. 52, pp. 1827-1833, November 1, 2011 2011.

[13] R. Laforest, C. Waterson, S. Broski, and J. Lewis, "Radiation dose considerations in tumor growth monitoring with CT," *Mol Imaging*, vol. 3, p. 288, 2004.

[14] K. M. Prise, "New advances in radiation biology," *Occupational Medicine*, vol. 56, pp. 156-161, May 1, 2006 2006.

[15] W. P. Shuman, D. E. Green, J. M. Busey, O. Kolokythas, L. M. Mitsumori, K. M. Koprowicz, *et al.*, "Model-based iterative reconstruction versus adaptive statistical iterative reconstruction and filtered back projection in liver 64-MDCT: focal lesion detection, lesion conspicuity, and image noise," *AJR Am J Roentgenol,* vol. 200, pp. 1071-6, May 2013.

[16] Q. Xu, H. Yu, X. Mou, L. Zhang, J. Hsieh, and G. Wang, "Low-dose x-ray ct reconstruction via dictionary learning," *Medical Imaging, IEEE Transactions on,* vol. 31, pp. 1682-1697, 2012.

[17] X. Han, J. Bian, D. R. Eaker, T. L. Kline, E. Y. Sidky, E. L. Ritman, *et al.*, "Algorithm-enabled low-dose micro-CT imaging," *Medical Imaging, IEEE Transactions on,* vol. 30, pp. 606-620, 2011.

[18] Y. Lu, J. Zhao, and G. Wang, "Few-view image reconstruction with dual dictionaries," *Physics in medicine and biology,* vol. 57, p. 173, 2012.

[19] E. Y. Sidky, C.-M. Kao, and X. Pan, "Accurate image reconstruction from few-views and limited-angle data in divergent-beam CT," *Journal of X-ray Science and Technology,* vol. 14, pp. 119-139, 2006.

[20] H. Yu and G. Wang, "Compressed sensing based interior tomography," *Physics in medicine and biology,* vol. 54, p. 2791, 2009.

[21] G. Wang and H. Yu, "The meaning of interior tomography," *Physics in medicine and biology,* vol. 58, p. R161, 2013.

[22] Q. Xu, X. Mou, G. Wang, J. Sieren, E. A. Hoffman, and H. Yu, "Statistical interior tomography," *Medical Imaging, IEEE Transactions on,* vol. 30, pp. 1116-1128, 2011.

[23] D. Bharkhada, H. Yu, R. Dixon, Y. Wei, J. J. Carr, J. D. Bourland, *et al.*, "Demonstration of Dose and Scatter Reductions for Interior Computed Tomography," *Journal of computer assisted tomography,* vol. 33, p. 967, 2009.

[24] Y. Shen, Y. Yi, Y. Zhong, C. J. Lai, X. Liu, Z. You, *et al.*, "High resolution dual detector volume-of-interest cone beam breast CT--Demonstration with a bench top system," *Med Phys,* vol. 38, pp. 6429-42, Dec 2011.

[25] D. Kolditz, Y. Kyriakou, and W. A. Kalender, "Volume-of-interest (VOI) imaging in C-arm flat-detector CT for high image quality at reduced dose," *Med Phys,* vol. 37, pp. 2719-30, Jun 2010.

[26] L. Chen, C. C. Shaw, M. C. Altunbas, C.-J. Lai, X. Liu, T. Han, *et al.*, "Feasibility of volume-of-interest (VOI) scanning technique in cone beam breast CT—a preliminary study," *Medical Physics,* vol. 35, pp. 3482-3490, 2008.

[27] R. Chityala, K. R. Hoffmann, S. Rudin, and D. R. Bednarek, "Region of interest (ROI) computed tomography (CT): Comparison with full field of view (FFOV) and truncated CT for a human head phantom," *Proceedings - Society of Photo-Optical Instrumentation Engineers,* vol. 5745, pp. 583-590, 2005.

[28] C. J. Lai, L. Chen, H. Zhang, X. Liu, Y. Zhong, Y. Shen, *et al.*, "Reduction in x-ray scatter and radiation dose for volume-of-interest (VOI) cone-beam breast CT--a phantom study," *Phys Med Biol,* vol. 54, pp. 6691-709, Nov 7 2009.

[29] J. Bian, X. Han, E. Y. Sidky, G. Cao, J. Lu, O. Zhou, *et al.*, "Investigation of sparse data mouse imaging using micro-CT with a carbon-nanotube-based X-ray source," *Tsinghua Science & Technology,* vol. 15, pp. 74-78, 2010.
[30] H. Yu, G. Cao, L. Burk, Y. Lee, J. Lu, P. Santago, *et al.*, "Compressive sampling based interior reconstruction for dynamic carbon nanotube micro-CT," *Journal of X-ray Science and Technology,* vol. 17, pp. 295-303, 2009.
[31] E. Katsevich, A. Katsevich, and G. Wang, "Stability of the interior problem with polynomial attenuation in the region of interest," *Inverse problems,* vol. 28, p. 065022, 2012.
[32] H. Kudo, M. Courdurier, F. Noo, and M. Defrise, "Tiny a priori knowledge solves the interior problem in computed tomography," *Physics in medicine and biology,* vol. 53, p. 2207, 2008.
[33] S. Tang, Y. Yang, and X. Tang, "Practical interior tomography with radial Hilbert filtering and a priori knowledge in a small round area," *Journal of X-ray science and technology,* vol. 20, pp. 405-422, 2012.
[34] K. S. Sharma, H. Gong, O. Ghasemalizadeh, H. Yu, G. Wang, and G. Cao, "Interior micro-CT with an offset detector," *Medical Physics,* vol. 41, pp. -, 2014.
[35] K. S. Sharma, C. Holzner, D. M. Vasilescu, X. Jin, S. Narayanan, M. Agah, *et al.*, "Scout-view assisted interior micro-CT," *Physics in medicine and biology,* vol. 58, p. 4297, 2013.
[36] G. Cao, L. M. Burk, Y. Z. Lee, X. Calderon-Colon, S. Sultana, J. Lu, *et al.*, "Prospective-gated cardiac micro-CT imaging of free-breathing mice using carbon nanotube field emission x-ray," *Med Phys,* vol. 37, pp. 5306-12, Oct 2010.
[37] F. Noo, R. Clackdoyle, C. Mennessier, T. A. White, and T. J. Roney, "Analytic method based on identification of ellipse parameters for scanner calibration in cone-beam tomography," *Physics in Medicine and Biology,* vol. 45, p. 3489, 2000.
[38] L. Rui, L. Yan, and Y. Hengyong, "GPU-Based Acceleration for Interior Tomography," *Access, IEEE,* vol. 2, pp. 757-770, 2014.
[39] L. Feldkamp, L. Davis, and J. Kress, "Practical cone-beam algorithm," *JOSA A,* vol. 1, pp. 612-619, 1984.
[40] M. E. Mullins, M. H. Lev, P. Bove, C. E. O'Reilly, S. Saini, J. T. Rhea, *et al.*, "Comparison of Image Quality Between Conventional and Low-Dose Nonenhanced Head CT," *American Journal of Neuroradiology,* vol. 25, pp. 533-538, April 1, 2004 2004.
[41] J. Stützel, U. Oelfke, and S. Nill, "A quantitative image quality comparison of four different image guided radiotherapy devices," *Radiotherapy and Oncology,* vol. 86, pp. 20-24, 2008.
[42] Z. Wang, A. C. Bovik, H. R. Sheikh, and E. P. Simoncelli, "Image quality assessment: from error visibility to structural similarity," *Image Processing, IEEE Transactions on,* vol. 13, pp. 600-612, 2004.
[43] R. L. Dixon and J. M. Boone, "Cone beam CT dosimetry: a unified and self-consistent approach including all scan modalities--with or without phantom motion," *Med Phys,* vol. 37, pp. 2703-18, Jun 2010.

[44] S. Kim, H. Song, E. Samei, F.-F. Yin, and T. T. Yoshizumi, *Computed tomography dose index and dose length product for cone-beam CT: Monte Carlo simulations* vol. 12, 2011.
[45] M. Hupfer, D. Kolditz, T. Nowak, F. Eisa, R. Brauweiler, and W. A. Kalender, "Dosimetry concepts for scanner quality assurance and tissue dose assessment in micro-CT," *Medical Physics*, vol. 39, pp. 658-670, 2012.
[46] Z. Tian, X. Jia, K. Yuan, T. Pan, and S. B. Jiang, "Low Dose CT Reconstruction via Edge-preserving Total Variation Regularization," *Physics in medicine and biology*, vol. 56, pp. 5949-5967, 08/22 2011.
[47] Z. Zhu, K. Wahid, P. Babyn, D. Cooper, I. Pratt, and Y. Carter, "Improved Compressed Sensing-Based Algorithm for Sparse-View CT Image Reconstruction," *Computational and Mathematical Methods in Medicine*, vol. 2013, p. 15, 2013.
[48] X. Li and S. Luo, "A compressed sensing-based iterative algorithm for CT reconstruction and its possible application to phase contrast imaging," *BioMedical Engineering OnLine*, vol. 10, pp. 73-73, 2011.
[49] X. Dong, T. Niu, X. Jia, and L. Zhu, "Relationship between x-ray illumination field size and flat field intensity and its impacts on x-ray imaging," *Medical physics*, vol. 39, pp. 5901-5909, 2012.
[50] J. M. Boone, O. Velazquez, and S. R. Cherry, "Small-animal X-ray dose from micro-CT," *Molecular imaging*, vol. 3, pp. 149-158, 2004.

Chapter 3 Hardware based X-ray scatter correction for multi-source interior computed tomography

Hao Gong[1], Hao Yan[2], Xun Jia[2], Bin Li[2], Ge Wang[3], Guohua Cao[1]

[1]Department of Biomedical Engineering and Mechanics, Virginia Polytechnic Institute and State University, Blacksburg, VA, 24061, USA

[2]Department of Radiation Oncology, University of Texas Southwestern Medical Center, Dallas, TX, 75390, USA

[3]Department of Biomedical Engineering, Biomedical Imaging Center, Center for Biotechnology and Interdisciplinary Studies, Rensselaer Polytechnic Institute, Troy, NY, 12180, USA

Publication information – The major contents of this chapter were published as: Hao Gong, Hao Yan, Xun Jia, Bin Li, Ge Wang, Guohua Cao. (2017), "X-ray scatter correction for multi-source interior computed tomography", ***Medical Physics***, 44: 71–83. doi:10.1002/mp.12022. https://www.ncbi.nlm.nih.gov/pubmed/28102959

3.1 Abstract

The schemes of multi-source interior computed tomography (CT) have shown promise for ultra-fast, organ-oriented, and low-dose dynamic imaging. Besides forward scattering, X-ray cross scattering from multiple X-ray sources activated simultaneously can further

degrade image quality. Here, we investigate the overall X-ray scattering artifact in a recently proposed multi-source interior CT architecture, and present two methods for scatter correction. Compared to single-source global CT, scattering in multi-source interior CT architecture is affected by two new factors: cross scattering from simultaneously activated multiple X-ray sources and region-of-interest (ROI) oriented interior CT mode. The scatter artifact in the multi-source interior CT architecture was evaluated through both numerical simulation and physical experimentation, and compared to that from conventional single-source global CT. Monte Carlo simulation was conducted with a modified numerical CATphan® 600 phantom. Physical experiments were performed in an in-house developed CT imaging platform with a custom-built phantom. The simulation and experiments were carried out on the single-source CT architecture and the multi-source CT architecture, respectively in the global CT mode and the interior CT mode for comparison. To correct the scattering artifact, two new methods were presented. The first is a beam-stopper-array (BSA) based method, which enables an online correction of forward scattering and cross scattering simultaneously. The second is a source-trigger-sequence (STS) based method dedicated to cross-scatter correction. It enables the on-the-fly measurements of the cross scattering signals at a few pre-selected views. The CT image quality was quantitatively evaluated in terms of contrast-to-noise ratio (CNR) and CT number deviation before and after the scatter correction. X-ray cross scattering degraded image quality in both the simulation and experiments. Before the scatter correction, the multi-source interior CT mode yielded a reduction of CNR at the ROIs by up to 68.5% and 50.7% in the simulation and experiments respectively. The stationary BSA based method

significantly improved CNR and CT number accuracy in the images from multi-source interior CT mode, by reducing the negative effects from both forward scattering and cross scattering. The STS based method enabled multi-source interior CT mode to provide comparable image quality to that with the single-source interior CT mode, by correcting the artifact from cross scattering. The remaining forward scattering artifact can be corrected with the fast adaptive scatter kernel superposition (FASKS) technique. With the proposed scatter correction methods, the CT number error at the ROIs was reduced to less than 37 HU in both simulation and experiments respectively. Cross scattering, in addition to forward scattering, can cause significant image quality degradation in the multi-source interior CT architecture. However, image quality can be significantly improved with the proposed scatter correction methods.

Keywords: Multi-source, interior tomography, forward scattering, cross scattering, scatter correction

3.2 Introduction

Ever since Hounsfield's pioneering work on the first CT [1], improving temporal resolution has been a main driving force behind CT developments. High temporal resolution is desired when CT imaging objects with fast dynamics (e.g., cardiac CT imaging of beating hearts) [2-4]. To obtain high temporal resolution in a CT scanner, the research effort has been focused on the engineering of a gantry with faster rotation speed and an X-ray source with

more power [5]. However, as both the source power and gantry rotation speed are approaching their engineering limits [6], an attractive alternative is multi-source CT.

CT systems with multiple X-ray sources have been long pursued. In a multi-source CT scanner, more than one source-detector imaging chains are operated simultaneously. The rationale is that doubling the number of source-detector chains on a given gantry is two times more efficient in speeding up the temporal resolution than reducing the gantry rotation time [7]. The first multi-source CT prototype, the dynamic spatial reconstructor (DSR), was reported in the 1980s [8]. Now, dual-source CT (DSCT) (Siemens SOMATOM) that fixes two X-ray sources and two detectors in one gantry is routinely implemented in clinical applications [9, 10].

Several other conceptual multi-source CT schemes have been explored recently. Liu *et. al.* demonstrated the improved image quality in a simulated five-source cone-beam micro-CT with a Feldkamp-type reconstruction algorithm [11]. Zhao *et. al.* proposed a triple-source helical / saddle cone-beam CT architecture with the exact volumetric reconstruction algorithm [12, 13]. Wang *et. al.* presented a general scheme of multi-source interior tomography which operates multiple (≥ 7) rotating source-detector chains simultaneously [14]. Lately, Cao *et. al.* proposed a multi-source interior CT architecture that employs three stationary X-ray source arrays and three detector operated in the interior tomography mode [15]. In interior tomography, X-ray beams are restricted to travel through an internal region of interest (ROI), and thereby reducing radiation exposure to the surrounding tissues [16, 17]. Moreover, interior tomography enables utilization of smaller X-ray detectors, thus it

allows more source-detector chains in a given gantry space [18]. The multi-source interior CT architectures has the potential to achieve the high temporal resolution required for all-phase cardiac CT imaging [15].

In a multi-source CT, X-ray scattering problem is more complicated than that in a conventional single-source CT. X-ray scattering in a multi-source CT involves both the traditional forward scattering that occurs at the same source-detector chain, and the cross scattering that takes place among different source-detector chains. In a multi-source CT, each X-ray detector receives the forward scattering originated from the X-ray source at the opposite side, and more importantly, the "cross" scattering originated from the other activated X-ray sources at cross angles (hence termed "cross scattering") [19]. The superposition of forward scattering signal and cross scattering signal at the detector will lead to more noise and lower contrast-to-noise ratio (CNR) in the final CT images. Therefore, cross scattering is expected to increase the total amount of scattering to the detectors in multi-source CT schemes, and dedicated cross-scatter correction techniques are needed to improve CT image quality.

The correction methods for forward scattering have been extensively studied for conventional single-source CT [20, 21]. For example, Ning *et. al*. used a beam-stopper-array (BSA) to acquire a set of scout projections and then applied angular interpolation to estimate forward scattering at all view angles, before the regular CT scan [22]. Ren *et. al.* proposed a synchronized-moving-grid (SMOG) system to combine two complementary projections to determine the patient projection and forward scattering at each view angle

[23]. By contrast, only a few correction methods for cross scattering have been reported. The conventional hardware-based scatter suppression techniques (i.e. anti-scatter grid, air gap and bow-tie filter) are insufficient for cross scattering reduction in dual-source CT [19, 24]. The manufacturer for dual-source CT has developed a few dedicated scatter correction techniques, including a scatter-sensor based method and a tabulated model based method [25]. Moreover, Ren *et. al.* have recently applied pre-patient grids to correct both forward scattering and cross scattering in dual-source CT, with the grids placed at two complementary locations to combine the complementary X-ray projections at all view angles [26]. On the other hand, interior tomography tends to suppress X-ray scattering, because X-ray scattering is approximately proportional to the irradiated volume of the subject. Multi-source interior CT architectures have been simulated using conventional single-source CT data [14, 15], yet the effects of cross scattering were not considered in these previous studies. Therefore, our objective of this study is to develop effective correction techniques for cross scattering in multi-source CT.

In this work, we first investigated the impacts of X-ray cross scattering in our previously presented multi-source interior CT architecture [15], and then developed two scatter correction methods to suppress the scattering artifact and improve the CT image quality. The first method modifies the SMOG method for multi-source CT, by replacing the SMOG with an array of stationary BSAs. Compared with the SMOG method, this stationary BSA method can bypass the technical challenges of synchronizing the fast-moving grid with the rapid gantry rotation. The second method directly measures cross scattering in multi-source

CT, by activating / deactivating the X-ray sources under the newly designed source trigger sequences (STS). This new STS method is exceptionally suitable for multi-source CT, and it can enable a fast online measurement of cross scattering during a regular CT scan. Furthermore, both methods allow a considerable radiation dose reduction.

The paper is organized as follows. In section 2, we will introduce the multi-source interior CT system architecture, followed by the descriptions for the Monte Carlo simulation, physical experiments, and the scatter correction methods. In section 3, we will present the results from the simulation and experiments on the scattering effects in the multi-source interior CT architecture, and the results from the two scatter correction methods. In the last section, we will discuss the results and conclude this paper.

3.3 Methods

3.3.1 System overview

A schematic illustration of the multi-source interior CT architecture is shown in Figure 3-1. This architecture utilizes three stationary X-ray source arrays and three rotating flat panel X-ray detectors, which form the three imaging chains. The three identical source arrays are placed outside the rotating gantry and symmetrically around the rotation axis. The total coverage angle of the source arrays would allow data acquisition for a short CT scan (i.e. 180˚ + fan angle). The three detectors are mounted equal angularly (with 120˚ angular interval) on the rotating gantry. Three interior collimators are fixed on the rotation gantry

and opposite to the detectors, to restrict the size of X-ray beams. The size of interior field-of-view (FOV) is determined by the collimator aperture size and the system geometry. During scans, the three source-detector chains can be operated simultaneously. The source arrays produce X-rays by extracting electron beams from an array of cathodes and sending each electron beam to a distinctive focal spot on the same anode target. The cathodes can be based on either hot dispenser cathode emitters (DCE's) [27] or cold field emitters such as carbon nanotubes (CNT) [28]. Electron beams (and hence the corresponding X-ray beams) can be switched on and off electronically by applying the corresponding gate voltages on the cathodes. By programming the gate voltages, a scanning X-ray beam can be generated to image an object from different angles, enabling tomographic imaging without X-ray source motion [29]. The CNT-based X-ray source array technology is very attractive, because the cold CNT cathodes can work at the room temperature and allow compact packaging and faster and more flexible control of X-ray emission [30]. For the CNT X-ray source arrays, the X-ray emission can be controlled by a pre-programmed electrical trigger signal that turns on and off the gate voltages on individual CNT cathodes. The electronic sweeping of the X-ray beams from the X-ray source arrays is synchronized with the rotation of the X-ray detectors. More details about this system configuration can be found in the reference [15].

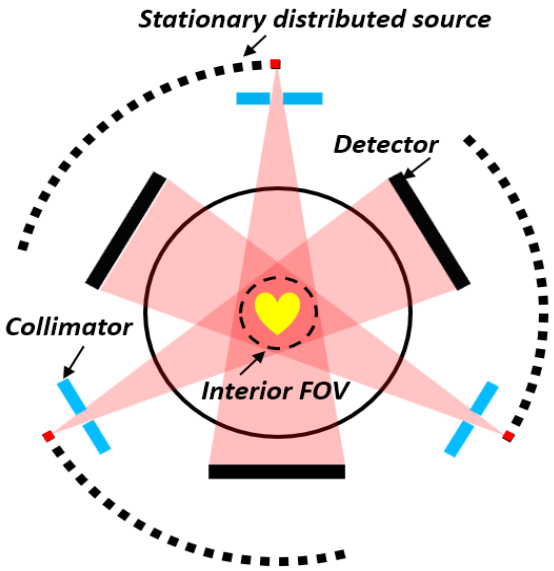

Figure 3-1 A schematic of the stationary X-ray source arrays based multi-source interior CT architecture. This architecture consists of three stationary source arrays and three rotating X-ray detectors. The interior collimators are fixed on the rotating gantry opposite to the detectors.

3.3.2 Monte Carlo simulation

A Monte Carlo simulation of the multi-source interior CT was implemented by using a previously published GPU-based software package [31]. The parameters of imaging geometry and scanning protocols (Table 3-1) were chosen to be similar to those of clinical CT scanners [32]. In the simulation, the X-ray source voltage was 80 kV and the X-ray beams were filtered by 2.3 mm aluminum. The simulated X-ray photon interactions included photoelectric absorption, Compton scattering, and coherent (Rayleigh) scattering.

The imaging object was a modified numerical CATphan® 600 phantom. The standard numerical CATphan® 600 phantom was scaled down (120 mm in diameter) and then placed in the center of a water cylinder (256 mm in diameter). The interior tomography was realized by restricting the cone-beam angle at 13°. The interior FOV at the isocenter was a sphere of 120 mm in diameter. The simulated CT scans were conducted in the single-source global CT mode, single-source interior CT mode, and multi-source interior CT mode.

Table 3-1. Parameters of imaging geometries and scanning protocols.

Source-Isocenter distance (mm)	520
Source-detector distance (mm)	940
Field-of-view at isocenter (mm)	120
Total coverage angle (°)	219
Step angle per projection (°)	1
Source voltage (kV)	80
Total mAs	50

3.3.3 Physical experiments

To experimentally simulate the multi-source interior CT architecture, physical experiments were performed in an in-house developed CT imaging platform (Figure 3-2A). It consists mainly of a laboratory X-ray source (Oxford instrument, Inc.), a flat panel detector (Hamamatsu, Inc.), and several mechanical stages. The source was operated at 80 kV with 2.3 mm aluminum filter. The interior tomography was realized by mounting an aperture

collimator near the X-ray source. The interior FOV at isocenter was also spherical with a diameter of 120 mm. The geometry and parameters of the CT scans are listed in Table 3-1. The CT platform can be configured to simulate the CT data acquisition at the conventional single-source global CT mode, single-source interior CT mode, and multi-source interior CT mode. The details for data acquisition in the multi-source interior CT mode are illustrated in Figure 3-3. First, the detector and the source were placed opposite to each other, and the detector detects the primary X-ray signal and forward scattering signal which are originated from the opposite X-ray source at view β. Then, the source and the detector were re-arranged at two cross angles, and the detector detects the cross scattering signals from the two "cross" sources at the views β+120° and β+240° respectively. This method allows the cross scattering signals to be directly measured by placing the X-ray source at the "cross" angles. The total X-ray scattering signals can be assumed as the addition of the forward scattering and cross scattering signals [20, 21]. Therefore, the total X-ray signal at a detector in the multi-source interior CT mode can be synthesized by the superposition of the primary signals, forward scattering signals, and cross scattering signals.

A customized CT phantom was fabricated for the imaging experiments. The diameter and height of the phantom was 250 mm and 310 mm respectively. To increase the heterogeneity of the phantom structure and materials, the phantom was fabricated with acrylic tubes/blocks, artificial bone, animal ribs, Styrofoam blocks, polyurethane strips, water, glass rods, iodine, corn oil, calcium carbonate, calcium chloride, graphite, aluminum oxide, polyethylene tubes, and duct tape. A picture of the phantom is shown in Figure 3-2B.

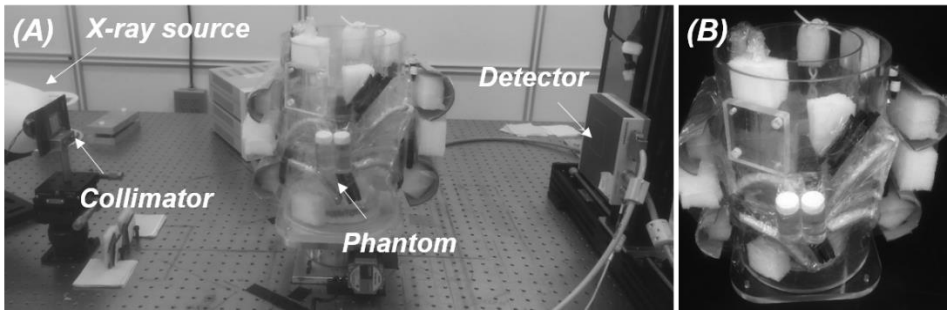

Figure 3-2. (A) Experimental setup of the imaging platform. (B) In-house CT phantom.

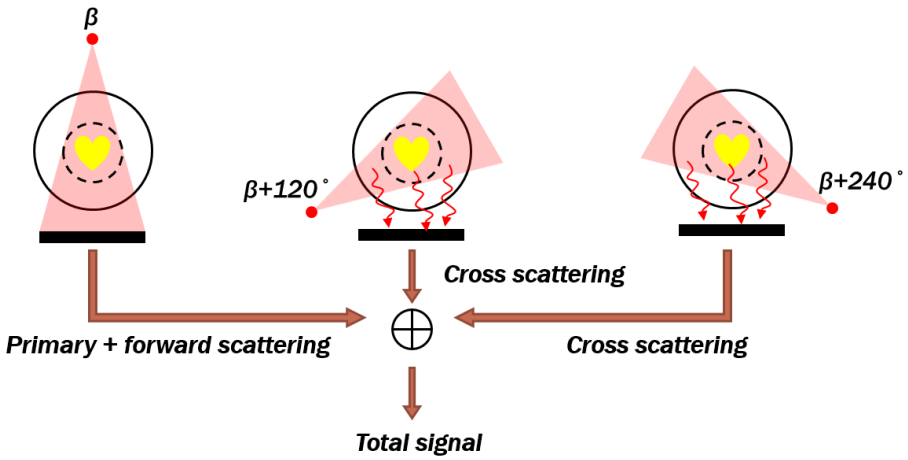

Figure 3-3. Illustration of the experimental synthesis of total X-ray signals in the multi-source interior CT mode.

3.3.4 Scatter correction

3.3.4.1 Beam-stopper-array based scatter correction

The BSA based scatter correction method was inspired by the SMOG based scatter correction method (for single-source cone-beam CT) proposed by Ren *et. al.* [23]. The SMOG was shifted periodically along the longitudinal direction to measure the scattering

signals, by using a rotor crank system that coupled the movement of the SMOG to the rotation of the gantry (Figure 3-4A). This SMOG method can be easily adapted for the stationary source based multi-source CT illustrated in Figure 3-1. We propose to replace the moving-grid with an array of stationary BSAs. These BSAs will be attached in front of all X-ray sources with periodic offset along the longitudinal direction (Figure 3-4B). Ideally, the BSAs could be attached to the exit windows of all X-ray sources in each source array (Figure 3-4C). The geometrical specifications of the BSAs used in this study are shown in Table 3-2. It is assumed that the septa of BSA can fully absorb the incident primary X-rays, and only the scattered X-rays can arrive at the detector pixels under the shadow of the septa (i.e. shadow regions). The scattering signals received by the detector pixels in the open regions were estimated by the cubic spline interpolation [33]. In this way, both the forward scattering signals and the cross scattering signals can be obtained.

Table 3-2. Specification of BSA

Septa length (mm)	9
Septa width (mm)	2
Septa depth (mm)	4
Septa material	Lead
Offset (mm)	2
Interspace (mm)	2

The scattering signals can then be subtracted from the projection data, to calculate the primary X-ray signals at the open regions. The missing primary X-ray signals at the shadow regions can be calculated by using the inter-projection interpolation (IPI) technique described in the reference [34]. An example of using IPI method to recover the primary signals is shown in Figure 3-4D. In this example, to restore the shadow region B1 in the view β2, the open regions R1 and R2 from the two adjacent views β1 and β3 are selected as the inputs. Then, pairs of detector pixels (termed as "reference points") from the open region R1 and R2 are analytically identified for each missing pixel in B1. Finally, the primary X-ray signals at the missing pixels in B1 are calculated as the mean value of the optimal reference points. The optimal reference points were selected by minimizing an energy function with the similarity and smoothness constraints:

$$E = E_{data} + \lambda E_{smooth} \quad (1)$$

where E_{data} is the sum of similarity cost of all reference points at the same scanline, E_{smooth} is the smoothness term, and λ is a weighting factor. Details of the IPI method can be found in the reference [34].

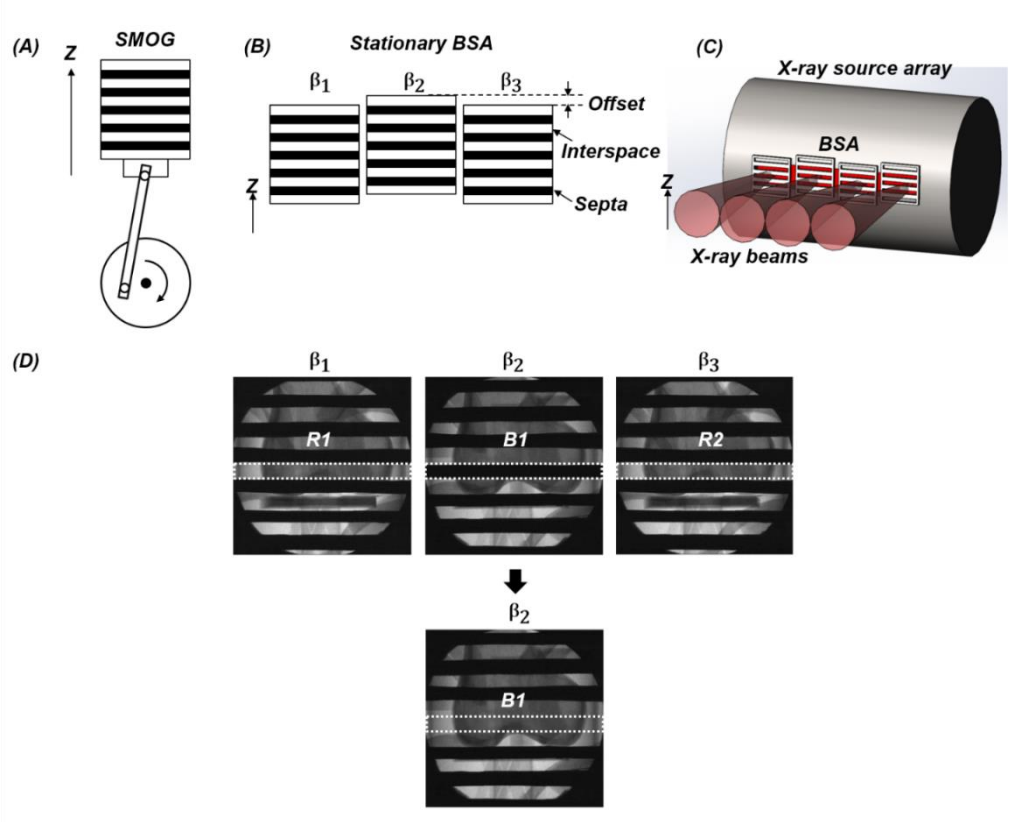

Figure 3-4. (A) The moving-grid mounted on a rotor crank system in the SMOG method. Z-axis indicates the longitudinal direction. (B) Stationary BSA at three neighboring sources in a source array, corresponding to three consecutive views. β2 indicates the central view, and β1 and β3 indicate the two adjacent views. The angular interval was 1°. (C) A 3D rendering of the stationary BSA array with an X-ray source array. (D) An example of recovering the missing primary X-ray signals by using the IPI method. The shadow region B1 in the central view β2 is restored by using the open regions R1 and R2 in the adjacent views β1 and β3.

3.3.4.2 Source trigger sequence based scatter correction

It is well known that the X-ray scattering signals operate primarily at low spatial frequencies [22, 35]. Therefore, scattering signals can be sampled sparsely at only a few views, and then angular interpolation can be used to estimate the scattering signals at the remaining views. In the multi-source interior CT architecture, the X-ray cross scattering signals can be measured directly by switching on only one X-ray source and switching off the other X-ray sources at each sampling view. Therefore, the STS for the multiple sources can be designed to provide an on-the-fly measurement of the cross scattering signals during CT scans. This STS strategy is illustrated in Figure 3-5. Three synchronized source trigger sequences can be designed for the three source arrays S1, S2, and S3 respectively. At the selected views (i.e. sampling views) for which the cross scattering signals will be measured, two X-ray sources were switched off to measure the cross scattering induced by the activated source. For example, to measure the cross scattering signals induced by the source at view β, we can switch off the other two sources (at the source arrays S2 and S3) at views $\beta+120^{\circ}$ and $\beta+240^{\circ}$, and switch on the source (at the source array S1) at view β. The cross scattering signals originated from the source S1 can then be directly measured by the detectors D2 and D3. This sampling scheme for the cross scattering can be repeated for a few selected view angles. The similar STS based sampling were implemented for the source arrays S2 and S3, to measure the cross scattering signals induced by the sources in the source array S2 and S3 respectively. At all the other views, the three source arrays would be activated simultaneously to speed up data acquisition. In this study, seven measurements of cross scattering signals were conducted at an angular interval ($d\beta$) of 10°

for each source array, resulting in 21 measurements of cross scattering signals for the three source arrays. The cross scattering signals at the other views were estimated with cubic spline angular interpolation. Then, the correction for the cross scattering becomes a simple subtraction of the measured projection data by the cross scattering signals. The remaining forward scattering can be corrected by using the existing scatter correction methods for single-source cone-beam CT. In this study, the remaining forward scattering was corrected by using the fast adaptive scatter kernel superposition (FASKS) method [36]. Briefly, the FASKS method employs multiple stationary scatter kernels, which are derived from Monte Carlo simulation with water slabs at various thicknesses. Then, these scatter kernels are adaptively combined to model the scattering signals with a dependence on the local water-equivalent thicknesses of the object. More details of FASKS method can be found in the reference [36].

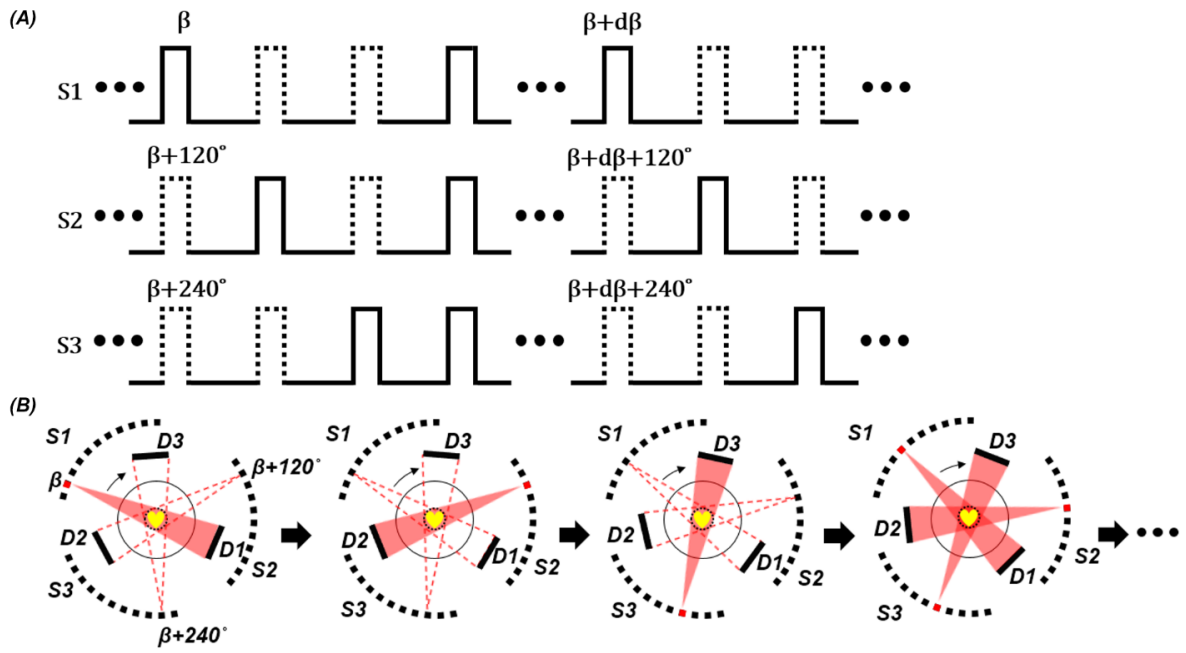

Figure 3-5. (A) Trigger sequences for the source arrays S1, S2 and S3. X-ray sources are only energized at the solid pulses and not at the dotted pulses. (B) Illustration of the X-ray beams sweeping with the source trigger sequences in (A). D1, D2, and D3 indicate the X-ray detectors.

3.3.5 Evaluation method

The forward-scatter-to-primary ratio (FSPR) and the cross-scatter-to-primary ratio (CSPR) were used to quantify the amount of forward scattering and cross scattering respectively. For simulation, the primary signals, forward scattering signals and cross scattering signals were simulated separately to calculate the FSPR and CSPR. For experiments, these signals were directly measured to evaluate the FSPR and CSPR. The primary signals were measured at the single-source fan-beam (3 mm beam thickness) CT mode, since X-ray

scattering can be considered negligible in the fan-beam CT [37]. The forward scattering signals were obtained by subtracting the measured primary signals from the projection data from the corresponding single-source CT mode. The cross scattering signals were measured as shown in Figure 3-3.

For the STS method, the estimation accuracy of cross scattering was evaluated in both the simulation and experiments. First, cross scattering signals were acquired at 720 views equal-angularly spaced around the phantoms in a full circle. Then, 36 evenly spaced measurements of cross scattering (i.e. 10˚ angular interval) were selected as the measurements of the cross scattering signals in the STS method. The cross scattering signals at the remaining views were estimated through cubic spline angular interpolation. The estimated cross scattering signals were compared to the ones measured directly at the same views. The estimation accuracy was quantified using the mean-absolute-percentage-error (MAPE) for each view:

$$MAPE = \frac{1}{Q}\sum_{k=1}^{Q}\left|\frac{M_{k,i} - E_{k,i}}{M_{k,i}}\right| \times 100\% \quad (2)$$

where Q is the number of pixels per view, $M_{k,i}$ is k^{th} pixel of the measured cross scattering at i^{th} view, and $E_{k,i}$ is k^{th} pixel of the estimated cross scattering at i^{th} view.

To assess the effectiveness of the scatter correction methods, image quality was compared before and after the scatter correction. Image reconstruction was carried out using total variation minimization (TVM) based simultaneous algebraic reconstruction technique (SART) algorithm [38]. The simulated X-ray primary signals from the Monte Carlo

simulation were used to reconstruct the "scatter-free" reference images for image quality evaluation. For the physical experiments, the fan-beam (3mm beam thickness) global CT scan was conducted to establish the reference image, because of the negligible X-ray scattering in fan-beam CT [37]. The BSA based method was applied only for the physical experiments, while the STS based method was tried on both the simulated and experimental data. Image quality was quantitatively analyzed in terms of CNR and CT number accuracy. The CNR was calculated as:

$$CNR = \frac{|\mu_1 - \mu_2|}{\sqrt{\sigma_1^2 + \sigma_2^2}} \tag{3}$$

Where μ_1 and μ_2 are the averaged CT numbers of two selected ROIs, σ_1 and σ_2 are standard deviation of these two ROIs respectively. Moreover, CT number accuracy was analyzed using the mean absolute error (MAE):

$$MAE = \frac{1}{N}\sum_{k=1}^{N}(|p_{k,i} - p_{k,r}|) \tag{4}$$

Where $p_{k,i}$ and $p_{k,r}$ are k^{th} pixels from the same ROIs of the multi-source interior CT images and the reference images respectively, and N is the number of pixels in those ROIs. The location of ROIs is shown in Figure 3-6. The sizes of ROIs were 24 mm^2 and 34 mm^2 in simulation and experiments respectively.

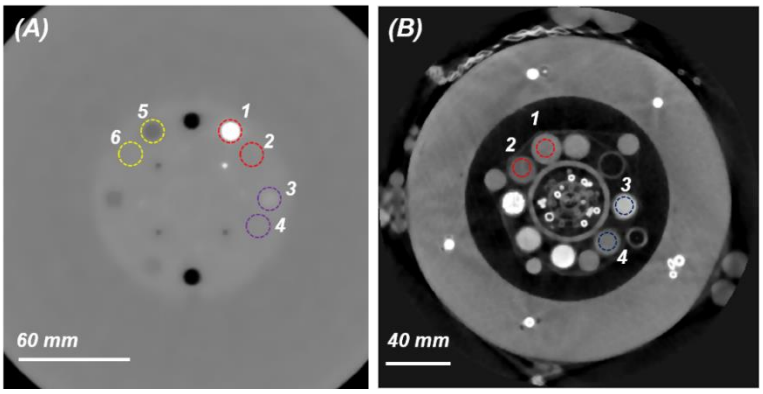

Figure 3-6. The selection of ROIs in the reconstructed images for the analysis of CNR and CT number error. (A) The zoom-in image of the numerical CATphan 600 phantom. (B) The zoom-in image of the in-house physical phantom.

3.4 Experimental results

Figure 3-7 shows the FSPR and CSPR along the detector pixels at the central detector row, for the projections at View 0˚. For simulation, the magnitude of CSPR was up to 4.8, while FSPR was relatively smaller (< 1.1). For physical experiments, CSPR and FSPR were up to 3.57 and 1.08 respectively. Notice that the magnitude of CSPR was significantly higher than that of FSPR in both the simulation and experiments. More detailed discussion about this phenomenon is presented in Sec. 4.

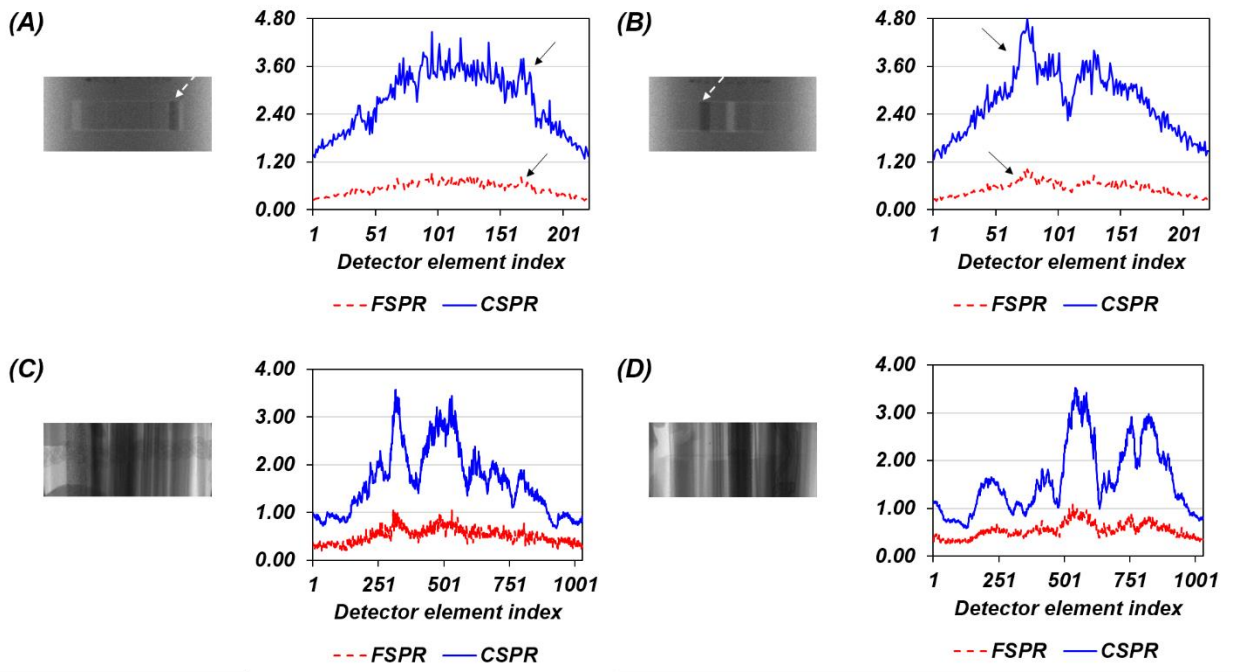

Figure 3-7. Examples of the profiles of FSPR and CSPR. (A) – (B) the simulated FSPR and CSPR at views 0˚ and 90° respectively. Insets: the simulated (zoom-in) projection of CATphan phantom. (C) – (D) the experimentally measured FSPR and CSPR at views 0˚ and 90° respectively. Inset: the (zoom-in) projection of the in-house phantom. White dashed arrows indicate the locations of X-ray projections through Teflon insert region (i.e. ROI1 in Figure 3-6A). Black solid arrows indicate the locations of local FSPR and CSPR at the X-ray projections through Teflon insert region.

Figure 3-8 shows the estimation accuracy of cross scattering in the STS based method. In both simulation and physical experiments, the interpolation error was small. For simulation, the MAPE was less than 3.0% throughout all views. For physical experiments, the MAPE was less than 2.4%. The non-uniform angular distribution of MAPE in the cross scattering estimation could be attributed to the inhomogeneity of phantom structure and

materials. We can conclude that, although the angular sampling was carried out with a relatively large interval in the STS method, the estimation accuracy of the cross scattering was high.

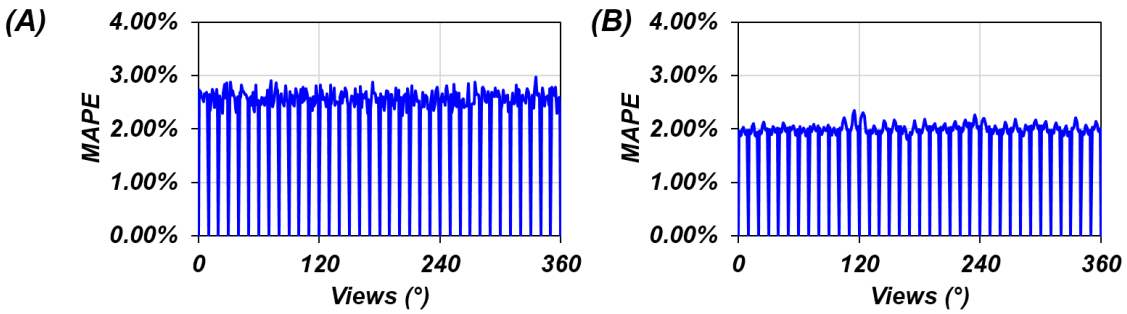

Figure 3-8. Mean-absolute-percentage-error (MAPE) of the estimated cross scattering signals at different views for the STS method. (A) Monte Carlo simulation. (B) Physical experiment.

Figure 3-9 shows the reconstruction results from the Monte Carlo simulation data. Figure 3-10 plots the line profiles (marked by L1 and L2 in Figure 3-9A) in the reconstructed images. It can be observed that, compared to the "scatter-free" reference image (Figure 3-9B), forward scattering caused a downward deviation of image pixel values in the single-source interior CT mode (Figure 3-9C), and cross scattering induced obvious shading artifact in the center of the image in the multi-source interior CT mode (Figure 3-9D). It is obvious that X-ray scattering deviated CT numbers from the reference image, which is especially true for cross scattering.

The image quality is largely improved after the scatter correction (Figure 3-9E-F). With the STS method, the line profiles from the multi-source interior CT mode were partially

restored, and matched well with those from the single-source interior CT mode. After combining the STS based cross-scatter correction method with the FASKS based forward-scatter correction method, the line profiles from the multi-source interior CT mode became close to the ones from the reference image.

The quantitative evaluation of CNR and CT number deviation of the six selected ROIs (marked by numbers 1-6 in Figure 3-6A) is shown in Table 3-3. Without scatter correction, multi-source interior CT mode yielded a significant reduction of CNR (up to 68.5%) and the largest CT number error (up to 1122 HU). With the STS method, both CNR and CT number accuracy of the multi-source interior CT mode were partially recovered to be similar to those of the single-source interior CT mode. With the combined STS and FASKS methods, CNR was further improved and CT number error was largely suppressed (up to 37 HU).

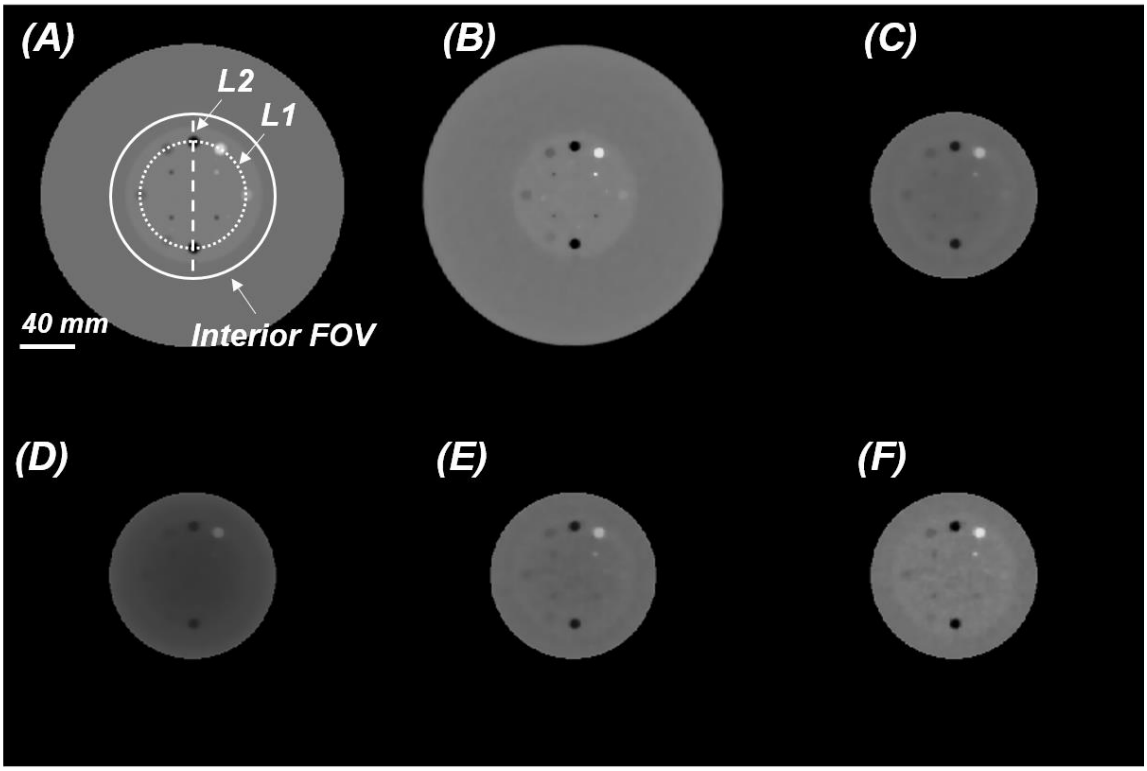

Figure 3-9. (A) Selection of line profiles. L1 and L2: the selected line profiles are shown in the Figure 3-10. (B) "Scatter-free" reference image. (C) Single source interior CT w/o scatter correction. (D) Multi-source interior CT w/o scatter correction. (E) Multi-source interior CT with cross-scatter correction, using STS method. (F) Multi-source interior CT with forward/cross-scatter correction, using STS method and FASKS method. Display window [-1000 1200] HU.

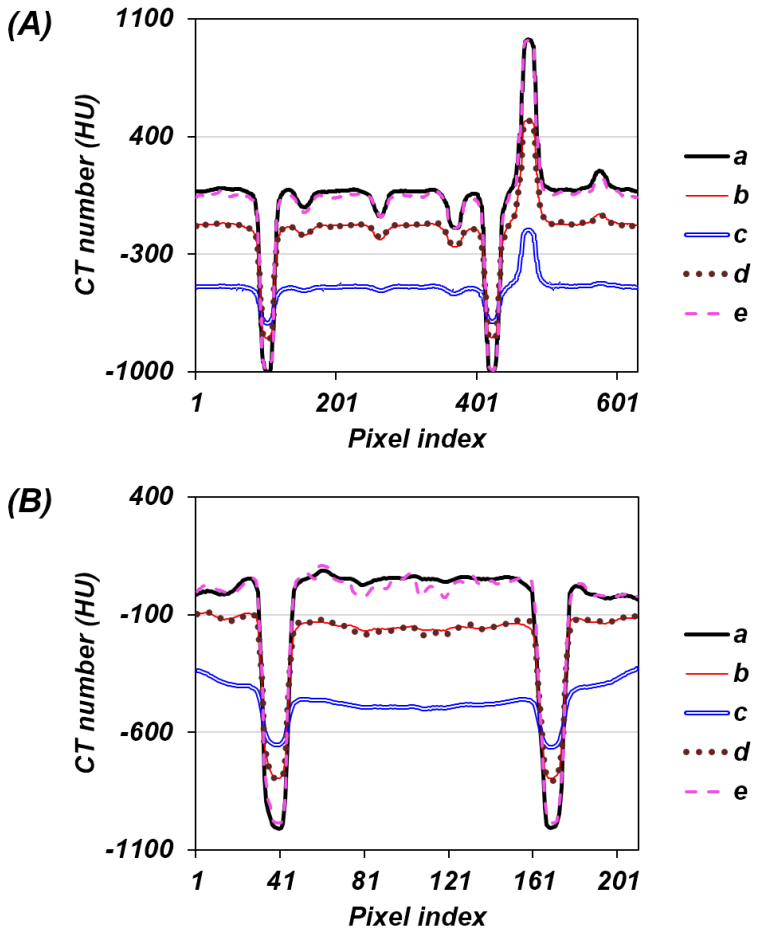

Figure 3-10. Line profiles of L1 (A) and L2 (B) at Figure 3-9A: a – "Scatter-free" reference; b – Single-source interior CT w/o scatter correction; c – Multi-source interior CT w/o scatter correction; d – Multi-source interior CT with cross-scatter correction, using STS method; e – Multi-source interior CT with forward/cross-scatter correction, using STS method and FASKS method.

Table 3-3. Contrast-to-noise ratio (CNR) and mean absolute error (MAE) of ROIs 1-6 in the simulation. a – "Scatter-free" reference; b – Single-source interior CT w/o scatter correction; c – Multi-source interior CT w/o scatter correction; d – Multi-source interior CT with cross-scatter correction, using STS method; e – Multi-source interior CT with forward/cross-scatter correction, using STS method and FASKS method.

		a	b	c	d	e
CNR	ROI 1 vs ROI 2	40.0	36.3	30.0	34.7	37.2
	ROI 3 vs ROI 4	10.8	7.9	3.4	7.6	8.4
	ROI 5 vs ROI 6	15.1	12.7	5.3	12.3	13.4
MAE (HU)	ROI 1	-	470	1122	475	37
	ROI 2	-	206	578	212	33
	ROI 3	-	245	653	259	35
	ROI 4	-	210	580	215	31
	ROI 5	-	112	405	118	34
	ROI 6	-	208	583	213	32

The reconstruction results from the physical phantom experiments are shown in Figure 3-11. By visual inspection, X-ray scattering caused obvious negative effects on the image quality. Compared with the single-source interior CT mode, cross scattering in the multi-source interior CT mode induced the shading artifact across the reconstructed image, and caused significant reduction of image contrast and CT number accuracy. Similar to the results from the simulation, with STS method, the image from the multi-source interior CT mode can be restored to be similar to that from the single-source interior CT mode.

Figure 3-12 shows the selected line profiles (marked by L3 and L4 in Figure 3-11A) from the reconstructed phantom images. Before scatter correction, X-ray scattering greatly deviated the CT numbers from the reference, and suppressed the image contrast. After applying the STS method, the line profiles from multi-source interior CT mode became well matched with those from the single-source interior CT mode. After using FASKS method, the discrepancy between the line profiles from the reference image and those from the multi-source interior CT mode was largely reduced. The BSA-based method addressed forward scattering and cross scattering simultaneously, therefore it can largely improve the line profiles from the multi-source interior CT mode to be well matched with the ones from the reference image.

Table 3-4 shows the quantitative evaluation of CNR and CT number error of four selected ROIs (marked by numbers 1-4 in Figure 3-6B). Before scatter correction, CNR was degraded by up to 50.7% and CT number deviation was up to 929 HU in multi-source interior CT mode. Again, the STS method improved both CNR and CT number accuracy to the same level of single-source interior CT mode. Using both STS and FASKS methods, CNR was further improved and CT number error was significantly reduced (up to 35 HU). In addition, the BSA-based method also further improved CNR at the selected ROIs, and reduced CT number error (up to 37 HU). In the physical experiments, STS method also allowed the multi-source interior CT mode to yield comparable image quality to that of the single-source interior CT mode. Moreover, BSA-based method greatly corrected the negative effects from both forward scattering and cross scattering simultaneously.

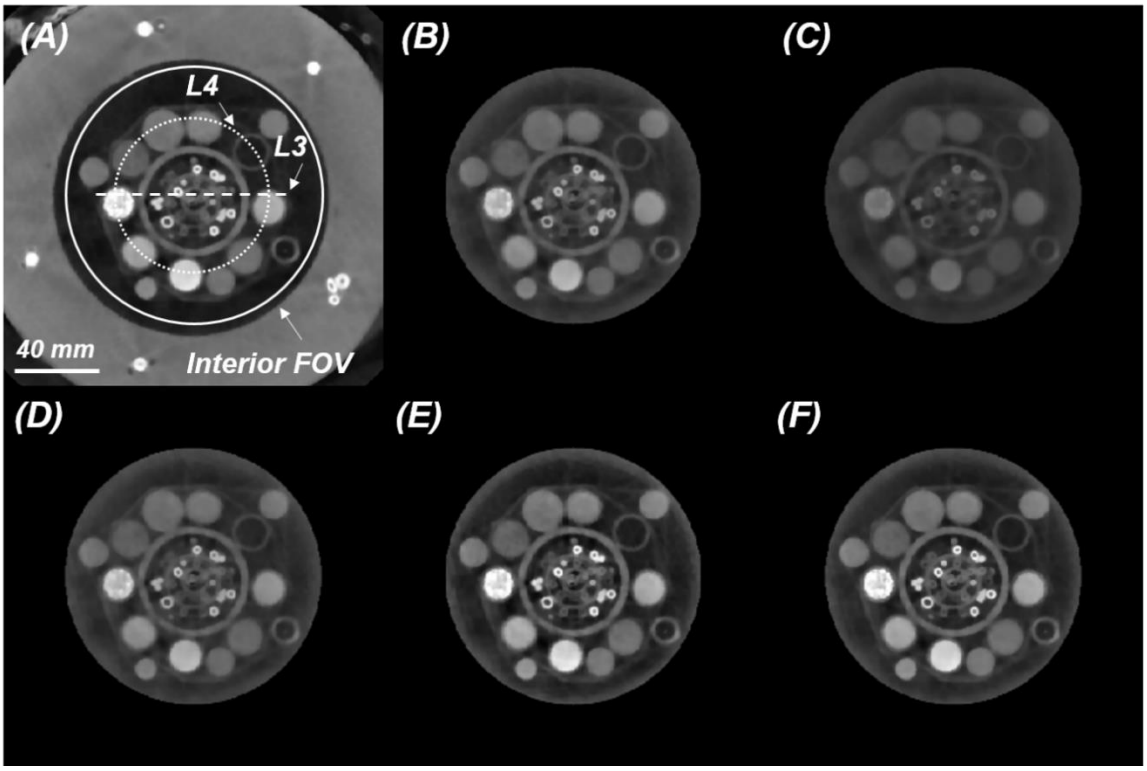

Figure 3-11. (A) "Scatter-free" reference image (zoom-in to the interior FOV) and the selection of line profiles. L3 and L4: the selected line profiles are shown in Figure 3-12 (B) Single-source interior CT w/o scatter correction. (C) Multi-source interior CT w/o scatter correction. (D) Multi-source interior CT with cross-scatter correction, using the STS method. (E) Multi-source interior CT with forward/cross-scatter correction, using STS method and FASKS methods. (F) Multi-source interior CT with forward/cross-scatter correction, using the stationary BSA based method. Display window [-1000 1800] HU.

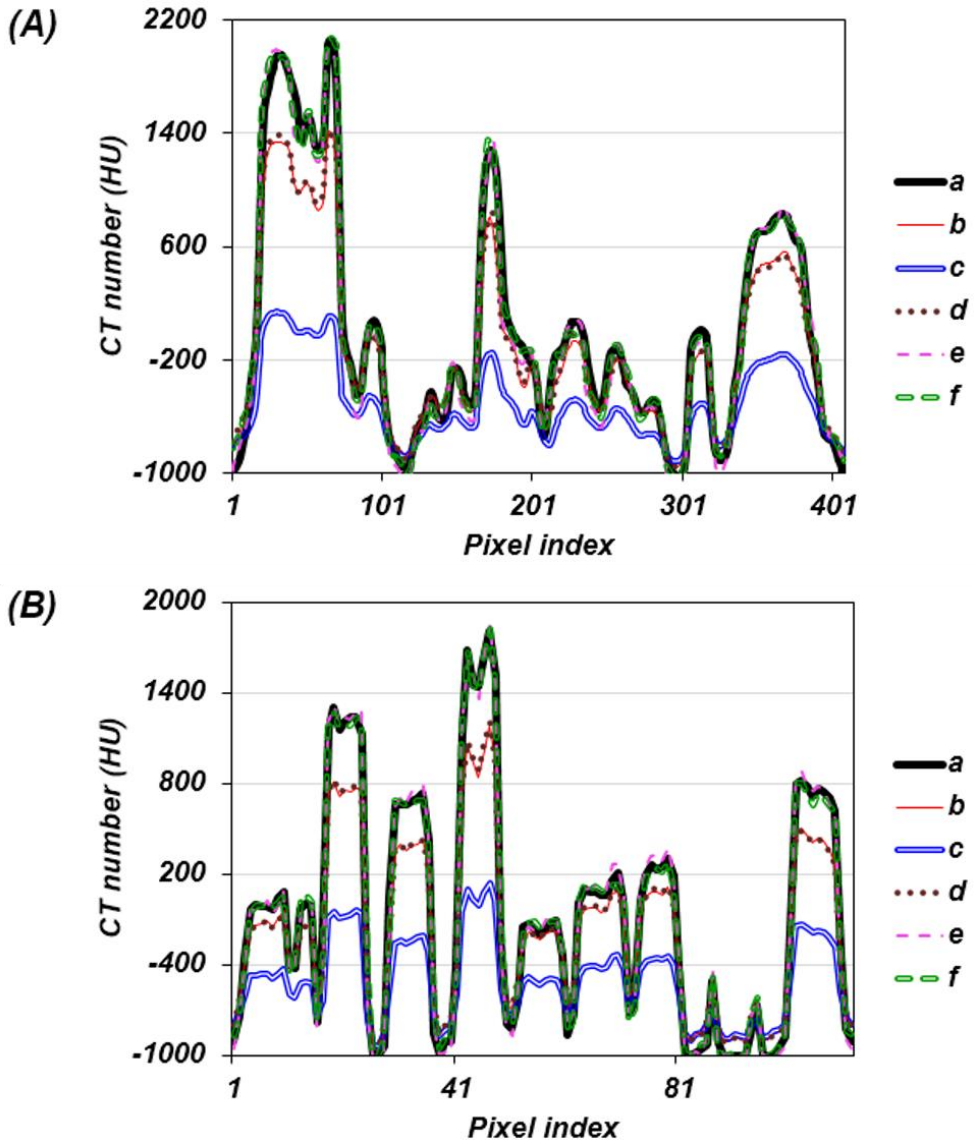

Figure 3-12. Line profiles of L3 (A) and L4 (B) at Figure 3-11A: a – "Scatter-free" reference; b – Single-source interior CT w/o scatter correction; c – Multi-source interior CT w/o scatter correction; d – Multi-source interior CT with cross-scatter correction, using STS method; e – Multi-source interior CT with forward/cross-scatter correction, using both STS method and FASKS methods; f – Multi-source interior CT with forward/cross scatter correction, using BSA based scatter correction.

Table 3-4. Contrast-to-noise ratio (CNR) and mean absolute error (MAE) of ROIs 1-4 in the experiments. a – "Scatter-free" reference; b – Single-source interior CT w/o scatter correction; c – Multi-source interior CT w/o scatter correction; d – Multi-source interior CT with cross-scatter correction, using STS method; e – Multi-source interior CT with forward/cross-scatter correction, using both STS method and FASKS methods; f – Multi-source interior CT with forward/cross scatter correction, using BSA based scatter correction.

		a	b	c	d	e	f
CNR	ROI1 vs ROI2	7.1	5.0	3.5	4.9	5.2	5.3
	ROI3 vs ROI4	40.6	36.2	32.5	35.3	38.2	37.3
MAE (HU)	ROI1	-	100	478	117	32	34
	ROI2	-	76	383	82	26	25
	ROI3	-	309	929	316	35	37
	ROI4	-	82	445	90	27	31

3.5 Discussion and conclusion

In this study, we conducted a Monte Carlo simulation to simulate the X-ray cross scattering in a multi-source interior CT architecture, and constructed a bench-top imaging platform to experimentally quantify the cross scattering signals using a customized phantom. The cross scattering signals were superposed onto the projection images (which include forward scattering signals) to synthesize the expected X-ray projections from the multi-source CT architecture. The underlying assumption is that the cross scattering signals are additive. The image quality was evaluated with and without the influences of the X-ray cross

scattering, to highlight the effects of X-ray cross scattering in multi-source CT schemes. Two correction methods for cross scattering (i.e. STS and BSA based methods) were developed and evaluated. The BSA based method significantly improved the image quality from multi-source interior CT by correcting both forward scattering and cross scattering simultaneously, while the STS method enabled multi-source interior CT to yield comparable image quality to that of single-source interior CT by correcting the cross scattering.

X-ray scattering in multi-source CT architectures depends on the number of source-detector chains, the imaging geometry, and the characteristics of the subject (i.e. size, shape, etc.). In this work, we observed that the multi-source interior CT architecture yielded high magnitudes of FSPR and CSPR. This phenomenon can be attributed to the following reasons. First, we utilized a tube voltage of 80kV in both the simulations and the experiments. At this relatively low energy X-rays, the transmittance of primary X-ray signals through the phantoms was low and thus the SPR became relatively high. This is particularly true for the Teflon insert region (i.e. ROI1 in the numerical phantom) and iodine insert region (i.e. ROI3 in the physical phantom) in the simulations and experiments respectively. Second, we utilized cone-beam imaging geometry with a much wider longitudinal collimation (120 mm z coverage) than that of the typical dual-source CT (20 mm z coverage in [19, 24]). Despite a relatively small interior FOV in the transverse plane, the larger z coverage still yielded a considerable volume of the phantoms under X-ray irradiation. In fact, each cone beam irradiated a volume of 2,882 cm^3 in the phantoms. In

comparison, because of 20 mm z coverage in dual-source CT [19], the global X-ray beam irradiated a much smaller volume of 1,512 cm^3. Third, the three simultaneously operated X-ray sources increased the occurrence of cross scattering at the detectors. For each detector, the other two X-ray sources at the cross angles can cause a considerable amount of cross scattering. Forth, the 120 deg cross angle in the multi-source CT caused more scattering than the 90 deg cross angle in the dual-source CT. It is known that the differential cross section of Compton scatter is angularly dependent [39], and it is smaller at 90 deg but larger at 120 deg at the diagnostic X-ray energy range. Finally, the simulations and experiments were performed without ASGs and thus more scattered photons can be detected. Interestingly, even with ASGs, the cross scattering in a dual-source CT can still become comparable to or higher than the forward scattering in magnitude [19, 24].

Although we lack a proper ASG in physical experiments, an additional Monte Carlo simulation was conducted to evaluate the effects of a standard ASG in multi-source interior CT. The configuration of ASG is adapted from the reference [19]. The blades of the ASG are thin and highly absorbing tungsten blades which were oriented in parallel to the primary ray paths. The thickness and the height of each blade are 80 μm and 35 mm respectively. The line profiles of FSPR and CSPR are plotted in the figure below:

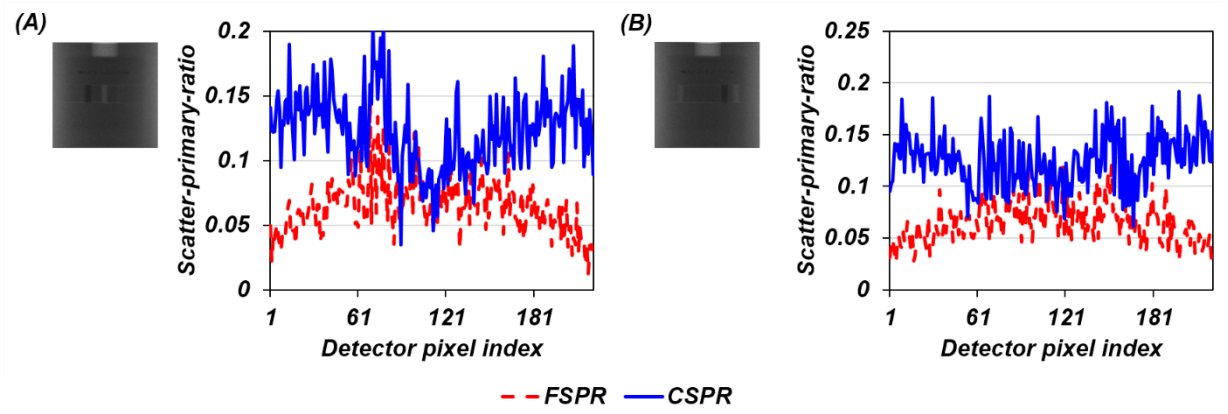

Figure 3-13. The profiles of FSPR and CSPR at the central detector row, respectively from (A) view 180° and (B) view 120°. Insets: the X-ray projections of the modified CATphan 600 phantom.

Compared with the simulation results without ASG, the utilization of ASG significantly reduced the FSPR and CSPR and thus the scatter artifact shall be ameliorated. However, the absolute magnitudes of total scatter-primary-ratio (< 0.4) is still comparable to that of the standard dual-source CT [19, 24]. Moreover, the magnitudes of scatter-primary-ratio is typically proportional to the object size, when the imaging geometry and the scanning protocols are fixed. When the imaged object has larger size (e.g. human torso), higher scatter-primary-ratio could be expected. In a word, the standard ASG is not sufficient for X-ray scatter suppression in multi-source interior CT, and the dedicated X-ray scatter correction methods are desired.

It has been demonstrated that high magnitude of SPR will cause high magnitude of HU error [20, 40]. For instance, when the SPR exceeded 1.2, the reconstructed attenuation coefficient of water deviated from its expected value by over 30% (corresponding to over

300 HU error) [40]. In the same way, the relatively higher SPR through the highly attenuating materials (e.g. the Teflon insert in Figure 3-7A) consequently caused much larger CT number error than other less attenuating materials, as shown in Table 3-3 and Table 3-4. Because of the high magnitudes of FSPR and CSPR in the multi-source CT architecture, cross scattering and forward scattering are important problems for multi-source CT and dedicated scatter correction methods are necessary to improve image quality.

The BSA based method was applied to our multi-source interior CT via imaging experiments in our bench-top imaging platform. By affixing stationary BSA array to the stationary source arrays in our multi-source interior CT architecture, the BSA based method enables an on-the-fly scatter correction with the minimal system modification. Additionally, this method can provide a significant radiation dose reduction (up to 50%), which is at the expense of blocking a part of primary X-ray signals at each view. The percent dose reduction depends on the ratio between the width of septa and interspace. The dose reduction leads to higher noise in the reconstructed CT images. To suppress the image noise, one could employ the TVM based or statistical model based CT reconstruction algorithms [41, 42]. Some effective filtering strategies [25, 43] could also be utilized. In the BSA-based method, the missing primary signals were recovered by the IPI method at the expense of reducing azimuthal resolution [34]. The missing primary signals could be recovered with other existing techniques [44, 45]. In the open region, the forward scattering and cross scattering signals were estimated by cubic spine interpolation. Overall, the BSA-

based method can largely correct the negative effects from both the forward scattering and cross scattering simultaneously.

For the BSA based method, the effects of penumbra from finite focal spot size were not investigated. The BSA method was applied in the experiments only, in which the focal spot size of the X-ray source was very small (16 μm diameter). Thus, the penumbra effects were negligible. However, the penumbra effects should be considered in clinical practices because the focal spot size of a clinical X-ray source is much larger. The signals in the penumbra around the edge of septa shadow come from both scattering and primary photons. If these signals in the penumbra were treated as pure scattering signals, it would cause the corruption of CT numbers in the reconstructed images. To correct the penumbra effects of the septa, it was suggested that the X-ray signals in a central region of the septa shadow can be treated as scattering signals [37]. Then, the primary signals in the penumbra regions and open regions can be retrieved after scatter corrections, to obtain the full scatter-corrected projection images [33]. The exact penumbra effects and their corrections in the multi-source interior CT architecture warrant a future investigation.

The STS based method was carried out in both numerical simulations and physical experiments. The STS method enables simultaneous CT data acquisition and cross-scatter correction within single CT scan. Moreover, this method can also reduce radiation dose, despite the loss of a few projection images at the selected views. Additionally, the STS method can be readily applied in many other multi-source CT schemes. In both our numerical simulations and physical experiments, the STS method enabled multi-source

interior CT mode to yield comparable image quality to that of single-source interior CT mode. This is because STS method is dedicated for cross-scatter correction and does not address the effects of forward scattering. The remaining artifact induced by forward scattering can be further reduced by the FASKS method [36] or other existing methods for conventional single-source cone-beam CT.

In conclusion, we analyzed the X-ray scattering in a stationary source based multi-source interior CT in both simulation and experiments, and investigated the corresponding negative impacts on image quality. We observed a significant degradation in CNR and CT number accuracy, due to forward and cross scattering from simultaneously operated multiple imaging chains. We then proposed two scatter correction methods, and found the methods can greatly suppress the scattering artifact and improve the image quality. The proposed scatter correction methods could find use in multi-source interior CT for dynamic CT imaging with high temporal resolution.

References

[1] G. N. Hounsfield, "Computerized transverse axial scanning (tomography). 1. Description of system," *Br J Radiol,* vol. 46, pp. 1016-1022, 1973.

[2] Z. Sun, G. H. Choo, and K. H. Ng, "Coronary CT angiography: current status and continuing challenges," *The British Journal of Radiology,* vol. 85, pp. 495-510, 2012.

[3] M. Mahesh and D. D. Cody, "Physics of Cardiac Imaging with Multiple-Row Detector CT," *RadioGraphics,* vol. 27, pp. 1495-1509, 2007.

[4] T. G. Flohr, C. N. De Cecco, B. Schmidt, R. Wang, U. J. Schoepf, and F. G. Meinel, "Computed Tomographic Assessment of Coronary Artery Disease: State-

of-the-Art Imaging Techniques," *Radiologic Clinics of North America,* vol. 53, pp. 271-285, 3// 2015.
[5] W. A. Kalender, "X-ray computed tomography," *Phys Med Biol,* vol. 51, pp. R29-43, Jul 7 2006.
[6] P. Schardt, J. Deuringer, J. r. Freudenberger, E. Hell, W. Knüpfer, D. Mattern, *et al.*, "New x-ray tube performance in computed tomography by introducing the rotating envelope tube technology," *Medical Physics,* vol. 31, p. 2699, 2004.
[7] W. A. Kalender, "CT: the unexpected evolution of an imaging modality," *European Radiology,* vol. 15, pp. D21-D24, Nov 2005.
[8] E. L. Ritman, J. H. Kinsey, R. A. Robb, B. K. Gilbert, L. D. Harris, and E. H. Wood, "3-DIMENSIONAL IMAGING OF HEART, LUNGS, AND CIRCULATION," *Science,* vol. 210, pp. 273-280, 1980.
[9] T. G. Flohr, C. H. McCollough, H. Bruder, M. Petersilka, K. Gruber, C. Suss, *et al.*, "First performance evaluation of a dual-source CT (DSCT) system," *European Radiology,* vol. 16, pp. 256-268, Feb 2006.
[10] B. Krauss, B. Schmidt, and T. G. Flohr, "Dual source CT," in *Dual energy CT in clinical practice*, ed: Springer, 2011, pp. 11-20.
[11] Y. Liu, H. Liu, Y. Wang, and G. Wang, "Half-scan cone-beam CT fluoroscopy with multiple x-ray sources," *Medical physics,* vol. 28, pp. 1466-1471, 2001.
[12] J. Zhao, Y. Jin, Y. Lu, and G. Wang, "A Filtered Backprojection Algorithm for Triple-Source Helical Cone-Beam CT," *IEEE transactions on medical imaging,* vol. 28, pp. 384-393, 2009.
[13] Y. Lu, J. Zhao, and G. Wang, "Exact image reconstruction with triple-source saddle-curve cone-beam scanning," *Physics in medicine and biology,* vol. 54, pp. 2971-2991, 2009.
[14] G. Wang, H. Yu, and Y. Ye, "A scheme for multisource interior tomography," *Medical Physics,* vol. 36, pp. 3575-3581, 2009.
[15] G. Cao, B. Liu, H. Gong, H. Yu, and G. Wang, "A stationary-sources and rotating-detectors computed tomography architecture for higher temporal resolution and lower radiation dose," *Access, IEEE,* vol. 2, pp. 1263-1271, 2014.
[16] D. Bharkhada, H. Yu, R. Dixon, Y. Wei, J. J. Carr, J. D. Bourland, *et al.*, "Demonstration of Dose and Scatter Reductions for Interior Computed Tomography," *Journal of computer assisted tomography,* vol. 33, p. 967, 2009.
[17] H. Gong, R. Liu, H. Yu, J. Lu, O. Zhou, L. Kan, *et al.*, "Interior tomographic imaging of mouse heart in a carbon nanotube micro-CT," *Journal of X-Ray Science and Technology,* vol. 25, 2016.
[18] G. Wang and H. Y. Yu, "The meaning of interior tomography," *Physics in Medicine and Biology,* vol. 58, pp. R161-R186, Aug 21 2013.
[19] K. J. Engel, C. Herrmann, and G. Zeitler, "X-ray scattering in single- and dual-source CT," *Medical Physics,* vol. 35, pp. 318-332, 2008.
[20] E.-P. Rührnschopf and K. Klingenbeck, "A general framework and review of scatter correction methods in x-ray cone-beam computerized tomography. Part 1: Scatter compensation approaches," *Medical Physics,* vol. 38, pp. 4296-4311, 2011.

[21] E.-P. Rührnschopf and and K. Klingenbeck, "A general framework and review of scatter correction methods in cone beam CT. Part 2: Scatter estimation approaches," *Medical Physics,* vol. 38, pp. 5186-5199, 2011.
[22] R. Ning, X. Tang, and D. Conover, "X-ray scatter correction algorithm for cone beam CT imaging," *Medical Physics,* vol. 31, pp. 1195-1202, 2004.
[23] L. Ren, F.-F. Yin, I. J. Chetty, D. A. Jaffray, and J.-Y. Jin, "Feasibility study of a synchronized-moving-grid (SMOG) system to improve image quality in cone-beam computed tomography (CBCT)," *Medical Physics,* vol. 39, pp. 5099-5110, 2012.
[24] K. Yiannis and A. K. Willi, "Intensity distribution and impact of scatter for dual-source CT," *Physics in Medicine and Biology,* vol. 52, p. 6969, 2007.
[25] M. Petersilka, K. Stierstorfer, H. Bruder, and T. Flohr, "Strategies for scatter correction in dual source CT," *Medical Physics,* vol. 37, pp. 5971-5992, 2010.
[26] L. Ren, Y. Chen, Y. Zhang, W. Giles, J. Jin, and F. F. Yin, "Scatter Reduction and Correction for Dual-Source Cone-Beam CT Using Prepatient Grids," *Technol Cancer Res Treat,* May 24 2015.
[27] K. Frutschy, B. Neculaes, L. Inzinna, A. Caiafa, J. Reynolds, Y. Zou, *et al.*, "High power distributed x-ray source," 2010, p. 76221H.
[28] F. Sprenger, X. Calderon, E. Gidcumb, J. Lu, X. Qian, D. Spronk, *et al.*, "Stationary digital breast tomosynthesis with distributed field emission X-ray tube," *Proc SPIE Int Soc Opt Eng,* vol. 7961, Mar 3 2011.
[29] X. Qian, A. Tucker, E. Gidcumb, J. Shan, G. Yang, X. Calderon-Colon, *et al.*, "High resolution stationary digital breast tomosynthesis using distributed carbon nanotube x-ray source array," *Medical Physics,* vol. 39, pp. 2090-2099, Apr 2012.
[30] J. Zhang, G. Yang, Y. Z. Lee, S. Chang, J. P. Lu, and O. Zhou, "Multiplexing radiography using a carbon nanotube based x-ray source," *Appl. Phys. Lett.,* vol. 89, p. 064106, 2006.
[31] X. Jia, H. Yan, L. Cerviño, M. Folkerts, and S. B. Jiang, "A GPU tool for efficient, accurate, and realistic simulation of cone beam CT projections," *Medical physics,* vol. 39, pp. 7368-7378, 2012.
[32] O. J. O'Connor, M. Vandeleur, A. M. McGarrigle, N. Moore, S. R. McWilliams, S. E. McSweeney, *et al.*, "Development of Low-Dose Protocols for Thin-Section CT Assessment of Cystic Fibrosis in Pediatric Patients," *Radiology,* vol. 257, pp. 820-829, 2010.
[33] J.-Y. Jin, L. Ren, Q. Liu, J. Kim, N. Wen, H. Guan, *et al.*, "Combining scatter reduction and correction to improve image quality in cone-beam computed tomography (CBCT)," *Medical Physics,* vol. 37, pp. 5634-5644, 2010.
[34] H. Zhang, F. Kong, L. Ren, and J.-Y. Jin, "An Inter-Projection Interpolation (IPI) Approach with Geometric Model Restriction to Reduce Image Dose in Cone Beam CT (CBCT)," in *Computational Modeling of Objects Presented in Images. Fundamentals, Methods, and Applications: 4th International Conference, CompIMAGE 2014, Pittsburgh, PA, USA, September 3-5, 2014,* Y. J. Zhang and J.

M. R. S. Tavares, Eds., ed Cham: Springer International Publishing, 2014, pp. 12-23.
[35] G. J. Bootsma, F. Verhaegen, and D. A. Jaffray, "Spatial frequency spectrum of the x-ray scatter distribution in CBCT projections," *Medical physics,* vol. 40, p. 111901, 2013.
[36] M. Sun and J. M. Star-Lack, "Improved scatter correction using adaptive scatter kernel superposition," *Physics in Medicine and Biology,* vol. 55, p. 6695, 2010.
[37] T. Niu and L. Zhu, "Scatter correction for full-fan volumetric CT using a stationary beam blocker in a single full scan," *Medical Physics,* vol. 38, pp. 6027-6038, 2011.
[38] H. Yu and G. Wang, "Compressed sensing based interior tomography," *Physics in medicine and biology,* vol. 54, p. 2791, 2009.
[39] J. H. Hubbell, W. J. Veigele, E. A. Briggs, R. T. Brown, D. T. Cromer, and R. J. Howerton, "Atomic form factors, incoherent scattering functions, and photon scattering cross sections," *Journal of Physical and Chemical Reference Data,* vol. 4, pp. 471-538, 1975.
[40] J. H. Siewerdsen and D. A. Jaffray, "Cone-beam computed tomography with a flat-panel imager: Magnitude and effects of x-ray scatter," *Medical Physics,* vol. 28, pp. 220-231, 2001.
[41] M. Katsura, I. Matsuda, M. Akahane, J. Sato, H. Akai, K. Yasaka, *et al.*, "Model-based iterative reconstruction technique for radiation dose reduction in chest CT: comparison with the adaptive statistical iterative reconstruction technique," *European Radiology,* vol. 22, pp. 1613-1623, 2012.
[42] H. Lee, L. Xing, R. Lee, and B. P. Fahimian, "Scatter correction in cone-beam CT via a half beam blocker technique allowing simultaneous acquisition of scatter and image informationa)," *Medical physics,* vol. 39, pp. 2386-2395, 2012.
[43] L. Zhu, J. Wang, and L. Xing, "Noise suppression in scatter correction for cone-beam CT," *Medical Physics,* vol. 36, pp. 741-752, 2009.
[44] D. J. Heeger and J. R. Bergen, "Pyramid-based texture analysis/synthesis," presented at the Proceedings of the 22nd annual conference on Computer graphics and interactive techniques, 1995.
[45] M. Bertalmio, G. Sapiro, V. Caselles, and C. Ballester, "Image inpainting," presented at the Proceedings of the 27th annual conference on Computer graphics and interactive techniques, 2000.

Chapter 4 Physics model based scatter correction in multi-source interior computed tomography

Hao Gong[1], Bin Li[2], Xun Jia[2], Guohua Cao[1*]

[1]Department of Biomedical Engineering and Mechanics, Virginia Polytechnic Institute and State University, Blacksburg, VA, 24061, USA

[2]Department of Radiation Oncology, University of Texas Southwestern Medical Center, Dallas, TX, 75390, USA

Publication information – The major contents of this chapter were submitted to ***IEEE Transaction on Medical Imaging*** on 01-24-2017.

4.1 Abstract

The multi-source interior computed tomography (CT) schemes have demonstrated great potentials to provide an ultra-fast and organ-oriented dynamic imaging at low radiation dose. The X-ray cross scattering originated from multiple simultaneously activated X-ray sources superposes onto the forward scattering and then induces worse image artifacts. Previously, we investigated the overall impacts of the X-ray scattering in a recently proposed multi-source interior CT architecture, and proposed two measurement-based scatter correction approaches (H. Gong, et. al., "X-ray scatter correction for multi-source interior computed tomography", Med Phys, 44: 71–83. 2017, doi:10.1002/mp.12022).

Here, we proposed an alternative scatter correction method based on a physics model and an iterative framework. Both Monte Carlo simulation and physical experimentation were conducted to emulate the X-ray scattering signals in the multi-source interior CT architecture, using a modified numerical CATphan® 600 phantom and a custom-built physical phantom respectively. A physics model was developed to analytically determine the magnitudes and distributions of X-ray scattering signals in the multi-source interior CT architecture. The angular distributions of first-order Compton scattering and Rayleigh scattering were calculated using the corresponding differential cross section formula, while the higher order scattering was assumed to be negligible. The truncated object volume was extended as elliptical water layers, to approximate the X-ray scattering signals originated in the region outside the interior field-of-view (FOV). Then, the physics model was integrated into an iterative framework to reduce the magnitudes of scatter artifact until the convergence criteria were reached. Quantitative evaluation was conducted to compare the image quality before and after scatter correction, wherein the "scatter-free" images from single-source global CT mode served as the reference for comparison. The contrast-to-noise ratio (CNR) and CT number deviation were employed as the quantitative metrics for image quality evaluation.

In multi-source interior CT architecture, X-ray scattering significantly degraded the image quality in both Monte Carlo simulation and physical experiments. Without the scatter correction, the multi-source interior CT mode reduced the CNR at the ROIs by < 68.5% and < 50.7% in the simulation and experiments respectively. The physics model based iterative scatter correction method largely reduced the scatter-induced projection error in

the sinograms and hence the scatter artifact in the reconstructed images, even after only one iteration. Within a few iterations, the updated sinograms and reconstruction results gradually converged toward the relevant references. With the proposed scatter correction methods, the CT number error at the ROIs was reduced to less than 46 HU in Monte Carlo simulation and 48 HU in physical experiments respectively. X-ray scattering can cause significant image quality degradation in the multi-source interior CT architecture. However, the proposed physics model based iterative scatter correction method can significantly improve the image quality.

Keywords: Multi-source, interior tomography, forward scattering, cross scattering, scatter correction

4.2 Introduction

The technical advancements of X-ray CT have been continued over the past decades, wherein lots of research efforts have been focused on the enhancement of temporal resolution. In clinics, high temporal resolution is especially desired for cardiovascular imaging [1-3], which is a major driving force for the technical developments of X-ray CT. The manufacturers have long pursued the faster gantry rotation speed and the higher X-ray source power, to push the limits of temporal resolution in CT scanners [4]. Nevertheless, both gantry rotation speed and X-ray source power are approaching their engineering limits [5]. By contrary, the multi-source CT schemes become the promising alternatives to further improve temporal resolution.

Nowadays, the clinical dual-source CT (DSCT) (Siemens SOMATOM) integrates two imaging chains in single rotary gantry to provide a substantial improvement of temporal resolution [6, 7]. Previously, several research groups have proposed a few conceptual multi-source CT schemes with the corresponding reconstruction algorithms. Zhao et. al. developed a filtered back-projection reconstruction algorithm for a triple-source cone-beam helical CT [8]. Yang et. al. proposed another saddle-curve scanning trajectory based triple-source cone beam CT and an exact filtered back-projection algorithm for image reconstruction [9]. Liu et. al. reported a high-level design of half-scan multi-source cone-beam CT with a generalized Parker's weighting scheme [10]. Zhao and Xi presented a field emitter based circular interlaced-source-detector-array CT [11]. Lately, some multi-source CT schemes have employed the interior tomography strategy (i.e. multi-source interior CT). For example, Wang et. al. proposed a general scheme of multi-source interior CT, wherein multiple ($\geq$ 7) X-ray sources were interleaved with the detectors around the patients [12]. Recently, Cao et. al. proposed a multi-source interior CT system architecture that simultaneously operates triple interior tomographic imaging chains formed by three pairs of the stationary X-ray source arrays and the rotary flat panel detectors [13]. There are two major advantages of integrating interior tomography into the multi-source CT schemes. First, interior tomography suppresses the radiation exposure to the surrounding tissues, by confining the X-ray beams to an internal region of interest (ROI) inside the patients [14, 15]. Second, interior tomography enables the implementation of more ($\geq$ 3) imaging chains in a given gantry space and hence further improve the temporal resolution, since smaller X-ray detector can be utilized in the interior imaging chain [16]. Therefore,

the multi-source interior CT architectures bring the promises to the CT imaging applications that place a strict demand on high temporal resolution (e.g. all-phase cardiac CT imaging) [13].

Despite the improvement of temporal resolution, multi-source CT schemes can suffer from more complex impacts of X-ray scattering. In multi-source CT, the X-ray scattering signals are raised both within and across the individual imaging chains, and thus the X-ray detectors detect the scattering signals from a wide range of scatter angles. At each detector, the "forward scattering" photons are originated from the X-ray source on the opposite side, while the "cross scattering" photons are originated from the X-ray sources of different imaging chains [17]. The cross scattering signals are superposed onto the forward scattering signals at the X-ray detector, and hence cause a worse X-ray projection error which then propagate into the CT images via reconstruction. The cross scattering signals will eventually further degrade the contrast-to-noise ratio (CNR) and the CT number accuracy in the reconstruction results. Although interior tomography tends to reduce the size of FOV in the multi-source CT schemes, the utilization of X-ray cone-beams with the increased z-coverage can still cause the irradiation of a considerable object volume and thus induce significant scatter artifact to the reconstructed images [18]. Therefore, it is necessary to develop dedicated scatter correction techniques to address the deteriorated scatter artifact in multi-source CT schemes.

The approaches of forward scattering correction have been extensively studied in the standard single-source CT [19, 20]. The forward scattering signals can be estimated from

experimental measurements or physical-mathematical models. As for the measurement-based estimation, many variants of the beam-stopper-array (BSA) based approaches have been proposed to directly measure forward scattering signals in the BSA shadow [21-23]. As for the model-based estimation, the X-ray projections or the reconstructed CT images are respectively fed to 2D or 3D theoretical models to calculate the magnitudes and spatial distributions of forward scattering signals. For example, Sun and Star-Lack proposed to adapt the scatter kernels to the local object thickness, and then superpose these scatter kernels to deconvolve the forward scattering signals from the X-ray projections [24]. Meyer et. al. developed a convolution kernel based algorithm to estimate the spatial distribution of the forward scattering signals in X-ray projections, and combined this algorithm with an object-size-dependent scaling derived from Monte Carlo simulation [25]. Poludniowski et. al. proposed an accelerated Monte Carlo simulation for forward scattering estimation, wherein a coarse volumetric image reconstruction was combined with a special "fixed forced detection" technique [26]. On the contrary, there are few dedicated cross scattering correction methods in the previous literature. The insufficiency of the conventional anti-scatter grid, air gap and bow-tie filter for cross scattering suppression has been demonstrated in dual-source CT [17, 27]. Previously, the manufacturer (Siemens Healthcare) developed two dedicated scatter correction approaches in dual-source CT [28]: the first method measured X-ray scattering signals by dedicated scatter sensors that were placed outside the X-ray beams in the z-direction, and the second method employed a look-up table of the cross scattering signals derived from previous phantom experiments and Monte Carlo simulation. Moreover, Ren et. al. presented another

measurement-based scatter correction method in dual-source CT, wherein a BSA was mounted in front of each X-ray source and shifted between two complementary locations to obtain the complete measurements of patient projections and total scattering signals (i.e. forward scattering and cross scattering) at each view angle [29]. Our group has recently developed a stationary BSA array based method and a source-trigger-sequence based method to enable the online measurement and correction of cross scattering signals in the multi-source interior CT [18]. Thus far, the hardware-based scatter correction methods typically cause certain modifications of the imaging system configuration (e.g. BSA or scatter sensors), while the model-based methods frequently induce heavy workload in the numerical computation (e.g. Monte Carlo simulation) and / or the parametric calibration (e.g. scatter kernel convolution).

In this work, our objective is to develop an alternative model-based scatter correction technique with a relatively better computational efficiency, for our previously presented multi-source interior CT architecture [13]. Briefly, we propose here to combine a deterministic physics model of the multi-source interior CT with an iterative scatter correction framework to suppress the scatter artifacts induced by both forward scattering and cross scattering. The spatial distributions of first-order forward scattering and cross scattering signals were analytically determined by using the physical laws of the scatter-angle cross sections. The surrounding region outside the interior FOV was approximated via the reconstruction of the extrapolated X-ray projections. The scatter correction started with a coarse estimation of X-ray scattering signals derived from the scatter-contaminated

CT images. The scatter artifacts were gradually removed with more iterations of correction. In addition, we conducted Monte Carlo simulation and physical phantom experimentation to synthesize the primary X-ray signals, forward scattering signals and cross scattering signals in multi-source interior CT, and the proposed scatter correction method was validated using the synthesized multi-source interior CT data.

The rest part of this paper is organized as follows. In section 2, we will first present the introduction of the multi-source interior CT architecture, the Monte Carlo simulation and the physical experiments. Then, we will introduce the physical model and the iterative scatter correction framework with details. In section 3, we will demonstrate the qualitative and quantitative results before and after scatter correction, both for the Monte Carlo simulation and the physical experiments. In the last section, we will conclude this paper with a discussion of the results.

4.3 Methods

4.3.1 System overview

The schematics of the multi-source interior CT system architecture is illustrated in Figure 3-1. Three stationary source arrays and three rotary flat panel X-ray detectors are mounted respectively outside and on the rotary gantry, which constitutes three simultaneously operative imaging chains. Both the source arrays and the detectors are placed symmetrically around the system rotation axis, and the total angular coverage of the three

imaging chains enables a short CT scan (i.e. 180˚ + fan angle). On the opposite sides of the detectors, three interior collimators are fixed on the rotary gantry to confine the X-ray beams to an internal ROI inside the patient. For each source array, an array of cathodes (e.g. hot dispenser cathode [30] or cold carbon-nanotube field emitter [31]) are integrated into the same envelope to generate an array of X-ray beams at successive view angles. The X-ray beams can be activated electronically by applying proper gate voltages to the cathodes. Especially, the cold carbon-nanotube cathodes can enable the programmable X-ray emissions under the faster and more flexible control, via utilizing a pre-programmed electronic trigger sequence to switch on and off the gate voltages on individual cathodes [32]. Therefore, the X-ray beams can be electronically swept through the successive view angles for tomographic imaging without the rotation of X-ray source [33]. More details about this system configuration can be found in the reference [13].

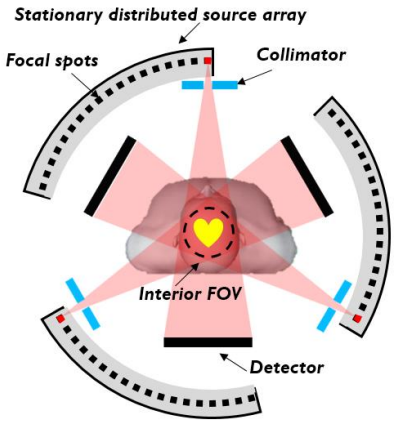

Figure 4-1 A schematic of the stationary X-ray source arrays based multi-source interior CT architecture. This architecture consists of three stationary source arrays and three rotary X-ray detectors. The interior collimators are fixed on the rotary gantry opposite to the detectors.

4.3.2 Numerical simulations and physical experiments

We conducted numerical simulations and physical experiments to emulate the X-ray scattering signals in multi-source interior CT system architecture. For numerical simulation, a previously published Monte Carlo simulation package with GPU-acceleration technique [34] was utilized to simulate the photon interactions with matters, wherein the photoelectric absorption, Compton scattering and Rayleigh scattering were all included in the simulation. A modified numerical CATphan® 600 phantom served as the imaging subject. The standard numerical CATphan® 600 phantom was downsized to be 120 mm in diameter, and then it was inserted into the center of a water cylinder (256 mm in diameter). Table 3-1 lists the major parameters of system geometry and scanning protocols. The X-ray source was operated at 80 kV with 2.3 mm aluminum filtration at the source side. The simulated CT scans were conducted in the single-source global CT mode and multi-source interior CT mode, respectively. In interior CT mode, the cone-beam angle was fixed at 13° to yield a spherical interior FOV (120 mm in diameter) at the isocenter.

Table 4-1. Parameters of imaging geometries and scanning protocols.

Source-Isocenter distance (mm)	520
Source-detector distance (mm)	940
Field-of-view at isocenter (mm)	120
Total coverage angle (°)	219
Step angle per projection (°)	1
Source voltage (kV)	80
Total mAs	50

For physical experiments, an in-house CT imaging platform was devised to experimentally emulate the multi-source interior CT system architecture (Figure 3-2A). It was comprised of a standard X-ray source (Oxford instrument, Inc.), a flat panel X-ray detector (Hamamatsu, Inc.) and several mechanical stages. A customized CT phantom was fabricated (250 mm in diameter and 310 mm in height) for the experiments. It was constituted with heterogeneous materials such as acrylic tubes/blocks, animal ribs, water, glass rods, iodine, corn oil, calcium carbonate, aluminum oxide and polyethylene tubes. The physical experiments utilized the same imaging geometry and scanning protocols as the Monte Carlo simulation (Table 3-1). This experimental platform can be flexibly re-configured to execute the tomographic imaging at the conventional single-source global CT mode and multi-source interior CT mode. In interior CT mode, an aperture collimator was mounted near the exit window of the X-ray source, to confine the cone-beam angle to 13°. The method to synthesize the X-ray signals in multi-source interior CT mode is briefly

summarized as follows (Figure 3-2B). First, the X-ray source was placed on the opposite side of the detector, to obtain the primary X-ray signals and forward scattering signals at view β. Then, the cross scattering signals from the two "cross" sources were directly measured by re-positioning the source at two cross angles (i.e. views β+120° and β+240° respectively). It is known that X-ray scattering can be assumed as the additive signals superposed onto the primary X-ray signals [19, 20]. Therefore, in the multi-source interior CT mode, the total X-ray signals at a detector can be synthesized by the superposition of the primary signals, forward scattering signals, and cross scattering signals.

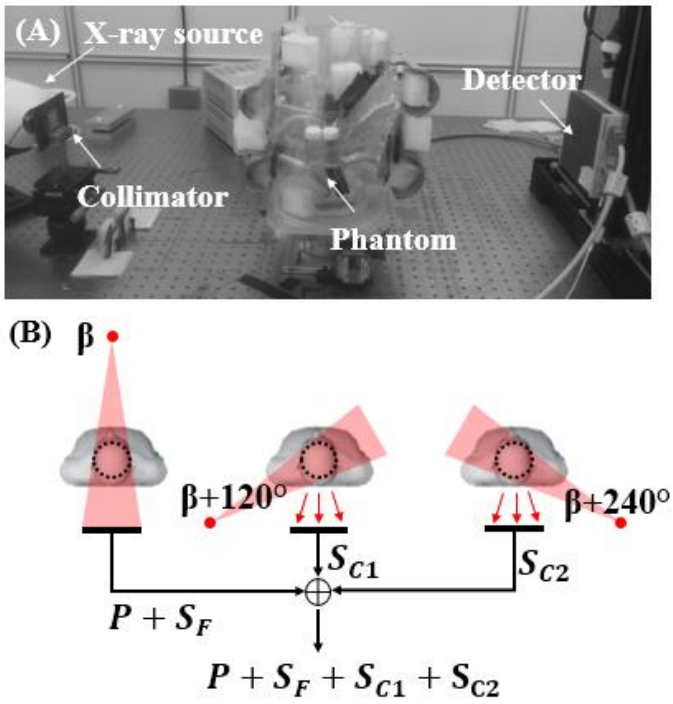

Figure 4-2. (A) Experimental setup of the imaging platform. (B) Illustration of the experimental synthesis of total X-ray signals in the multi-source interior CT mode.

4.3.3 Physics model

A physics model was developed for scatter estimation in the multi-source interior CT system architecture. Our model employed the physical laws to deterministically calculate the X-ray scattering signals. Specifically, Klein-Nishina formula modified by the incoherent scattering function was utilized to calculate Compton scattering cross section per atom [35]:

$$\frac{d\sigma_C(\theta, E, Z)}{d\Omega} = \frac{r_e^2}{2}[1 + k(1 - \cos\theta)]^{-2}\left[1 + \cos^2\theta + \frac{k^2(1 - \cos\theta)^2}{1 + k(1 - \cos\theta)}\right]S(x(\cos\theta, E), Z) \quad (1)$$

$$k = \frac{E}{511.0034} \quad (2)$$

$$x(\cos\theta, E) = \frac{1}{\lambda}\sin\frac{\theta}{2} \quad (3)$$

where θ is the scatter angle, E is the incident photon energy, Z is the atomic number, Ω is the solid angle, r_e is the classical electron radius, k is the photon energy in units of the electron rest mass energy, λ is the photon wavelength, and S is the molecular incoherent scattering function. Moreover, Rayleigh scattering cross section per atom was calculated by utilizing Thompson scattering formula modified by atomic form factor [35]:

$$\frac{d\sigma_R(\theta, E, Z)}{d\Omega} = \frac{r_e^2}{2}[1 + \cos^2\theta]\,[F(x(\cos\theta, E), Z)]^2 \quad (4)$$

where F is the atomic form factor. Note that the X-ray scattering cross section for compounds can be calculated by utilizing the weighted sums of the corresponding angular

distribution for individual elements [36, 37]. In the equations above, incoherent scatter function and atomic form factor were tabulated using NIST reference database [35, 36].

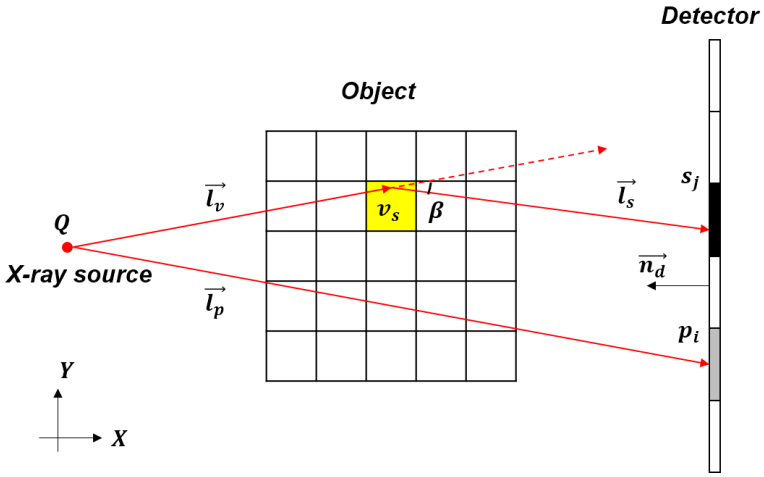

Figure 4-3. Schematics of the simulations of primary signals and scattering signals. For primary X-ray signals, the unscattered primary photons propagate from the X-ray source to i^{th} detector element through a primary ray path l_p. For X-ray scattering signals, the photons first propagate from the source to the scatter site v_s along a partial primary ray path l_v and then the scattered photons are eventually detected at the j^{th} detector element.

The principles of the simulation of X-ray signals are illustrated in Figure 4-3. The Siddon's algorithm [38] based three dimensional ray tracing was employed to identify the ray paths for both primary and scattering signals in the simulation. The entire volume of reconstructed CT images was utilized as a discretized model of objects. For the calculation of primary X-ray signals, X-ray attenuation was integrated along the primary ray paths through the objects. The primary X-ray signals were calculated as the energy fluence of the primary photons absorbed by individual detector element:

$$p_i(\gamma) = Q\frac{E_0}{4\pi\left\|l_p\right\|_2^2}\exp\left(-\int_{l_p}\mu_t dt\right)\left(\int_{A_d} d^2n\cos\alpha\right)\left[1-\exp\left(-\mu_{d,E0}d_{det}\right)\right] \quad (5)$$

Where $p_i(\gamma)$ is the energy fluence of primary X-ray signals at the i^{th} detector element at view γ, Q is the number of photons emitted from the X-ray source, E_0 is the primary photon energy, l_p is the X-ray path from X-ray source to the center of i^{th} detector element, μ_t is the linear attenuation coefficient, A_d is the area of each detector pixel, $d^2n\cos\alpha/\left\|l_p\right\|_2^2$ is the solid angle subtended by individual detector element, α is the angle between the detector normal $\overrightarrow{n_d}$ and the ray path l_p, $\mu_{d,E0}$ is the energy absorption coefficient of the detector material and d_{det} is the detector thickness. On the other hand, the X-ray scattering signals were calculated as the energy fluence of the scattered photons absorbed by individual detector elements. We first calculated the number of the photons scattered in a particular voxel v_s (i.e. a scatter site), and the corresponding energy fluence of scattered photons absorbed by the j^{th} detector element:

$$\begin{aligned} s_{j,v_s}(\gamma) = Q\frac{E_s}{4\pi\|l_v\|_2^2}\left(\int_{v_s}\rho_v dv\right)\left(\frac{d\sigma_S(\beta,E_0,Z)}{d\Omega}\right)\exp\left(-\int_{l_v}\mu_t dt\right. \\ \left.-\int_{l_s}\mu_s dt\right)\left(\frac{\cos\alpha'}{\|l_s\|_2^2}\int_{A_d} d^2n\right)\left[1-\exp\left(-\mu_{d,Es}d_{det}\right)\right] \end{aligned} \quad (6)$$

$$E_s = \begin{cases} \dfrac{E_0}{1+\dfrac{E_0}{511.0034}(1-\cos\beta)} & \text{for Compton scattering} \\ E_0 & \text{for Rayleigh scattering} \end{cases} \quad (7)$$

$$\frac{d\sigma_S(\beta, E_0, Z)}{d\Omega} = \frac{d\sigma_C(\theta, E, Z)}{d\Omega} + \frac{d\sigma_R(\theta, E, Z)}{d\Omega} \quad (8)$$

where $s_{j,v_s}(\gamma)$ is the energy fluence of the photons scattered at the voxel v_s and then detected by the j^{th} detector element, E_s is the energy of the scattered photon, l_v is the ray path from X-ray source to the voxel v_s, l_s is the ray path from voxel v_s to the center of the j^{th} detector element, ρ_v is the molecular density in v_s, β is the scatter angle, μ_t is the linear attenuation coefficient for incident photons propagating along l_v, μ_s is the linear attenuation coefficient for the scattered photons propagating along l_s, α' is the angle between the detector normal and l_s. Finally, we integrated the scattering signals originated in all scatter sites:

$$S_j(\gamma) = \int_V s_{j,v_s}(\gamma) dv \quad (9)$$

where V is the collection of all scatter sites at view γ, and $S_j(\gamma)$ is total scattering signals at the j^{th} detector element.

As for the implementation, several simplifications were applied to improve the computational efficiency. First, the X-ray source was simplified to be an isotropic point source and thus the penumbral effects from the focal spot was not included in the physics model. The photon energy of the incident X-ray photons was fixed at the mean energy of the polychromatic spectrum. Second, for the ray tracing of scattered X-ray signals, the ray paths were assumed to start from the point source, then pass through the centroid of the scatter sites, and finally reach the center of the detector elements. Similarly, for the ray

tracing of primary X-ray signals, the ray paths were assumed to directly connect the point source and the center of individual detector element. Third, the second and higher ordered X-ray scattering signals were assumed to be negligible, and thus only the first-order X-ray scattering signals were estimated. This is because the occurrence of first order X-ray scattering dominates the majority part of the total scattering events. Forth, the X-ray scattering cross section of any non-water material was approximated by that of water, since the chemical formulas of that material may not be available in practice. Briefly, the scattering cross section of water was weighted by an estimated molecular density of the particular non-water material, wherein the estimated molecular density was derived from an empirical bi-linear relationship based on the scaled Hounsfield units (Figure 3 in the reference [39]). Finally, the analytically calculated X-ray signals was scaled to match the magnitudes of the actual X-ray signals [40], since flat panel X-ray detectors typically have a linear response to the energy fluence of the detected photons.

4.3.4 Iterative scatter correction

We employed the previously published iterative image improvement framework to obtain the "scatter-free" images in multi-source interior CT [41, 42]. Briefly, the scatter estimation and correction were conducted immediately after the completion of the interior ROI reconstruction, wherein the residual magnitudes of scatter artifacts gradually decreased until the convergence was reached. The workflow of this iterative scatter correction method is illustrated in Figure 4-4. First, the original scatter-contaminated X-ray projections were

used to reconstruct a volume of CT images of the objects. The total variation minimization (TVM) based simultaneous algebraic reconstruction technique (SART) algorithm was employed for image reconstruction [43]. Second, the latest volumetric CT images were fed into the physics model to estimate both forward and cross scattering signals in multi-source interior CT. Third, for scatter correction, the simulated total X-ray scattering signals were subtracted from the original scatter-contaminated X-ray projections. The second and third steps were repeated until the averaged absolute percentage differences (AAPD) of the intermediate reconstruction results or the "scatter-corrected" X-ray projections were less than a small number, or when the maximal number of iterations was reached [19]:

$$\frac{1}{M}\sum_{i}\left|\frac{f_i^{k+1}-f_i^{k}}{f_i^{k}}\right|\times 100\% \le \varepsilon \text{ or } \frac{1}{T}\sum_{i}\left|\frac{L_i^{k+1}-L_i^{k}}{L_i^{k}}\right|\times 100\% \le \varepsilon \text{ or } k \ge N \qquad (10)$$

where f_i^k is the i^{th} image voxel of the intermediate CT image at k^{th} iteration, M is the number of voxels, L^k is the scatter-corrected X-ray projections at k^{th} iteration, $\varepsilon \in \mathbb{R}$ is a small constant number (fixed at 1%), T is the number of detector pixels and N is the maximal number of iterations (fixed at 10). Note that, in the aforementioned steps, the model-based scatter estimation were carried out with a coarse image reconstruction (voxel size 0.4^3 cm^3). When the convergence was reached, the "scatter-free" X-ray projections were used to reconstruct CT images with higher resolution (voxel size 0.06^3 cm^3).

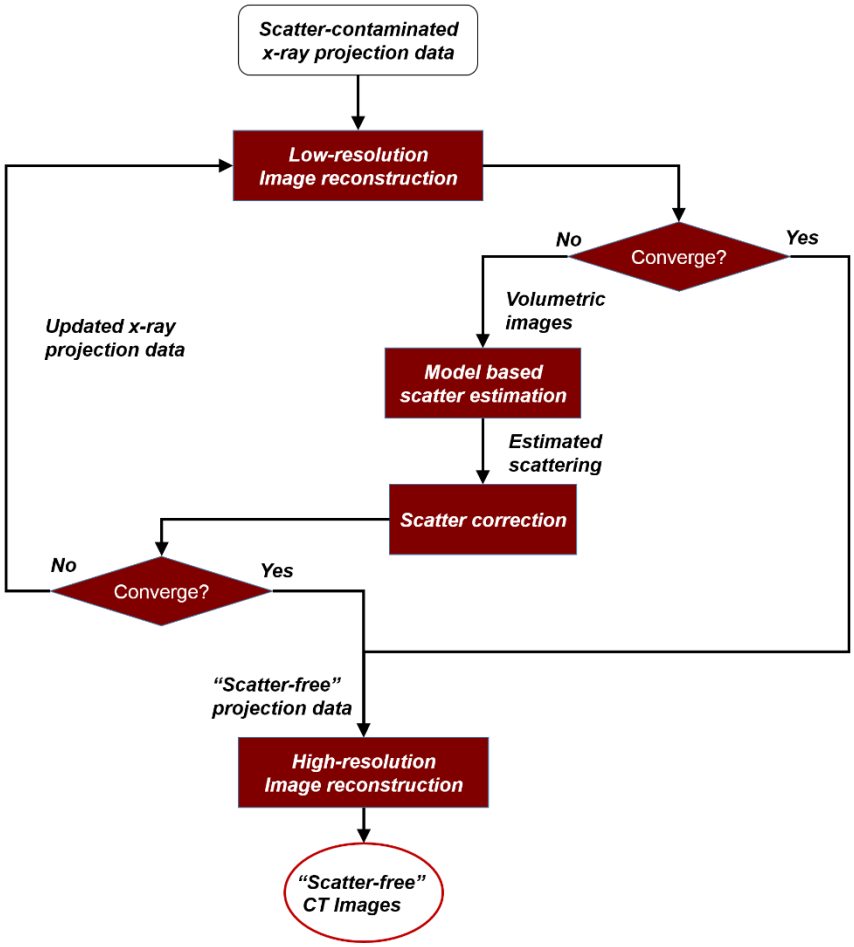

Figure 4-4. The flowchart of the iterative scatter correction method. In the initial iteration, the scatter-contaminated raw projection data was used to reconstruct images for the physics model based scatter estimation. The estimated total scattering signals were subtracted from the raw projections. The updated projections were used in the image reconstruction which then fed to the next iteration of scatter correction. These steps were iterated when the updated reconstruction results or X-ray projections satisfied the convergence criteria.

Note that the interior tomography induced significant volume truncation along the lateral and the longitudinal directions in multi-source interior CT. The physics model would

severely reduce the accuracy of the estimated X-ray scattering signals, if no volume extension methods were applied to approximate the outer region (i.e. the object volume outside the interior FOV). To address this problem, we applied a method similar to the image based object size estimation (IBSE) from the reference [25]: First, the interior X-ray projections were detruncated by applying extrapolation up to the estimated object boundaries (Figure 4-5A); Second, the object volume was then extended using the extrapolated projections, via image reconstruction (Figure 4-5B); Third, the boundary of outer region was approximated by applying elliptical fitting to the outline of the reconstructed images (Figure 4-5C); Finally, the elliptical outer region was filled with water (Figure 4-5D).

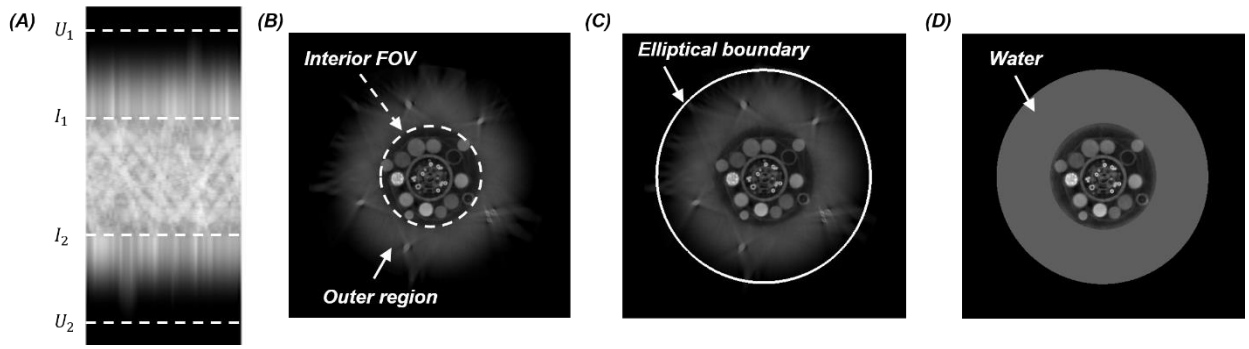

Figure 4-5. (A) The sinogram of the interior FOV (from I_1 to I_2) extended up to the object boundaries (U_1 and U_2). The extrapolated projection data corresponds to the region between U_1 and I_1 and the region between I_2 and U_2. (B) The reconstructed image from (A). (C) An elliptical curve is fitted to the boundary points of the outer region. (D) The outer region is finally approximated by an elliptical water layer.

4.3.5 Evaluation methods

We evaluated the convergence of the proposed scatter correction method, using the CT data from Monte Carlo simulation and physical experimentation. The iteratively updated X-ray projections were evaluated against the number of iterations of the scatter correction, wherein the "scatter-free" projections from the global CT mode served as the reference of evaluation. Moreover, after each iteration of scatter correction, the intermediate reconstruction results were evaluated against the "scatter-free" images from global CT mode. For Monte Carlo simulation, the scatter-free projections were derived from the simulated primary X-ray signals. For physical experiments, the "scatter-free" projections were experimentally measured from the global fan-beam CT mode (3 mm beam thickness), since the X-ray scattering in fan-beam CT is typically negligible [23]. In addition, AAPD of the intermediate reconstruction results and X-ray projections were calculated for all iterations of the scatter correction.

Then, we compared the scatter-primary-ratio from our physics model with the respective references from both Monte Carlo simulations and physical experiments, after the scatter correction reached the convergence. For Monte Carlo simulation, the primary X-ray signals, forward scattering signals and cross scattering signals were simulated separately to calculate the forward-scatter-to-primary-ratio (FSPR) and the cross-scatter-to-primary-ratio (CSPR). For physical experiments, these X-ray signals were measured to calculate the FSPR and the CSPR. The primary X-ray signals was directly measured in single-source fan-beam CT mode with a slit collimator (3 mm fan-beam thickness). This is because the

X-ray scattering signals are typically negligible in fan-beam CT [23]. Then, the forward scattering signals were calculated by subtracting the primary X-ray signals from the projection data obtained from the single-source cone-beam CT mode, while the cross scattering signals were directly measured by re-positioning the source at the cross angles of the detector (Figure 3-2B).

Then, we compared the image quality before and after scatter correction, to evaluate the efficacy of our methods in both Monte Carlo simulation and physical experiments. As to image reconstruction, the TVM based SART algorithm was employed in both single-source global CT mode and multi-source interior CT mode. For Monte Carlo simulation, the global CT image reconstructed from the primary X-ray signals were employed as the reference image for the evaluation of image quality. For physical experiments, the global fan-beam CT image (3 mm beam thickness) was used as the "scatter-free" reference image. The image quality was quantitatively evaluated by using two metrics: contrast-noise-ratio (CNR) and CT number accuracy. The CNR can be calculated as follows:

$$\mathrm{CNR} = \frac{|\mu_1 - \mu_2|}{\sqrt{\sigma_1^2 + \sigma_2^2}} \tag{11}$$

Where μ_1 and μ_2 are the mean CT numbers in two selected ROIs, σ_1 and σ_2 are the respective standard deviation of these two ROIs. CT number accuracy was analyzed by using the mean absolute error (MAE):

$$\mathrm{MAE} = \frac{1}{\mathrm{N}}\sum_{\mathrm{k}=1}^{\mathrm{N}}\left(\left|\mathrm{p_{k,i}} - \mathrm{p_{k,r}}\right|\right) \tag{12}$$

Where $p_{k,i}$ and $p_{k,r}$ are k^{th} pixels from the same ROIs of the multi-source interior CT images and the reference images respectively, and N is the number of pixels in those ROIs. The location of ROIs is shown in Figure 3-6. The sizes of ROIs were 24 mm^2 and 34 mm^2 in simulation and experiments respectively.

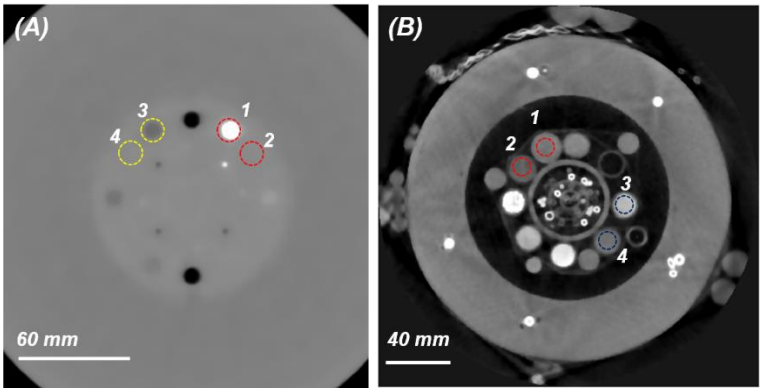

Figure 4-6. The location of ROIs for the analysis of CNR and CT number deviation in (A) numerical CATphan 600 phantom and (B) in-house physical phantom. The images were zoom-in for display purpose.

4.4 Experimental results

Figure 4-7 demonstrates the sinograms of the central slice of CATphan 600 phantom at successive iterations of scatter correction. Figure 4-8 shows the corresponding reconstruction results. Before scatter correction, the X-ray scattering induced significant downward deviation in the sinogram (Figure 4-7A1), which then caused the significant cupping artifact across the interior FOV (Figure 4-8A1). The scatter-induced projection error was gradually removed from the sinograms. In the 4^{th} and 5^{th} iterations (Figure 4-8A5

& A6), the updated sinograms became comparable to the reference sinogram, despite the increased noise level after scatter correction. Consequently, the cupping artifact and the CT number deviation were iteratively suppressed in the reconstructed images and thus the image quality was improved to be comparable to the reference image. Figure 4-9A plots the line profiles extracted from the reconstructed images in Figure 4-8, and Figure 4-9B plots the curves of AAPD of the intermediate sinograms and reconstruction results. The AAPD was quickly reduced from < 30.0% to < 1.0% within 5 iterations. Note that an obvious quality improvement can be observed even after the 1st iteration. Table 4-2 demonstrates the CNR and the CT number error of the pre-selected ROIs (Figure 3-6A) in numerical CATphan phantom. Without scatter correction, the CNR degradation was up to 64.9% and the CT number error was up to 1122 HU. After the model-based scatter correction, CNR was largely improved and CT number error was reduced to < 46 HU.

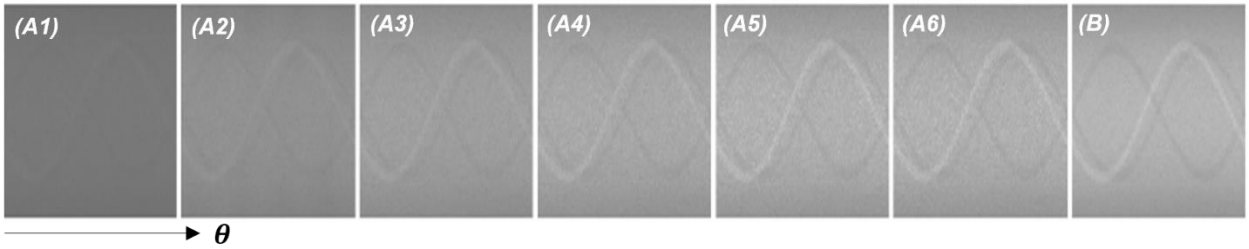

Figure 4-7. The intermediate sinograms of the central slice of CATphan phantom at different iterations of scatter correction. (A1): the initial sinogram without scatter correction. (A2) – (A5): the sinograms from the 1st to 5th iterations of scatter correction. Subfigure (B) is the reference sinogram from the global fan-beam CT. All sinograms are demonstrated with the same display window.

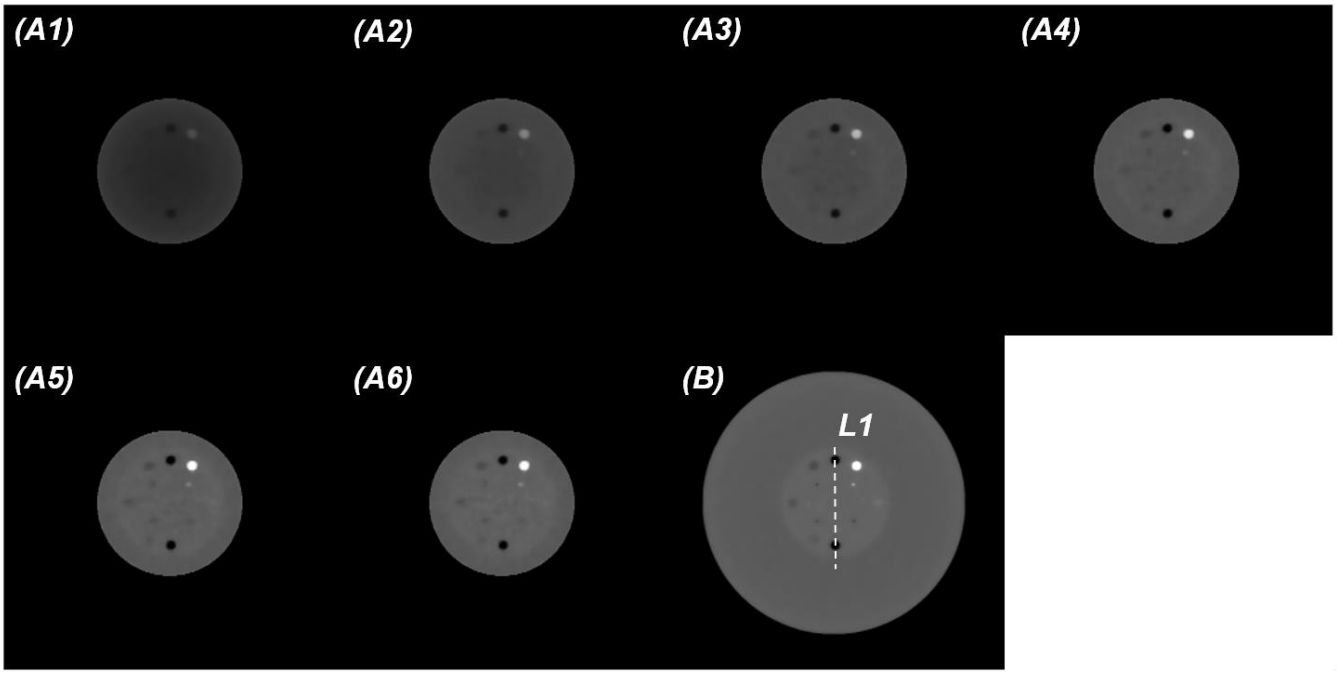

Figure 4-8. The intermediate reconstruction results of the central slice of the CATphan 600 phantom at different iterations of scatter correction. (A1): the scatter-contaminated CT image before scatter correction. (A2) – (A6) are from the 1st iteration to the 5th iteration. Subfigure (B) is the reference image from global CT mode. Display window of (A1) – (B) [-1000 1200] HU.

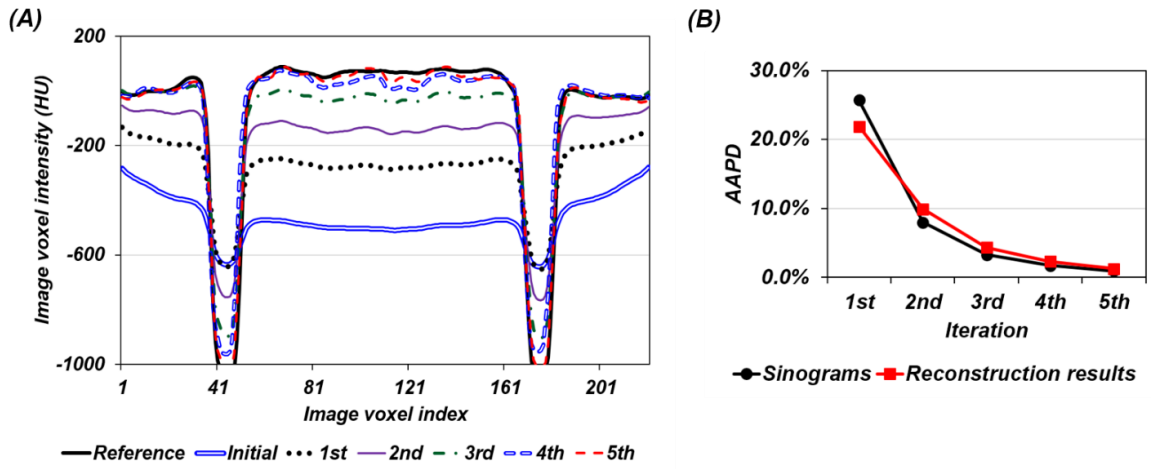

Figure 4-9. (A) L1 line profiles extracted from Figure 4-8. (B) The AAPD of the intermediate sinograms and the corresponding reconstruction results of the central slice of CATphan 600 phantom.

Table 4-2. Contrast-to-noise ratio (CNR) and mean absolute error (MAE) of ROIs 1-4 in the experiments. a – "Scatter-free" reference; b –Multi-source interior CT w/o scatter correction; c – Multi-source interior CT with scatter correction.

		a	c	d
CNR	ROI 1 vs ROI 2	40.0	30.0	34.0
	ROI 3 vs ROI 4	15.1	5.3	12.0
MAE (HU)	ROI 1	-	1122	46
	ROI 2	-	578	41
	ROI 3	-	405	35
	ROI 4	-	583	43

Figure 4-10 plots the profiles of FSPR and CSPR from analytical model (after scatter correction converged at the 5th iteration) and Monte Carlo simulation. Both the analytically

calculated FSPR and CSPR are close to their counterparts from Monte Carlo simulation, despite some minor discrepancy. The possible reasons of such discrepancy will be discussed in Sec. 4.

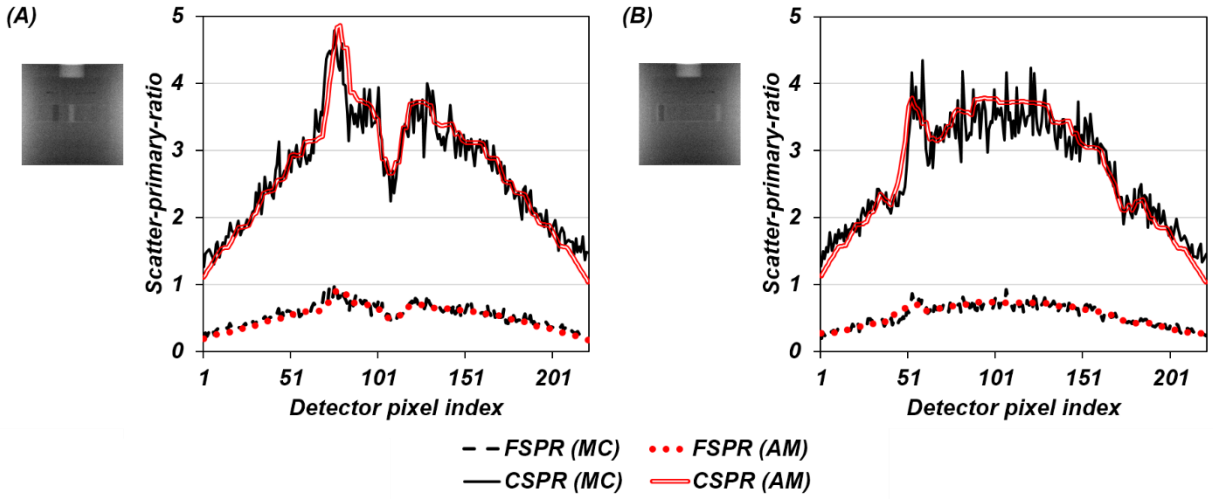

Figure 4-10. The comparison of pixel-wise scatter-primary-ratio (SPR) at the central detector row, respectively at views (A) 180° and (B) 270°. FSPR (MC) & CSPR (MC): FSPR and CSPR from Monte Carlo simulation. FSPR (AM) & CSPR (AM): FSPR and CSPR from analytical model. Both FSPR (AM) and CSPR (AM) were calculated after the iterative scatter correction stopped. Insets: X-ray projections of CATphan phantom.

Figure 4-11 demonstrates the sinograms from different iterations of the scatter correction for physical experiments, and Figure 4-12 shows the corresponding reconstruction results of the interior FOV. After the initial iteration, the scatter-induced projection error were largely corrected from the initial sinogram (Figure 4-11A2). With more iterations, the "scatter-corrected" sinograms from multi-source interior CT gradually converged toward the reference (Figure 4-11B). Consequently, the scatter artifact was iteratively suppressed

and hence the image quality was gradually improved to that of the reference image. Moreover, Figure 4-13A plots out the line profiles extracted from the reconstruction results in Figure 4-12, and Figure 4-13B shows the corresponding AAPD after each iteration of the scatter correction. Within 4 iterations, the line profiles converged toward the reference and thus CT number accuracy was improved. The AAPD of the intermediate sinograms and reconstruction results were reduced to < 1 % and < 4% respectively. Table 4-3 shows the comparison of CNR and CT number error, before and after scatter correction, at the ROIs (Figure 3-6B) in physical phantom. Before the scatter correction, CNR was degraded by up to 50.7% and the CT number error was up to 929 HU. After the scatter correction converged, CNR was improved by 40% and CT number error was reduced to < 48 HU.

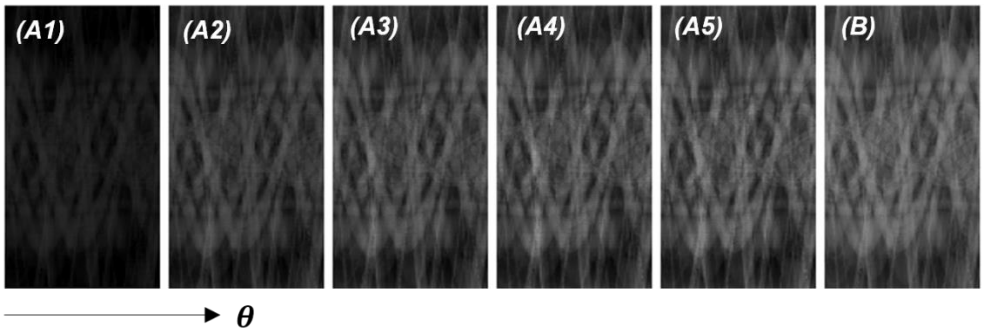

Figure 4-11. The intermediate sinograms of the central slice at different iterations of the iterative scatter correction in multi-source interior CT architecture. Subfigures (A1) – (A5) are from 1st to 5th iteration. The sinograms in (A1) – (A5) were truncated due to interior tomography. Subfigure (B) is the reference sinogram obtained from the global fan-beam CT, and it corresponds to the same interior ROI in (A1) – (A5). All of these sinograms are displayed in the same window. θ indicates the view angles.

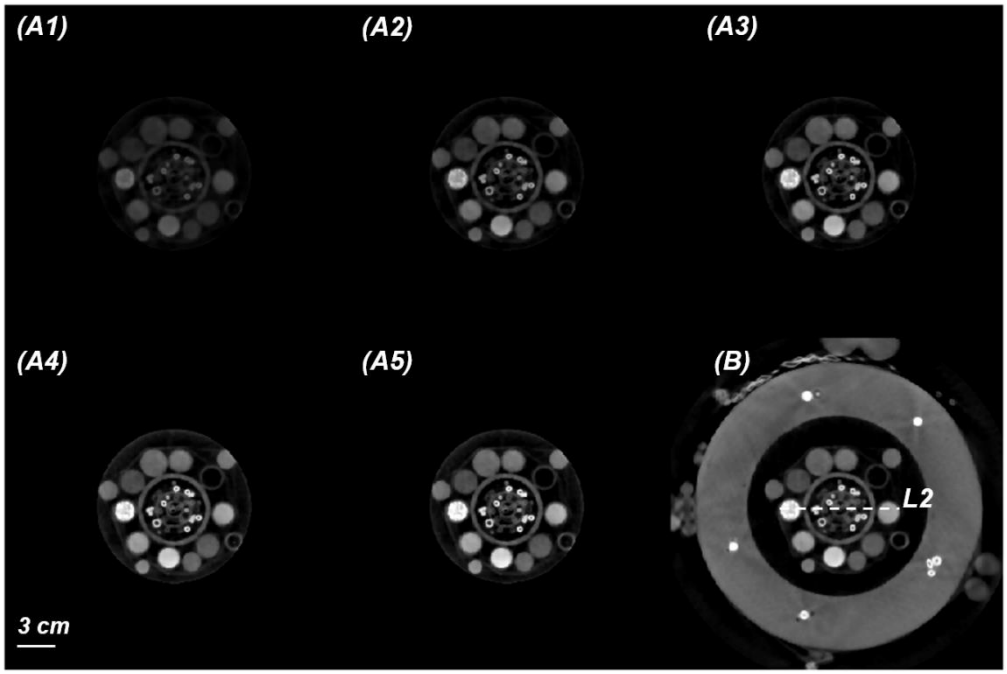

Figure 4-12. (A1): the original image without scatter correction. (A2) – (A5): the intermediate reconstruction results (zoom-in) of the central slice of the physical phantom, from the 1st iteration to 4th iteration. (B): the reference image of the central slice acquired from global fan-beam CT scan. Display window [-1000 1800] HU. White dashed line (L2) indicates the location of the line profiles shown in Figure 4-13A.

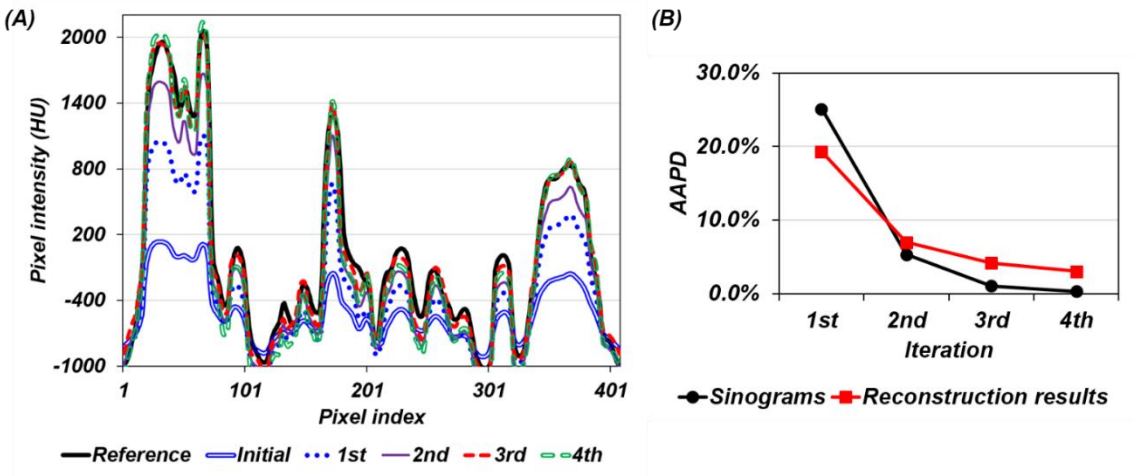

Figure 4-13. (A) L2 line profiles extracted from the reconstruction results in Figure 4-12. (B) The AAPD of the intermediate sinograms and the corresponding reconstructed images of central slice for physical phantom.

Table 4-3. Contrast-to-noise ratio (CNR) and mean absolute error (MAE) of ROIs 1-4 in the experiments. a – "Scatter-free" reference; b –Multi-source interior CT w/o scatter correction; c – Multi-source interior CT with the proposed scatter correction.

		a	b	c
CNR	ROI1 vs ROI2	7.1	3.5	4.9
	ROI3 vs ROI4	40.6	32.5	37.0
MAE (HU)	ROI1	-	478	45
	ROI2	-	383	38
	ROI3	-	929	48
	ROI4	-	445	43

Figure 4-14 demonstrates the line profiles of the FSPR and CSPR from analytical model and physical experiments, respectively. Despite the minor discrepancy, it is easy to observe

that the profiles of analytically calculated FSPR and CSPR were comparable to their counterparts measured in physical experiments.

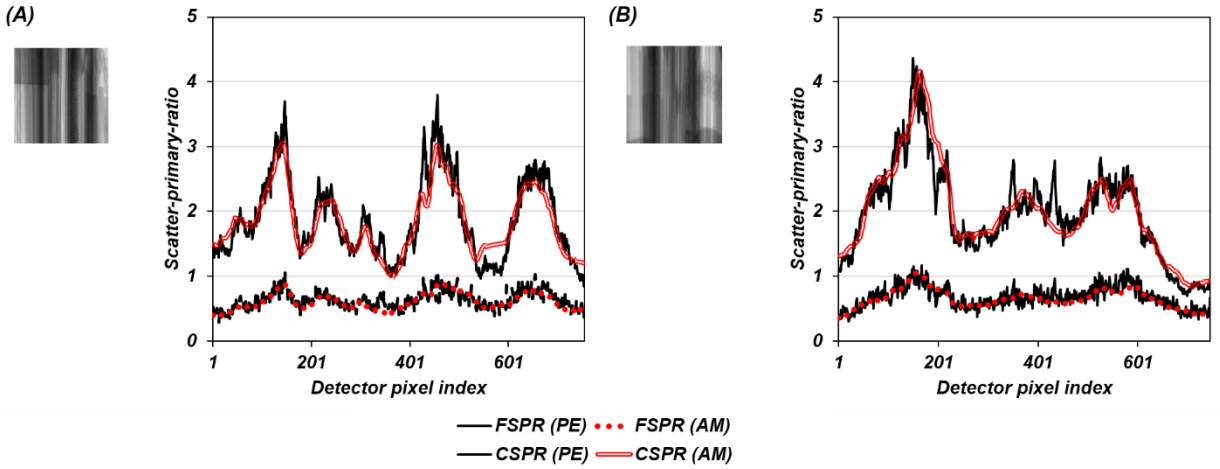

Figure 4-14. The comparison of pixel-wise scatter-primary-ratio at the central detector row, respectively at views (A) 60° and (B) 310°. FSPR (PE) & CSPR (PE): FSPR and CSPR measured in physical experiments. FSPR (AM) & CSPR (AM): FSPR and CSPR from analytical model. Both FSPR (AM) and CSPR (AM) were calculated after the iterative scatter correction stopped. Insets: X-ray projections of physical phantom.

4.5 Discussion and conclusion

We conducted the multi-source interior CT scans, both numerically and experimentally, via Monte Carlo simulation and imaging experimentations. The simulated and the measured cross scattering signals were then superposed onto the forward scattering and primary signals to synthesize the total X-ray signals in multi-source interior CT. Then, we developed a deterministic physics model to analytically calculate the X-ray forward

scattering and cross scattering signals. In our physics model, the scatter-contaminated CT images served as the initial representation of the objects, while then the scatter correction was conducted iteratively to reduce scatter artifacts until the convergence criteria were achieved. The analytically calculated FSPR and CSPR from our physics model became comparable to their respective references from Monte Carlo simulation or physical experiments, when the iterative scatter correction converged. The image quality was qualitatively and quantitatively evaluated before and after scatter correction.

In the experimental results, we could observe some discrepancy in the profiles of FSPR and CSPR. This phenomenon could be attributed to the following major reasons. First, during the iterative scatter correction, the phantoms were represented by the coarsely discretized CT images, and thus the partial volume effect could raise discrepancy between the analytically calculated forward projections and the corresponding references. Second, the outer region was approximated by elliptical water layers, because of the projection truncation induced by interior CT mode. The approximation error of the outer region could also partially raise the discrepancy. Third, the scattering cross section was calculated based on the assumption that all materials (except for the air) were water-like. Forth, the incident primary photons were assumed to be monochromatic and the corresponding energy was fixed at the theoretical average energy of the polychromatic spectrum. Finally, the X-ray detector response was simplified to be the equal to the energy absorption curve of the CsI scintillator, while the signal conversion from CsI scintillator to the CCD / CMOS sensor was not included.

To further improve the scatter estimation accuracy in practice, the experimentally measured polychromatic X-ray spectrum can be fed into the proposed physics model based scatter estimation. Moreover, a proper material partition could be conducted to enable a theoretically exact calculation of X-ray scattering cross sections for different photon energies and object materials. Notice that material partition is frequently dependent on the reconstructed image voxel values (i.e. CT numbers or attenuation coefficients) [26]. The accuracy of material partition could be severely reduced when there is significant scatter artifact [44]. To bypass this problem, one possible solution is to apply the material partition after the convergence of the proposed iterative scatter correction. In addition, the X-ray detector model could be calibrated to match the specific energy response of a particular imaging system.

Furthermore, the outer region could yield a considerable amount of X-ray scattering signals that eventually reach the X-ray detectors. The corresponding knowledge of the materials and structures (i.e. prior knowledge) may be obtained from the previous planning CT scans of the patients. Since such prior knowledge is not necessarily available before multi-source interior CT scans, it is important to provide a proper estimation of the outer region on the ray paths. We notice that a previously published adaptive water model [41] may be applied to improve the approximation of the outer region in spite of its relatively lower computational efficiency. In addition, the scout views (i.e. global projections of the patients at a few view angles) are frequently acquired to locate or align the interior ROI, and may be combined with the interior CT data to provide a better approximation of the outer region.

The approximation of outer region raises an interesting problem, and we will continue our investigation on this topic in our follow-up studies.

In conclusion, we demonstrated the detrimental impacts of X-ray scattering in a lately proposed multi-source interior CT system architecture, using both Monte Carlo simulation and imaging experiments. The forward scattering and cross scattering from the simultaneously operated multiple imaging chains yielded significant cupping artifact and largely degraded CNR and CT number accuracy in the reconstructed images. The physics model based iterative scatter correction method can greatly suppress the scatter artifact and improve the image quality within a few iterations. The proposed scatter correction method could find use in multi-source interior CT for dynamic CT imaging with high temporal resolution.

References

[1] Z. Sun, G. H. Choo, and K. H. Ng, "Coronary CT angiography: current status and continuing challenges," *The British Journal of Radiology,* vol. 85, pp. 495-510, 2012.

[2] T. G. Flohr, C. N. De Cecco, B. Schmidt, R. Wang, U. J. Schoepf, and F. G. Meinel, "Computed Tomographic Assessment of Coronary Artery Disease: State-of-the-Art Imaging Techniques," *Radiologic Clinics of North America,* vol. 53, pp. 271-285, 3// 2015.

[3] M. Mahesh and D. D. Cody, "Physics of Cardiac Imaging with Multiple-Row Detector CT," *RadioGraphics,* vol. 27, pp. 1495-1509, 2007.

[4] W. A. Kalender, "X-ray computed tomography," *Phys Med Biol,* vol. 51, pp. R29-43, Jul 7 2006.

[5] P. Schardt, J. Deuringer, J. r. Freudenberger, E. Hell, W. Knüpfer, D. Mattern, *et al.*, "New x-ray tube performance in computed tomography by introducing the rotating envelope tube technology," *Medical Physics,* vol. 31, p. 2699, 2004.

[6] T. G. Flohr, C. H. McCollough, H. Bruder, M. Petersilka, K. Gruber, C. Suss, *et al.*, "First performance evaluation of a dual-source CT (DSCT) system," *European Radiology,* vol. 16, pp. 256-268, Feb 2006.
[7] B. Krauss, B. Schmidt, and T. G. Flohr, "Dual source CT," in *Dual energy CT in clinical practice,* ed: Springer, 2011, pp. 11-20.
[8] J. Zhao, Y. Jin, Y. Lu, and G. Wang, "A Filtered Backprojection Algorithm for Triple-Source Helical Cone-Beam CT," *IEEE transactions on medical imaging,* vol. 28, pp. 384-393, 2009.
[9] Y. Lu, J. Zhao, and G. Wang, "Exact image reconstruction with triple-source saddle-curve cone-beam scanning," *Physics in medicine and biology,* vol. 54, pp. 2971-2991, 04/23 2009.
[10] Y. Liu, H. Liu, Y. Wang, and G. Wang, "Half-scan cone-beam CT fluoroscopy with multiple x-ray sources," *Medical physics,* vol. 28, pp. 1466-1471, 2001.
[11] J. Zhao and Y. Xi, "A Reconstruction Method for Circular Interlaced-Source-Detector-Array CT," in *2009 First International Conference on Information Science and Engineering*, 2009, pp. 3575-3578.
[12] G. Wang, H. Yu, and Y. Ye, "A scheme for multisource interior tomography," *Medical Physics,* vol. 36, pp. 3575-3581, 2009.
[13] G. Cao, B. Liu, H. Gong, H. Yu, and G. Wang, "A stationary-sources and rotating-detectors computed tomography architecture for higher temporal resolution and lower radiation dose," *Access, IEEE,* vol. 2, pp. 1263-1271, 2014.
[14] D. Bharkhada, H. Yu, R. Dixon, Y. Wei, J. J. Carr, J. D. Bourland, *et al.*, "Demonstration of Dose and Scatter Reductions for Interior Computed Tomography," *Journal of computer assisted tomography,* vol. 33, p. 967, 2009.
[15] H. Gong, R. Liu, H. Yu, J. Lu, O. Zhou, L. Kan, *et al.*, "Interior tomographic imaging of mouse heart in a carbon nanotube micro-CT," *Journal of X-Ray Science and Technology,* vol. 25, 2016.
[16] G. Wang and H. Y. Yu, "The meaning of interior tomography," *Physics in Medicine and Biology,* vol. 58, pp. R161-R186, Aug 21 2013.
[17] K. J. Engel, C. Herrmann, and G. Zeitler, "X-ray scattering in single- and dual-source CT," *Medical Physics,* vol. 35, pp. 318-332, 2008.
[18] H. Gong, H. Yan, X. Jia, B. Li, G. Wang, and G. Cao, "X-ray scatter correction for multi-source interior computed tomography," *Medical Physics,* vol. 44, pp. 71-83, 2017.
[19] E.-P. Rührnschopf and K. Klingenbeck, "A general framework and review of scatter correction methods in x-ray cone-beam computerized tomography. Part 1: Scatter compensation approaches," *Medical Physics,* vol. 38, pp. 4296-4311, 2011.
[20] E.-P. Rührnschopf and and K. Klingenbeck, "A general framework and review of scatter correction methods in cone beam CT. Part 2: Scatter estimation approaches," *Medical Physics,* vol. 38, pp. 5186-5199, 2011.
[21] R. Ning, X. Tang, and D. Conover, "X-ray scatter correction algorithm for cone beam CT imaging," *Medical Physics,* vol. 31, pp. 1195-1202, 2004.

[22] L. Ren, F.-F. Yin, I. J. Chetty, D. A. Jaffray, and J.-Y. Jin, "Feasibility study of a synchronized-moving-grid (SMOG) system to improve image quality in cone-beam computed tomography (CBCT)," *Medical Physics*, vol. 39, pp. 5099-5110, 2012.
[23] T. Niu and L. Zhu, "Scatter correction for full-fan volumetric CT using a stationary beam blocker in a single full scan," *Medical Physics*, vol. 38, pp. 6027-6038, 2011.
[24] M. Sun and J. M. Star-Lack, "Improved scatter correction using adaptive scatter kernel superposition," *Physics in Medicine and Biology*, vol. 55, p. 6695, 2010.
[25] M. Michael, A. K. Willi, and K. Yiannis, "A fast and pragmatic approach for scatter correction in flat-detector CT using elliptic modeling and iterative optimization," *Physics in Medicine and Biology*, vol. 55, p. 99, 2010.
[26] G. Poludniowski, P. M. Evans, V. N. Hansen, and S. Webb, "An efficient Monte Carlo-based algorithm for scatter correction in keV cone-beam CT," *Physics in Medicine and Biology*, vol. 54, p. 3847, 2009.
[27] K. Yiannis and A. K. Willi, "Intensity distribution and impact of scatter for dual-source CT," *Physics in Medicine and Biology*, vol. 52, p. 6969, 2007.
[28] M. Petersilka, K. Stierstorfer, H. Bruder, and T. Flohr, "Strategies for scatter correction in dual source CT," *Medical Physics*, vol. 37, pp. 5971-5992, 2010.
[29] L. Ren, Y. Chen, Y. Zhang, W. Giles, J. Jin, and F. F. Yin, "Scatter Reduction and Correction for Dual-Source Cone-Beam CT Using Prepatient Grids," *Technol Cancer Res Treat*, May 24 2015.
[30] K. Frutschy, B. Neculaes, L. Inzinna, A. Caiafa, J. Reynolds, Y. Zou, *et al.*, "High power distributed x-ray source," 2010, p. 76221H.
[31] F. Sprenger, X. Calderon, E. Gidcumb, J. Lu, X. Qian, D. Spronk, *et al.*, "Stationary digital breast tomosynthesis with distributed field emission X-ray tube," *Proc SPIE Int Soc Opt Eng*, vol. 7961, Mar 3 2011.
[32] J. Zhang, G. Yang, Y. Z. Lee, S. Chang, J. P. Lu, and O. Zhou, "Multiplexing radiography using a carbon nanotube based x-ray source," *Appl. Phys. Lett.*, vol. 89, p. 064106, 2006.
[33] X. Qian, A. Tucker, E. Gidcumb, J. Shan, G. Yang, X. Calderon-Colon, *et al.*, "High resolution stationary digital breast tomosynthesis using distributed carbon nanotube x-ray source array," *Medical Physics*, vol. 39, pp. 2090-2099, Apr 2012.
[34] X. Jia, H. Yan, L. Cerviño, M. Folkerts, and S. B. Jiang, "A GPU tool for efficient, accurate, and realistic simulation of cone beam CT projections," *Medical physics*, vol. 39, pp. 7368-7378, 2012.
[35] J. H. Hubbell, W. J. Veigele, E. A. Briggs, R. T. Brown, D. T. Cromer, and R. J. Howerton, "Atomic form factors, incoherent scattering functions, and photon scattering cross sections," *Journal of Physical and Chemical Reference Data*, vol. 4, pp. 471-538, 1975.
[36] M. J. Berger, J. Hubbell, S. Seltzer, J. Chang, J. Coursey, R. Sukumar, *et al.*, "XCOM: photon cross sections database," *NIST Standard reference database*, vol. 8, pp. 3587-3597, 1998.

[37] A. Tartari, "Molecular differential cross sections for low angle photon scattering in tissues," *Radiation Physics and Chemistry*, vol. 56, pp. 205-211, 8/1/ 1999.
[38] R. L. Siddon, "Fast calculation of the exact radiological path for a three-dimensional CT array," *Medical Physics*, vol. 12, pp. 252-255, 1985.
[39] U. Schneider, E. Pedroni, and A. Lomax, "The calibration of CT Hounsfield units for radiotherapy treatment planning," *Phys Med Biol*, vol. 41, pp. 111-24, Jan 1996.
[40] Y. Chen, B. Liu, J. M. O'Connor, C. S. Didier, and S. J. Glick, "Characterization of scatter in cone-beam CT breast imaging: Comparison of experimental measurements and Monte Carlo simulation," *Medical Physics*, vol. 36, pp. 857-869, 2009.
[41] M. Bertram, T. Sattel, S. Hohmann, and J. Wiegert, "Monte-Carlo scatter correction for cone-beam computed tomography with limited scan field-of-view," 2008, pp. 69131Y-69131Y-10.
[42] W. Zbijewski and F. J. Beekman, "Efficient Monte Carlo based scatter artifact reduction in cone-beam micro-CT," *IEEE Transactions on Medical Imaging*, vol. 25, pp. 817-827, 2006.
[43] H. Yu and G. Wang, "Compressed sensing based interior tomography," *Physics in medicine and biology*, vol. 54, p. 2791, 2009.
[44] K. Yiannis, R. Thomas, and A. K. Willi, "Combining deterministic and Monte Carlo calculations for fast estimation of scatter intensities in CT," *Physics in Medicine and Biology*, vol. 51, p. 4567, 2006.

Chapter 5 Discussion, conclusion and outlook

5.1 Discussion and Conclusion

The study of chapter 2 was focused on the experimental evaluation of interior CT mode. A CNT field-emission X-ray source was fabricated and then integrated into single imaging chain to form an interior micro-CT platform. A comprehensive study of image quality and radiation dose was then conducted on this imaging platform, using in-house-fabricated phantoms and animal specimen. With a proper reconstruction algorithm, interior micro-CT can provide an image quality comparable to that of the standard global micro-CT. Moreover, interior micro-CT also significantly suppress the radiation exposure. These experimental results could be naturally extended to interior CT mode with clinical imaging geometry. Notice that the in-house-built interior micro-CT scanner could serve the purpose of low-dose and ROI-oriented pre-clinical imaging.

The study of chapter 3 was first focused on the effects of X-ray scattering in multi-source interior CT. The X-ray signals of multi-source interior CT were synthesized in Monte Carlo simulation and imaging experimentation. A comprehensive analysis was then carried out to separately evaluate the effects of X-ray forward scattering and cross scattering, since the X-ray scattering effects was not presented in the previous publications of multi-source interior CT schemes [1, 2]. It was observed that X-ray scattering yielded a significantly detrimental effects on image quality, which is especially true for cross scattering. In this study, no ASG was utilized to suppress X-ray scattering, due to the lack of proper ASG for

physical experiments. Therefore, another Monte Carlo simulation was conducted to estimate the effects of ASG in multi-source interior CT, and the corresponding results are shown in the Appendix. Notice that the previous studies on dual-source CT has reported that the standard hardware-based approaches (i.e. ASG, air gap and collimation) are insufficient for X-ray scatter suppression [3, 4]. To address the X-ray scatter artifact, two dedicated measurement-based scatter correction methods were developed to reduce scatter artifacts: a stationary BSA based method and a pre-programmed STS based method. The stationary BSA based and STS based methods respectively induced minor modification to imaging system configuration and scanning protocols, but both methods could further reduce the radiation dose delivered to the patients.

In the study of chapter 4, a physics model of multi-source interior CT was developed to provide a model-based scatter correction method. The proposed physics model employed the reconstructed CT images and the physical laws to quantify the photon-matter interaction and the resultant X-ray scattering signals. An iterative scatter correction framework was then employed to gradually suppress the scatter artifacts. The region outside the interior FOV was detruncated via an approximation using elliptical water layer. The analytically calculated FSPR and CSPR are comparable to the corresponding references from Monte Carlo simulation and physical experiments. The proposed model-based scatter correction method provided an obvious improvement of image quality, without raising the modifications to system configurations or scanning protocols.

In summary, a comprehensive study has been conducted to separately investigate three critical aspects of a recently proposed conceptual multi-source interior CT scheme [2]: interior CT mode, X-ray scatter effects, and scatter correction approaches. As for interior the benefits of radiation dose reduction has been experimentally validated. The X-ray scattering from the simultaneously operated imaging chains significantly degraded image quality. With the proposed scatter correction methods, the scatter artifact could be largely suppressed and hence maintain an image quality comparable to that of the standard single-source CT.

5.2 Outlook

The potential future research directions are briefly summarized as follows. First, the current technology of CNT X-ray source is still limited by the relatively lower operating voltage and power, which especially hampers the clinical imaging applications. Although the recently developed CNT X-ray source can be operated at a voltage up to 160 kV, the corresponding source power was still much lower than that is required in clinical imaging [5]. Moreover, the spatial density of the CNT field emitters in the source typically determines the angular sampling rate of X-ray projections. Therefore, a future research work could be directed toward the development of CNT X-ray source with more compact configuration and higher operating power. Second, different BSA patterns could be explored for the stationary BSA based scatter correction method. A proper BSA pattern could reserve more primary X-ray signals by reducing the blockage of incident ray paths,

while at the expense of less radiation dose reduction. It would be useful to achieve an optimal trade-off between the blockage and the radiation dose reduction. Third, a future research work could also be focused on improving the approximation accuracy of the outer region, for the proposed model-based scatter correction method. Thus far, there are few publications reporting the methods of recovering the outer region.

References

[1] G. Wang, H. Yu, and Y. Ye, "A scheme for multisource interior tomography," *Medical Physics*, vol. 36, pp. 3575-3581, 2009.

[2] G. Cao, B. Liu, H. Gong, H. Yu, and G. Wang, "A stationary-sources and rotating-detectors computed tomography architecture for higher temporal resolution and lower radiation dose," *Access, IEEE*, vol. 2, pp. 1263-1271, 2014.

[3] K. J. Engel, C. Herrmann, and G. Zeitler, "X-ray scattering in single- and dual-source CT," *Medical Physics*, vol. 35, pp. 318-332, 2008.

[4] K. Yiannis and A. K. Willi, "Intensity distribution and impact of scatter for dual-source CT," *Physics in Medicine and Biology*, vol. 52, p. 6969, 2007.

[5] B. Gonzales, D. Spronk, C. Yuan, A. W. Tucker, M. Beckman, O. Zhou, *et al.*, "Rectangular Fixed-Gantry CT Prototype: Combining CNT X-Ray Sources and Accelerated Compressed Sensing-Based Reconstruction," *Access, IEEE*, vol. 2, pp. 971-981, 2014.